UNIVERSITY OF CALIFORNIA,
IRVINE

Harnessing arginine methyltransferases for targeted protein degradation

DISSERTATION

submitted in partial satisfaction of the requirements
for the degree of

DOCTOR OF PHILOSOPHY

in Biological Sciences

by

Laurence John Seabrook

Dissertation Committee:
Assistant Professor Lauren V. Albrecht, Chair
Professor Aimee L. Edinger
Associate Professor Wenqi Wang
Associate Professor Darci J. Trader
Associate Professor Selma Masri

2026

TABLE OF CONTENTS

LIST OF FIGURES

Page

ACKNOWLEDGMENTS

Firstly, I would like to thank my advisor, Dr. Lauren Albrecht, for guiding me through this research. Having the opportunity to work alongside you throughout this project has forever shaped the way that I think about and perform science. Your attitude inspired me to think bigger, more creatively, and to push against boundaries. Your guidance brought my scientific curiosities to life. Your unconditional support continues to push me forward in the pursuit of my dreams. I could not imagine doing this PhD without you, thank you.

I am incredibly thankful for my committee members, Dr. Aimee Edinger, Dr. Darci Trader, Dr. Selma Masri, and Dr. Wenqi Wang. Being able to share my scientific thought process with you has shaped me into a much more thoughtful scientist and has given me the confidence to move forward in this field. I thank you for dedicating your time towards this research. Your critical insights, advice, and feedback have significantly improved the scope and the rigor of this work.

I would like to thank all of the Albrecht Lab members that helped make this work happen. I am grateful to the collaborators that believed in our lab's wild hypotheses and for letting us into your worlds of science. Thank you to the labs of Dr. Matt Griffin, Dr. Selma Masri, Dr. Brian Paegel, Dr. Dorota Skowronska-Krawczyk, Dr. Darci Trader, Dr. Amit Choudhary, Dr. Stuart Conway. Thank you to the UC Irvine Developmental & Cell Biology Department, the Molecular and Cell Biology Program, the Center for Neurotherapeutics and the UC Center for Drug Discovery. I additionally thank the funding that helped make this work a reality, including the National Cancer Institute at the National Institute of Health (NCI F31CA295037).

The text of the introduction is a reprint of the material as it appears in ChemBiochem. 2025 26(15):e202500345 used with permission from John Wiley & Sons. The co-authors listed in this publication are Laurence J. Seabrook, Catherine R. Livelo & Lauren V. Albrecht. Link to the article: https://doi.org/10.1002/cbic.202500345.

The text of Chapter 1 is a reprint of the material as it appears in Nat Chem Biol. 2024 20:1566–1576, used with permission from Springer Nature. The co-authors listed in this publication are Laurence J. Seabrook, Carolina N. Franco, Cody A. Loy, Jaida Osman, Callie Fredlender, Jan Zimak, Melissa Campos, Steven T. Nguyen, Richard L. Watson, Samantha R. Levine, Marian F. Khalil, Kaelyn Sumigray, Darci J. Trader & Lauren V. Albrecht. Link to the article: https://doi.org/10.1038/s41589-024-01741-y.

The text of Chapter 2 is a reprint of the material as it appears in Chem 2026, 102998, used with permission from Cell Press. The co-authors listed in this publication are Laurence J. Seabrook, Endri Karaj, Shaimaa Sindi, Glen Brodie, Catherine R. Livelo, Melissa Campos, Jack T. Leonard, Fangyuan Gao, Dorota Skowronska-Krawczyk, Matthew E. Griffin, Stuart J. Conway, Amit Choudhary, and Lauren V. Albrecht. Link to the article: https://doi.org/10.1016/j.chempr.2026.102998.

Finally, I would like to thank my partner, my friends, and my family. Thank you to Jack Leonard for your never-ending support and patience, I cannot understate how grateful I am to have done this PhD alongside someone that understands this experience first-hand. You are one of the

brightest scientists that I have ever met, I am incredibly lucky to have you in my corner. To my friends, thank you for making Irvine feel like home and for keeping me grounded throughout this PhD. Thank you to my incredible family for supporting me throughout this long journey, I could not have started, let alone finished, this without you.

VITA

Laurence John Seabrook

2026 Ph.D. Biological Sciences, University of California, Irvine (Irvine, CA)
2024 M.S. Biological Sciences, University of California, Irvine (Irvine, CA)
2020 B.A. Biochemistry, Occidental College (Los Angeles, CA)

FIELD OF STUDY

Cell biology, Chemical biology, Targeted protein degradation, Lysosomes, Methylation, Induced proximity, Degrons, Drug discovery, Assay development

RESEARCH EXPERIENCE

University of California, Irvine – Irvine, CA 2021 – 2026
Graduate Researcher, Advisor: Dr. Lauren V. Albrecht

- Pioneered a small molecule platform to expand the druggable proteome, resulting in 2 first-author publications and patents
- Designed and profiled 60+ small molecule degraders across 20+ disease targets, yielding lead compounds with improved selectivity and potency
- Engineered 10+ stable cell lines and multiplexed reporter assays (HiBiT, HaloTag, CellTiter-Glo) to quantify drug activity in 2D/3D cancer models
- Achieved 5-fold improvement in yield and purity of poorly soluble proteins in *E. coli*, enabling downstream DEL screening and probe development
- Integrated multi-omic approaches to identify and validate novel colorectal cancer drug targets, contributing to 3 co-atuhored manuscripts

Occidental College – Los Angeles, CA 2019 – 2020
Undergraduate Researcher, Advisor: Dr. Michael G. Hill, Dr. Natalie B. Muren

- Engineered a system for renewable and cost-efficient chemical transformations by modulating Cytochrome P450 enzyme activity

Lewis & Clark College – Portland, OR 2017 – 2018
Undergraduate Researcher, Advisor: Dr. Greg J. Hermann

- Characterized the molecular pathways responsible for creating lysosome-related organelles in the developing *C. elegans* intestine

PROFESSIONAL EXPERIENCE

Genentech – South San Francisco, CA 2020 – 2021
Research Technician, Department of Purification Development

- Achieved 20% improvement in yield and purity of antibodies (mAbs, bispecifics) for oncology by FPLC, analytical HPLC, and LC-MS
- Collaborated with cross-functional teams across 3 Stage A mAb purification campaigns, supporting timeline adherence and reproducibility
- Coordinated GMP-compliant sample processing, recording, and analysis with detailed electronic records

PUBLICATIONS

1. Nguyen S, Campos M, Watson R, **Seabrook LJ**, Kim MC, Zuckerman J, Pereira RC, Salusky IB, Catz SD, Albrecht LV. "Lysosome-derived metabolites control lipid dynamics for cellular adaptation in kidney disease." *Nature Cell Biology* 2025, accepted.
2. **Seabrook LJ**, Karaj E, Sindi S, Brodie G, Livelo CR, Franco CF, Campos M, Leonard JT, Gao F, Skowronska-Krawczyk D, Griffin ME, Conway SJ, Choudhary A*, Albrecht LV*. "Exploration of protein degradability enables fully endogenous MrTAC degraders" *Chem* 2026, 102998. (*co-corresponding)
3. Campos M, Nguyen ST, Kong X, Yang Y, Watson RL, Gromova A, Livelo CR, Franco CN, Cabral JE, **Seabrook LJ**, Dai S, Liu Y, Zhou M, Hanse EA, Sumigray K, La Spada AR, Seldin MM, Plikus MV, Nicholas D, McNulty R, Kong M, Yokomori K, Albrecht LV. "PFKM governs metabolic shifts throughout skeletal muscle differentiation." *Nature Metabolism* 2026, 8, 495-505.
4. **Seabrook LJ**, Livelo C, Albrecht LV. "Designing the proteome with chemical tools: Degrons and beyond" *ChemBioChem* 2025, online May 21, 2025.
5. Loy C, Ali E, **Seabrook LJ**, Harris TJ, Kragness K, Albrecht LV, Trader DJ. "ByeTAC: Bypassing an E3 Ligase for Targeted Protein Degradation." *Journal of Medicinal Chemistry* 2025, 68, 9694.
6. **Seabrook LJ** & Albrecht LV. "Targeting proteins to lysosomes with a chemical inducer of arginine methylation." *Nature Chemical Biology* 2024, 20 1564-65.
7. **Seabrook LJ**, Franco CF, Loy CA, Osman J, Fredlender C, Zimak J, Campos M, Nguyen ST, Watson RL, Levine SR, Khalil MF, Sumigray K, Trader DJ, Albrecht LV. "Methylarginine targeting chimeras for lysosomal degradation of intracellular proteins." *Nature Chemical Biology* 2024, 20, 1566-76. Featured on Dec 2024 cover.
8. Franco C, **Seabrook LJ**, Nguyen ST, Yang Y, Campos M, Fan Q, Cichetto AC, Kong M, Christofk HR, Albrecht LV. "Vitamin B6 is governed by the local compartmentalization of metabolic enzymes during growth." *Science Advances* 2023, 9 eadi2232.
9. Franco C, **Seabrook LJ**, Nguyen ST, Leonard JT, Albrecht LV. "Simplifying the B Complex: How Vitamin B6 and B9 Modulate One Carbon Metabolism in Cancer and Beyond." *Metabolites* 2022, 12(10), 961.
10. Brandt J, Voss L, Nicholson K, Rambo F, Thein J, Fairchild L, **Seabrook L**, Lewis D, Guevara-Hernandez L, White ML, Sax L, Eichten V, Harper L, Hermann GJ. "Asymmetric

organelle positioning during epithelial polarization of C. elegans intestinal cells." *Developmental Biology* 2022 481, 75-94.

PATENTS

1. Albrecht LV & **Seabrook LJ**. Induced modification and degradation of endogenous intracellular proteins. Provisional Patent Application Filed July 18, 2025. UC Ref No: 2025-879. NT Ref. No.: UCI 25.19 PROV Application No 63/846,602.
2. **Seabrook LJ** & Albrecht LV. Induced modifications and degradation of intracellular proteins in lysosomes. Provisional Patent Application Filed August 8, 2024. UC Ref No: 2024-9AV-1. NT Ref No UCI 24.12 PROV Application No 63/681,323.

SELECT HONORS AND AWARDS

NCI Ruth L. Kirschstein National Research Service Award (NRSA) (F31) 2025 – 2026
National Institute of Health, F31CA295037
This award supports PhD researchers in scientific health fields in accordance with the mission of the NCI and provided $45,975 of yearly support

Joseph H. Stephens Memorial Prize 2025
University of California, Irvine, School of Biological Sciences
This award recognizes students "displaying excellent in the field of biochemistry and molecular biology" and provided $1,000

Honorable Mention, Graduate Research Fellowship Program (GRFP) 2023
National Research Foundation
This award honors students that "demonstrate the potential to make significant contributions in STEM"

SELECT PRESENTATIONS

1. Keystone Symposium for Proximity-Based Therapeutics. Santa Fe, NM 2025
2. American Society for Cell Biology. San Diego, CA 2024
   Supported by ASCB Travel Grant
3. International Society for Chemical Biology. Toronto, Canada. 2024
   Awarded best Presentation

ABSTRACT OF THE DISSERTATION

Harnessing arginine methyltransferases for targeted protein degradation

by
Laurence Seabrook
Doctor of Philosophy in Biological Sciences
University of California, Irvine, 2026
Assistant Professor Lauren V. Albrecht, Chair

Cellular control over protein stability is essential for homeostasis and adaptation. Proximity underlies the ability of cells to selectively degrade proteins and can be hijacked for therapeutics by targeted protein degradation (TPD). TPD therapeutics eliminate disease-causing proteins by inducing protein proximity with cellular degradation machinery. Since all proteins are eventually broken down, TPD has the potential to eliminate any protein within the proteome. The immense diversity within the human proteome is complemented by many routes and signals for protein degradation. However, most degraders rely on the same pathway for protein clearance, the ubiquitin-proteosome system, which limits the number of proteins we can currently target. Our lab has shown that natively, protein arginine methyltransferase (PRMT) enzymes can mark proteins for lysosomal degradation with a tag named the methylarginine degron. This thesis will discuss a small molecule platform that hijacks methylarginine degrons for TPD. We show that induced proximity with PRMT enzymes can eliminate targets on-command using Methylarginine TArgeting Chimeras (MrTACs). We devised a modular fusion tagging system to recruit PRMTs to protein targets using HaloTag and SNAP-tag fusion proteins. MrTACs could elicit upwards of >95% target degradation in a methylation- and lysosome-dependent manner across native PRMT1 substrates and neo-substrates that are not typically methylated. Unlike the native methylarginine degron, which is only catalyzed by PRMT1, MrTAC degradation could be accomplished by recruiting any PRMT. We leveraged this generalizable activity to develop fully endogenous

MrTACs by repurposing PRMT inhibitors into MrTAC degraders. Group-transfer chemistry enabled us to develop a scalable platform to transform orthosteric inhibitors into silent recruiters that eliminate the PRMT inhibitor upon enzyme binding. Group-transfer MrTACs could eliminate disease-causing proteins and showed an improved anti-cancer activity over existing inhibitors, demonstrating the therapeutic utility of MrTACs. Together, these data demonstrate the value of integrating native biology with TPD towards the goal of improving protein druggability.

INTRODUCTION

Expanding the Druggable Proteome with Targeted Protein Degradation

Targeted Protein Degradation (TPD) is an innovative therapeutic strategy that exploits natural cellular pathways to eliminate proteins on-command (Balch et al., 2008; Li and Crews 2022; Békés et al., 2022). Degraders are small molecule-, antibody-, or aptamer-based drugs that recruit protein substrates to degradation machinery within the cell, which results in clearance of the target. Since most diseases occur at the protein level, TPD has the power to resolve longstanding challenges within therapeutics through the elimination of disease-causing proteins (Hinterndorfer et al., 2025).

Over 85% of human proteins are currently considered undruggable (Schneider et al., 2021; Spradlin et al., 2021). The majority of existing drugs use an occupancy-based mechanism to modulate protein activity, which requires a high level of inhibition to inhibit the entire pool of the target for the remainder of its lifetime. Long-term efficacy therefore requires a high dosage window in order to achieve the desired therapeutic output, which increases the risk of off-target toxicity. Moreover, occupancy-based drugs are restricted to proteins with defined binding pockets that possess a druggable bioactivity such as enzymes and receptors (Schneider et al., 2021). This renders the remainder of the proteome intractable to current therapies, including major disease-causing scaffolding proteins and transcription factors. Degraders, on the other hand, operate by an event-based pharmacology of inducing protein degradation. Degraders can therefore be recycled to facilitate the degradation of many proteins through iterative drug binding and release. Proteins can be recruited to degradation machinery using any target-binding ligand, which differs from traditional drugs that must bind a function-associated pocket. This expands the scope of proteins

that can be targeted towards historically undruggable proteins through ligand binding to shallow pockets and grooves on protein surfaces. Given that all proteins are subject to degradation and possess diverse surfaces for ligand binding, TPD has the potential to expand druggability towards the entire human proteome. With over 52 degraders in clinical trials and the first anticipated approval in 2027, TPD has the potential to resolve longstanding gaps in therapeutics (Chirnomas et al., 2023).

The leading degrader class is PROteolysis TArgeting Chimera (PROTAC), which facilitates protein degradation via the ubiquitin-proteastome system (Békés et al., 2022). PROTACs are heterobifunctional molecules composed of a target-binding ligand and an E3-binding ligand, joined by a chemical linker (Figure 0.1). PROTACs recruit protein targets to E3 ubiquitin ligases, which act as scaffolds for K48-linked ubiquitination of the target by E2 ligases. Proximity-induced ubiquitination then signals the protein for degradation by the 26S proteasome. The heterobifunctional design of PROTACs is highly modular, which allows scalable recruitment of different target-E3 pairs based on ligand selection.

Gaps in Proteome Coverage with Current Degrader Modalities

Early success within the TPD field has inspired a boom in degrader discovery with the development of over 3,270 published PROTAC molecules (Weng et al 2023). Despite the promise of degraders to expand protein druggability, an incredibly small fraction of the proteome has yet to be targeted. As of 2025, only 95 proteins have been successfully targeted by degraders, which represents <0.5% of the human proteome.

The success of PROTAC degradation is predominantly determined by the ability to form an optimally oriented ternary complex that results in productive ubiquitination of the target protein. Extensive mechanistic research has highlighted that PROTAC degradation can be impeded by improper ternary complex formation, substrate orientation, and an inability of the proteasome to clear ubiquitinated proteins. Although linkers can typically be optimized to generate productive ternary complexes, Martin et al. found that PROTACs can fail to form ternary complexes if the target-binding ligand resides too deep within the protein, which blocks protein-protein interaction even when using very long linkers (Martin et al., 2024). Shallow pockets are therefore more likely to generate stable E3-substrate complexes that result in target ubiquitination. However, the formation of a ternary complex formation does not guarantee effective ubiquitination. Structural modeling by Crowe et al. used revealed that successful ubiquitination requires highly specific orientation of the substrate in order for the E2 ubiquitin ligase to facilitate lysine ubiquitination (Crowe et al., 2024). Predictive modeling and molecular docking have become crucial in degrader design to promote efficient ternary complex formation. A number of studies have shown that in the final step of the PROTAC pathway, properly ubiquitinated substrates are not always recognized for degradation by the proteasome. Fischer and colleagues combined global proteomic profiling with ubiquitin-enrichment proteomics to find that in response to PROTAC treatment, certain proteins can be readily degraded but others are often stunted at the step of ubiquitination and fail to degrade (Huang et al., 2024). Variability was observed even within the same protein family, highlighting the complex variables that shape the PROTAC mechanism. As such, there has been a recent emphasis in the TPD field to screen degraders on the basis of target degradation instead of binding-based or ubiquitination-based assays. Although PROTACs can drive powerful

effects on protein and cell biology, their multi-step mechanism creates potential pitfalls in studying new targets.

In both native and chemically-induced settings, certain proteins are more readily degradable than others due to differences in structure, localization, interactions, and more. The relationship between TPD success and innate protein degradability was first studied by Fischer and colleagues, who used unbiased chemoproteomics to identify proteins that are highly degradable by PROTAC. Xiong et al. identified differences in degradability within the histone deacetylase (HDAC) family by testing HDAC degradation across a library of PROTACs bearing pan-HDAC inhibitors that would simultaneously bind all 11 HDACs (Xiong et al., 2021). To account for variability in ligand affinity for one HDAC over the other, researchers constructed a 48-member PROTAC library consisting of 4 different HDAC ligands, 11 linker types, and 4 different E3 ligases. Although all HDACs are degraded by the ubiquitin-proteasome system, they discovered that HDAC6 was very readily degradable, whereas HDAC9 could rarely be degraded. A similar trend was observed in studying degradability of cyclin dependent kinases (CDKs) (Donovan et al., 2020; Huang et al., 2024). Several CDKs (CDK2, 5, 7, 9, 12, and 16) could be readily degraded by pan-kinase PROTACs, but CDK10 resisted degradation despite being successfully ubiquitinated. These reports highlight that intrinsic differences in protein behavior can affect each step of the PROTAC mechanism and highlights the importance of target selection for degrader studies. Machine learning strategies and predictive modeling can be used to predict protein compatibility with PROTAC approaches based on features like disorder, size, turnover, and localization (Donovan et al., 2020, Zhang et al., 2022). Schneider et al. applied such tools to predict that over 1,336 proteins

can be readily degradable by PROTACs (approximately 7.5% of the proteome), which provides a streamlined strategy to nominate and eliminate pathogenic protein targets (Schnieder et al., 2021).

Despite advances in PROTAC modeling and prediction, the vast majority (>90%) of the human proteome is considered a challenging target for PROTAC development. In recognition of this gap, many groups have devised novel approaches to target proteins for degradation beyond the classic PROTAC mechanism. For example, upstream steps of E3-substrate interfacing and ubiquitination can be bypassed using degraders that recruit targets to E2 ubiquitin ligases or even to the proteasome itself (Forte et al., 2023, Loy et al., 2025). This allows for streamlined degrader design by minimizing several of the confounding variables in the PROTAC mechanism, including the requirement for multi-protein assemblies involving the ubiquitin cascade. However, these modalities have largely focused on degrading previously established targets in proof-of-concept studies and it remains unclear whether they can eliminate un-PROTACtable proteins.

Identifying the full repertoire of cellular machinery that is available for exploitation by TPD is a major unmet need within degrader research. More than 90% of published degraders rely on the same two E3 ligases to coordinate TPD: cereblon (CRBN) and Hippel-Lindau tumor-suppressor (VHL). Several research groups have sought to identify other tractable E3 ligases, including cellular IAP1 (cIAP1), mouse double minute 2 (MDM2), Kelch-like ECH-associated protein-1 (KEAP1), and DDB1-cullin 4-associated factor (DCAF) (Han and Sun 2023). Chemogenetic screening has uncovered the many other proteins capable of being used as effectors of TPD,

including and beyond E3 ligases (Poirson et al., 2024, Serebrenik et al., 2024). This revealed that many proteins can be used for TPD, including chaperone machinery, autophagy-related proteins, and other proteins responsible for maintaining proteostatic quality control. Whether these novel effectors and alternative routes for degradation can be used to eliminate PROTAC-resistant proteins has yet to be determined but provides an exciting opportunity to resolve gaps in degrader coverage.

Targeted Protein Degradation via Lysosomes

With only two primary sites of degradation within the cell, the proteasome and the lysosome, there is a great interest in understanding how cells selectively mark proteins for degradation. Lysosomes degrade a different suite of proteins to the proteasome, including extracellular- and membrane-bound proteins, complex biomacromolecules, aggregates, and organelles (Klionsky et al., 2021). As such, lysosome-targeting degraders have the power to expand substrate coverage by TPD beyond the scope of current PROTAC technologies.

Lysosomal TPD has been readily accomplished for extracellular targets by hijacking cell-surface receptors for target endocytosis (Banik et al., 2020). In contrast, the ability to hijack lysosomes for intracellular TPD has lagged behind proteasomal degraders. Mapping the cellular cues for lysosomal degradation has identified several novel opportunities for intracellular TPD through pathways that act orthogonally to the ubiquitin-proteasome system.

There are three intracellular pathways for intracellular lysosomal degradation: macroautophagy, microautophagy and chaperone-mediated autophagy (Zhou et al., 2025). In macroautophagy,

cytoplasmic cargo is encapsulated by budding autophagosomes that eventually close and fuse with lysosomes, where substrates are then degraded. While macroautophagy has been historically associated with non-selective protein clearance during starvation, macroautophagy can clear proteins selectively through receptor-mediated interactions. The autophagosome membrane is decorated with receptors and adaptor proteins that bind cargo directly, which includes hallmark proteins LC3, p62, and OPTN (Zhou et al., 2025). Early attempts to hijack macroautophagy for TPD showed that autophagosome receptors can be used as docking sites to tether target proteins for macroautophagy through LC3 or p62 recruiters. For example, Autophagosome Tethering Chimeras (ATTECs) recruited targets to LC3B and could be used to degrade aggregates and organelles, including the neurodegeneration-linked mutant form of Huntingtin (Figure 0.2) (Li et al., 2019, Schwalm et al., 2024). Interestingly, the basal activity of macroautophagy was able to support this degradation in the absence of starvation in both cell-based and in vivo models. Ji et al. devised p62-recruiting Autophagosome Targeting Chimeras (AUTOTACs) that simultaneously recruit protein targets and stimulate autophagosome formation through ligand-induced p62 oligomerization, which was thought to improve degrader efficacy (Ji et al., 2022). These degraders have expanded the coverage of degraders to eliminate challenging targets that PROTACs cannot degrade, including aggregates, organelles and protein complexes. Furthermore, lysosomal degraders could provide an opportunity for TPD in cancers with hyperactive lysosomal activity, where lysosomal activity dominates over proteasomal activity.

Chaperone-mediated autophagy (CMA) mediates protein clearance in response to signaling cues and is strongly activated by starvation (Dice 1990). Proteins are marked for CMA based on an encoded pentapeptide consensus motif, KFERQ (Lys-Phe-Glu-Arg-Gln), which is recognized by

Hsc70 chaperones that deliver protein cargo to the lysosomal surface. Hsc70 interactions with the lysosomal associated membrane protein 2A (LAMP2A) enables protein unfolding by co-chaperones. LAMP2A multimerization enables translocation of the unfolded protein into the lysosomal lumen for degradation. Biochemical analyses demonstrated that CMA clearance can extend beyond the canonical KFERQ sequence to clear proteins that bear KFERQ-like sequences. The KFERQ recognition motif is flexible and can be mimicked by post-translational modifications such as lysine acetylation to mimic the terminal glutamine (Lv et al., 2011). Although a large fraction of the proteome possesses CMA motifs, different CMA cues (starvation, oxidative stress, hormone signaling) often result in different proteins being targeted by CMA. Mapping proteomic changes in response to CMA activation is further complicated by cross-talk with other proteolysis pathways, where CMA can degrade proteolysis machinery like the macroautophagy initiator protein Atg5 (Zhao et al., 2025). The connection between cellular dynamics and the substrates that are selected for CMA degradation remain poorly understood, but may be explained through differences in protein modifications, localization, and interactions.

Proteins can be targeted for CMA by genetically encoding the canonical KFERQ motif into their sequence, but a small molecule approach capable of degrading endogenous proteins by CMA has yet to be established (Fan et al., 2014). Given that CMA is largely coordinated by chaperones that facilitate a number of different cellular processes, successful TPD by CMA will likely occur by hijacking the downstream steps of CMA through LAMP2A recruiters. Whether CMA-based degraders will still require protein unfolding for lysosomal uptake will likely determine the scope of CMA-based degraders to degrade proteins beyond classic PROTAC targets.

Microautophagy facilitates protein clearance through protein docking at the surface of the lysosome or late endosome (Wang et al., 2023). Microautophagy uses the same protein machinery that is responsible for maintaining homeostasis of the lysosome itself to facilitate the import of proteases and the turnover of lysosomal membrane proteins (Li et al., 2019). In selective microautophagy, protein substrates are docked at the lysosome surface by chaperones and scaffolding proteins. Proteins are then transported into the lysosomal lumen by Endosomal Sorting Complexes Responsible for Transport (ESCRT) machinery, which facilitate membrane invagination to create multivesicular bodies that are subsequently digested in the lysosomal lumen alongside the protein cargo. Much like CMA, microautophagy has high levels of cross-talk with other degradation pathways and can scavenge non-canonical substrates in response to environmental cues. For example, the removal of damaged proteasomes is usually coordinated by macroautophagy but shifts towards microautophagy during glucose depletion (Li et al., 2019). The precise mechanism behind this shift is incompletely understood.

Given that microautophagy is capable of clearing large protein complexes like the proteasome and even organelles, microautophagy provides a potential avenue to expand the substrate scope of TPD. Nalawansha et al. developed a microautophagy tethering platform (lysosomal membrane targeting chimera, LYMTAC) that mirrors the AUTOTAC/ATTEC tethers for macroautophagy (Nalawansha et al., 2025). LYMTACs recruit protein targets to short-lived proteins that are embedded within the lysosomal surface. Induced proximity results in the passive turnover of the target protein alongside the short-lived protein, which is cleared through microautophagy. Protein recruitment to multiple short-lived membrane proteins, including RNF152 and LAPTM4a, resulted in degradation of several major disease targets, including KRAS. However, authors relied

on fusion tag approaches to recruit proteins to these lysosomal proteins since neither RNF152 nor LAPTM4a possess defined ligands for recruitment. Whether LYMTACs can degrade multisubunit protein complexes, organelles or aggregates has yet to be tested.

Overall, lysosomal degraders currently operate through a similar mechanism of recruiting protein targets to lysosomal machinery that facilitates passive protein uptake by the lysosome. This follows suit of classical inhibitors and uses an occupancy-based mechanism where the substrate and effector must be engaged for the entire lifetime of the substrate to ensure its degradation. PROTAC technologies benefit from event-based pharmacology, where ubiquitinated proteins can still be sent for degradation even after the substrate dissociates from the E3-PROTAC complex. Identification of a protein modification for the lysosome could significantly improve lysosomal degrader technology and improve the substrate targeting capabilities of TPD.

Natural Protein Degradation via the Methylarginine Degron

A major knowledge gap in the field of protein degradation is understanding how lysosomes coordinate selective protein degradation. While proteasomal degradation can be encoded by K48-linked ubiquitination, a consensus signal for the lysosome has not been clearly established. K63-linked ubiquitination sometimes signals for degradation via macroautophagy, but this is predominantly activated during starvation and stress (Zhang et al., 2018). Understanding the cellular signals that encode lysosomal degradation in steady-state cells could resolve major gaps in degrader capabilities.

Recent work found that cells can mark intracellular proteins for lysosomal degradation with a modification referred to as the methylarginine degron (Figure 0.3). Originally identified in the early stages of canonical Wnt3a signaling, a surge of global arginine methylation marks hundreds of cytosolic targets to be degraded in lysosomes via microautophagy (Albrecht et al., 2018). Our lab recently identified and characterized one of the substrates regulated by methylarginine degrons. We found that this degradation pathway regulates the levels of pyridoxal kinase (PDXK), which is the sole enzyme responsible for metabolizing dietary vitamin B6 into its active form (Franco et al., 2023). In response to Wnt stimulation, protein arginine methyltransferase 1 (PRMT1) methylates a single arginine residue on PDXK (R292), which is both necessary and sufficient for its lysosomal degradation. PDXK loss reshaped the metabolic landscape of Wnt-active cells with a decreased flux of inactive Vitamin B6 into its active form. Alongside other methylarginine degron substrates, PDXK is degraded in lysosomes via endosomal sorting complexes required for transport (ESCRT)-mediated microautophagy, which acts orthogonal to macroautophagy (Wang et al., 2023). Modulating PDXK degradation could suppress the growth of high-Wnt cancer cell models that rely on hyperactive Wnt signaling and PDXK degradation to facilitate uncontrolled growth. Although methylarginine degrons were activated by Wnt signaling, PRMT1 activity also regulated PDXK turnover under steady-state conditions. Whether this novel protein modification can be exploited chemically for TPD has yet to be examined. A complete understanding of the fundamental biology of arginine methylation will be essential to fully understand the scope, function, and clinical relevance of methylarginine degrons.

Regulation of Arginine Methylation

Arginine methylation is a widespread protein modification that marks over 25% of the human proteome (Maron et al., 2021). Methylation is catalyzed by protein arginine methyltransferases (PRMTs) which are structurally defined by the presence of an N-terminal Rossman Fold and β-Barrel that interface to form the methyltransferase active site (Schapira and Ferreira de Freitas 2014, Boriack-Sjodin and Swinger 2015). PRMTs possess N-terminal dimerization arms that enable head-to-tail interactions and have been reported to form higher order multimers and filaments that promote processive methylation (Lim et al., 2005, Dang et al., 2024). PRMTs are divided into three classes depending on the type of arginine methylation they catalyze: asymmetric dimethylation (Type I PRMTs), symmetric dimethylation (Type II PRMTs), or monomethylation (Type III PRMTs). Most PRMTs exist in the cytoplasm and nucleus with only PRMT3 (cytoplasmic) and PRMT6 (nuclear) showing subcellular-specific expression, although PRMTs can mislocalize in certain diseases (Hwang et al., 2021, Chan et al., 2018). PRMT8 is the only tissue-specific PRMT and is exclusively expressed in cortical neurons. Dysregulation of PRMT expression is strongly linked with the progression of many cancers through methylation-dependent reprogramming of cancer cell cycling, metabolism, migration, metastasis, and tumor suppressor silencing. Structurally, methylation creates steric bulk and blocks hydrogen bonding of the guanidinium nitrogen, which can reshape protein interactions with other proteins, RNA and DNA. The small size and lack of charge of this protein modification makes it challenging to study arginine methylation. As such, only a small fraction of the human methylome has been functionally characterized with a predominant focus on the effects of histone methylation in gene regulation.

Unbiased proteomic analyses have sought to map the human methylome using antibody-based approaches to isolate and identify methylated proteins. Over 5,386 arginine methylation events have been identified over 5,255 unique proteins (Maron et al., 2021). However, unbiased substrate mapping requires isolation of methylarginine-modified proteins using antibodies that enrich for canonical methylation motifs (glycine/arginine-rich, e.g. RGRG, RGGRGG) and likely underestimates the number of methylated proteins. Quantifying methylarginine abundance relative to global amino acid prevalence provides an alternative lens to estimate methylation prevalence, which revealed that approximately 7% of cellular arginine is methylated (Larsen et al., 2016). This rivals other protein modifications such as serine phosphorylation (9% of serine), lysine ubiquitination (7%) and threonine phosphorylation (3%). Interestingly, arginine methylation often crosstalks with other modifications and shows positive enrichment with serine phosphorylation events, which may indicate a priming event where one modification promotes the deposition of a nearby modification. Inversely, arginine methylation negatively correlates with lysine ubiquitination and may serve as a competition-based mechanism to control protein processing by the proteasome.

Several protein families recognize and bind methylarginine proteins to coordinate downstream effects with Tudor domain-containing proteins acting as the primary reader of methylarginine modifications. Tudor domains contain aromatic cages that enable binding to methylated amino acids (arginine or lysine) via cation-π stacking and are found in over 42 human proteins (Uguen et al., 2024; Wang and Bedford 2023). Differences in the size and composition of the aromatic cage allows tudor domains to bind with different selectivity profiles against the six types of arginine and lysine methylation: monomethylarginine, asymmetric dimethylarginine, symmetric

dimethylarginine, monomethyllysine, dimethyllysine, or trimethyllysine. Many downstream effects have been reported depending on the substrate being modified, the type of modification, and the reader protein. In fact, different types of methylation can result in opposite phenotypes despite seemingly small differences in the methyl structure. For instance, asymmetric dimethylation of MYC by PRMT1 causes protein degradation whereas symmetric dimethylation of MYC by PRMT5 stabilizes protein levels through undefined mechanisms (Favia et al., 2019). The diverse downstream consequences of methylarginine modifications challenge our understanding of how this modification regulates cell function. This is further complicated by the ability of PRMTs to perform substrate scavenging, where knockdown of one PRMT often results in an upregulation of other PRMT activities on the same set of substrates. However, the requirement of PRMT1 for cell and organism viability suggests that PRMT1 methylates a specific profile of substrates that other PRMTs cannot compensate for. Discrepancies in substrate scavenging between PRMTs have yet to be comprehensively studied.

Relative to the dynamic addition and removal of other protein modifications, methylarginine modifications are thought to be very stable modifications that are retained on the substrate for its lifetime. There have been a select set of instances of methylarginine removal by three mechanisms: removal of the methyl group, conversion to citrulline, and cleavage of the methylarginine-containing peptide (Wang and Bedford 2023). Jumonji domain containing protein 6 (JMJD6) is a putative arginine demethylase and its downregulation leads to an increase in cellular monomethylarginine, symmetric dimethylarginine and asymmetric dimethylarginine (Chang et al., 2007). However, reports of its demethylase activity are largely restricted to in vitro studies, which show that dimethylarginine-modified proteins can be reverted to an unmethylated state via a

monomethyl intermediate. Whether demethylation by JMJD6 is important for regulating methylarginine biology remains largely unstudied in an in vivo, biologically relevant setting. The protein arginine deiminase (PAD) family of enzymes is known to convert unmodified arginine to citrulline. Wang et al. discovered that PAD4 is also able to act on monomethylarginine residues to similarly yield citrulline in a process referred to as demethylimination (Wang et al., 2004). Finally, methylarginines can act as a cleavage signal for the modified protein to be digested by Jumonji domain containing proteins 5 and 7 (JMJD5 and JMJD7), which possess aminopeptidase activities. JMJD5 and JMJD7 bind methylarginine-modified histones and cleave the methylarginine site (Liu et al., 2017). Interestingly, cleavage often results in complete digestion of the remaining protein but it is unclear whether this activity is performed by JMJD5 and JMJD7 or by other proteases. It is possible that methylarginine cleavage acts as a more general signal for regulating protein turnover in the cell. By interaction mapping, JMJD5 and JMJD7 bind non-histone proteins but their proteolytic activity has only been studied in the context of chromatin remodeling (Bedford and Wang 2023). Given that JMJD5 and JMJD7 are often dysregulated in cancers, understanding these mechanisms of proteostatic maintenance could offer a potential window to better understand cancer cell biology.

Chemical Control of Arginine Methylation

As master regulators of cell activity, PRMTs provide a promising avenue to treat cancer, respiratory disease, inflammation, cardiovascular disease and more (Hwang et al., 2021, Hu et al., 2015). Chemical control over PRMT activity has only recently gained attention with the first pan-PRMT inhibitor discovered in 2015 (Hu et al., 2015). Hu et al. discovered that the small molecule AMI-1 inhibits all nine human PRMTs by occupying the peptide binding grooves. Early efforts

using AMI-1 showed that inhibiting PRMT activity can suppress in vitro and in vivo models of cancer progression, which has since inspired the development of PRMT inhibitors with improved selectivity profiles. High homology between PRMT active sites is often a challenge for inhibitor development but can be overcome using structure-oriented and counter-screening approaches (Boriack-Sjodin and Swinger 2025) (Figure 0.4A). Significant efforts in PRMT ligand discovery have generated orthosteric and allosteric inhibitors for PRMT3 (SGC707), PRMT4 (TP-064, EZM2302), PRMT5 (GSK3326595, JNJ-64619178, LLY-283), PRMT6 (SGC6870, EPZ020411, MS117), and PRMT7 (SGC8158) (Hwang et al., 2021). Selective ligands have yet to be identified for PRMT1, PRMT2, PRMT8, and PRMT9.

Although many cancers rely on PRMT1 overexpression, selective inhibition of PRMT1 remains elusive due to its structural similarity to other PRMTs. Since PRMT1 is the most active PRMT and is responsible for catalyzing >80% of cellular arginine methylation, inhibitors that target the Type I PRMT family (MS023 and GSK3368715) are often used as a proxy for PRMT1 inhibition. While this has proven effective for studying PRMT1 activity through in vitro and in vivo studies, clinical translation of Type I PRMT inhibitors has been limited by off-target effects. A clinical trial testing GSK3368715 for the treatment of various solid tumors was terminated early due to unpredictable success in tumor regression and several off-target effects in peripheral blood (El-Khoueiry et al., 2023). In contrast, several highly specific inhibitors against PRMT5, which is also upregulated in cancer, have shown success in clinical testing with superior safety profiles (Lee et al., 2015). Continued development of PRMT1 inhibitors with improved selectivity may resolve gaps in our ability to target this enzyme clinically.

In pursuit of alternative strategies to reduce PRMT activity, several PRMT inhibitors have been recently transformed into PROTACs aiming to degrade PRMT1, PRMT3, PRMT4, and PRMT5. PROTACs derivatized with the PRMT5 ligand GSK3326595 were capable of degrading PRMT5 to high levels using CRBN or VHL with specificity over other PRMTs (Guo et al., 2024, and Ju et al., 2025). However, it has yet to be demonstrated whether PRMT5-targeting PROTACs show superior potency or efficacy over existing PRMT5 inhibitors. PRMT4- and PRMT3-targeting PROTACs, however, have shown significant improvements over traditional inhibitors in models of multiple myeloma and acute leukemia, respectively (Shen et al., 2020, Guo et al., 2024, and Ju et al., 2025; Zou et al., 2024).

While PRMT3-, PRMT4-, and PRMT5-targeting PROTACs have been able to induce high levels of target degradation, the targeted degradation of PRMT1 has remained challenging. Using the Type I PRMT inhibitor, GSK3368715, Martin et al. developed CRBN- and VHL-recruiting PROTACs to target PRMT1 but were unable to detect degradation (Martin et al., 2024). Unsuccessful degradation was hypothesized to be a result of poor ternary complex formation since the site of GSK3368715-PRMT1 interaction lies deep in the base of the PRMT1 active site (Figure 0.4B). Since GSK3368715 binds all Type I PRMTs, it would also be worth evaluating whether other PRMTs, including PRMT2, 3, 4, 8, were degraded by GSK3368715-recruiting PROTACs. Discovery of other ligandable sites outside of the substrate binding pocket may greatly enhance our ability to control the activity of the highly active, disease-linked PRMT1 enzyme.

Although ternary complex formation was not directly studied, the ability of PRMT1 to form higher order tetramers, octamers and even 10-mer filaments may further reduce the ability of CRBN and

VHL-recruiting PROTACs to eliminate PRMT1 (Deng et al., 2024). However, other PRMTs, including PRMT4 and PRMT5, also form multimeric structures like PRMT1 and could be successfully degraded by PROTAC. TRIM21 is an E3 ligase that was recently hijacked by PROTACs for the targeted degradation of multimeric protein complexes due to its ability to multimerize and ubiquitinate large protein complexes simultaneously (Lu et al., 2024). It is possible that TRIM21-based PROTACs may improve our ability to degrade PRMTs on command. Mapping the multimeric states of PRMTs within cells remains largely undetermined and may streamline the development of PRMT-targeting PROTACs.

Many PRMTs possess structurally distinct allosteric pockets, which have been exploited for the discovery of allosteric ligands for PRMT3, PRMT5, and PRMT6 (Shen et al., 2021). Structural modeling has revealed several unexplored pockets within PRMTs, including PRMT1, that may be exploitable for future PRMT ligand development (Schapira and Ferreira de Freitas 2014). While assays have been developed to screen for activators of PRMT activity, only inhibitors have been discovered thus far (Prabhu et al., 2017). Chemical modulation is thereby limited to suppression of PRMT activity, which may not be favorable for all diseases. Moreover, existing PRMT inhibitors are unable to control specific PRMT-substrate interactions and instead affect the overall activity of the enzyme. Chemical probes capable of modulating PRMT activity with specificity towards a specific substrate could resolve a major gap in our ability to study and perturb arginine methylation.

Harnessing the Methylarginine Degron for Targeted Protein Degradation

Lysosomal degraders are currently limited by the lack of a lysosome-targeting protein modification that is akin to ubiquitin for the proteasome. The discovery of the methylarginine degron offers a profound opportunity to resolve gaps in TPD by using induced protein methylation to degrade proteins in lysosomes. Harnessing methylarginine degrons for TPD could resolve major gaps in protein degradability, but no tool has been developed to selectively induce methylation. In this work, I demonstrate that small molecule recruitment of PRMTs can be used for proximity-induced methylation with a platform named methylarginine targeting chimeras (MrTACs). I show that MrTACs can be applied to tag disease-causing proteins with methylarginine degrons, thereby resolving major gaps in druggability and the TPD field.

We first develop a chemogenetic tagging platform to demonstrate that MrTAC recruitment of PRMT1 to protein targets is sufficient for targeted protein degradation through microautophagy. We find that MrTACs can degrade both native PRMT1 substrates and neo-substrates that are not typically methylated. Screening a panel of diverse substrates shows that MrTAC can degrade a wide range of proteins and is especially capable of eliminating disordered, long-lived proteins with high arginine content. Although PRMT1 is the only PRMT implicated in native methylarginine degron regulation, we find that MrTAC degradation can be achieved using methyltransferases across all three of the PRMT classes.

The generality of PRMTs for MrTAC degradation enabled us to repurpose a series of PRMT inhibitors to develop fully endogenous MrTACs. We find that some PRMT inhibitors can be used for MrTACs in a catch-and-release mechanism, where MrTAC recruits the PRMT to the substrate and subsequently releases the PRMT for induced methylation of the target. However, not all

PRMT inhibitors resulted in successful MrTAC degradation due to inhibition of the PRMT in the final ternary complex. We demonstrate that group-transfer chemistry can provide a scalable alternative to convert PRMT inhibitors into silent recruiters by inhibitor-directed addition-elimination that eliminates the PRMT inhibitor following covalent labeling. Endogenous MrTACs show highly potent and selective degradation of pathogenic proteins, which suppressed cancer proliferation. We present the first non-inhibitory tool to study PRMT activity, which we applied for TPD through methylarginine degron addition. Moreover, MrTAC modulates PRMT-substrate interactions with high selectivity, which provides an advance over existing methyltransferase probes that globally modulate PRMT activity. Overall, we provide a generalizable strategy to study, induce, and assess the effects of arginine methylation in cells. This resolves major gaps across the fields of proteostasis, chemically-induced proximity, and targeted protein degradation.

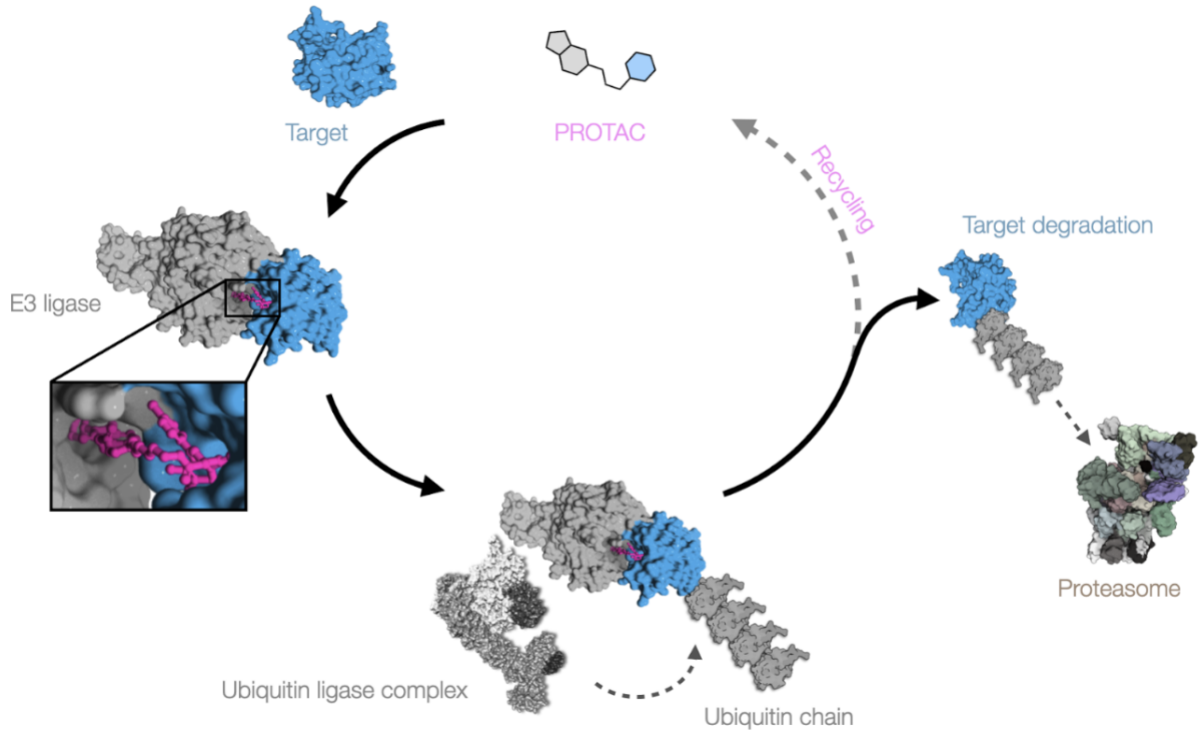

Figure 0.1 Targeted protein degradation by PROTACs

Proximity- induced ubiquitination using deposited crystal structures: BRD4 BD1 (blue) in complex with the E3 ligase CRBN (gray) and dBET6 PROTAC (pink) (PDB 6BOY), ubiquitin ligase complex (PDB 2HYE), ubiquitin chain (1UBQ).

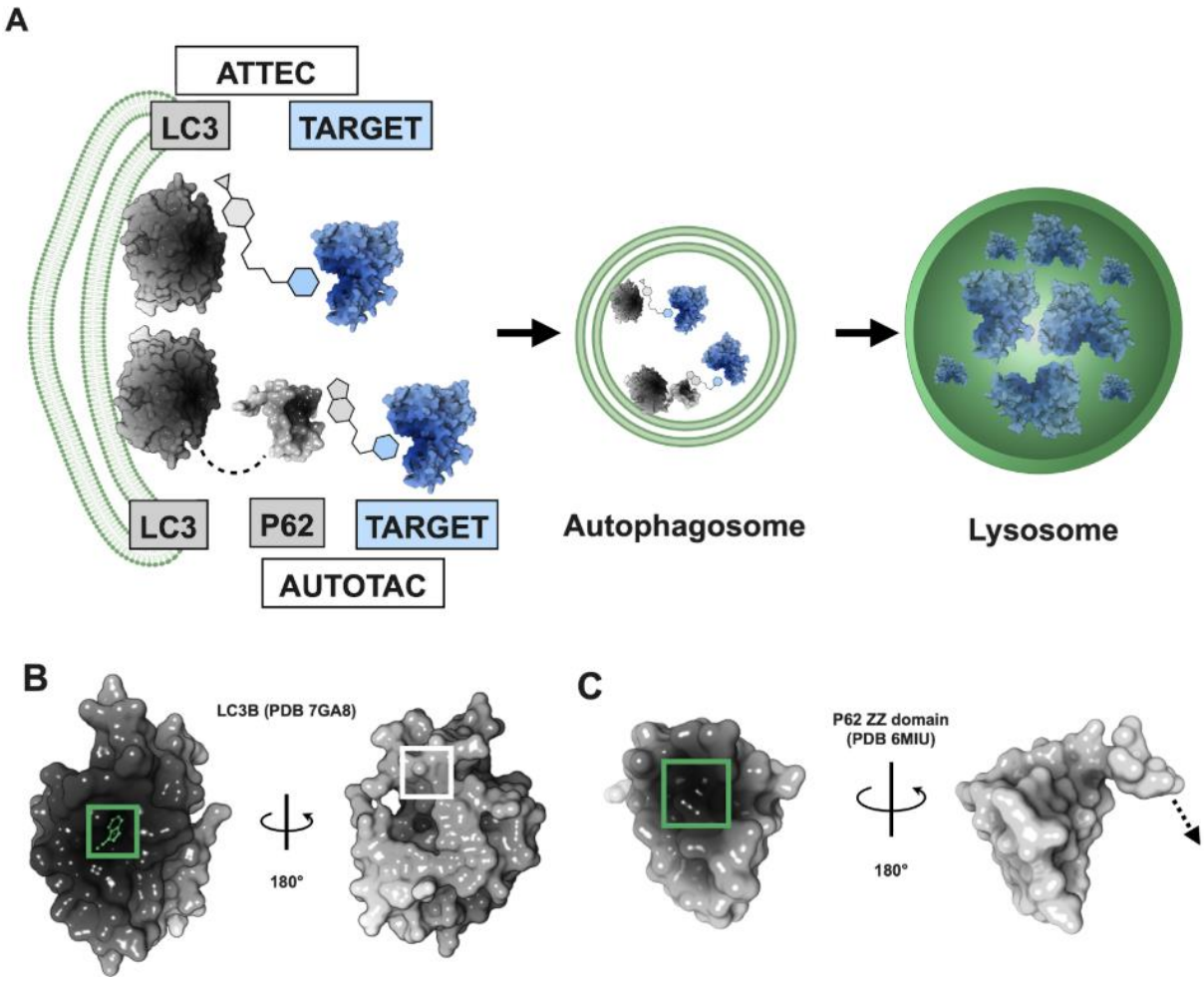

Figure 0.2 Binding modes of lysosomal degraders

(A) Model depicting ATTEC and AUTOTAC recruitment of a target protein (blue, PDB 1I09) to budding autophagosomes before enclosure and fusion with lysosomes. **(B)** Structure of the ligandable LC3B binding pocket for ATTEC recruitment (PDB 7GA8). Green square shows one available ligand binding site, white square shows the autophagosome tethering site. **(C)** Structure of the P62 ZZ domain for AUTOTAC recruitment (PDB 6MIU), green square shows the ligand binding site, arrow points towards the C-terminal domains.

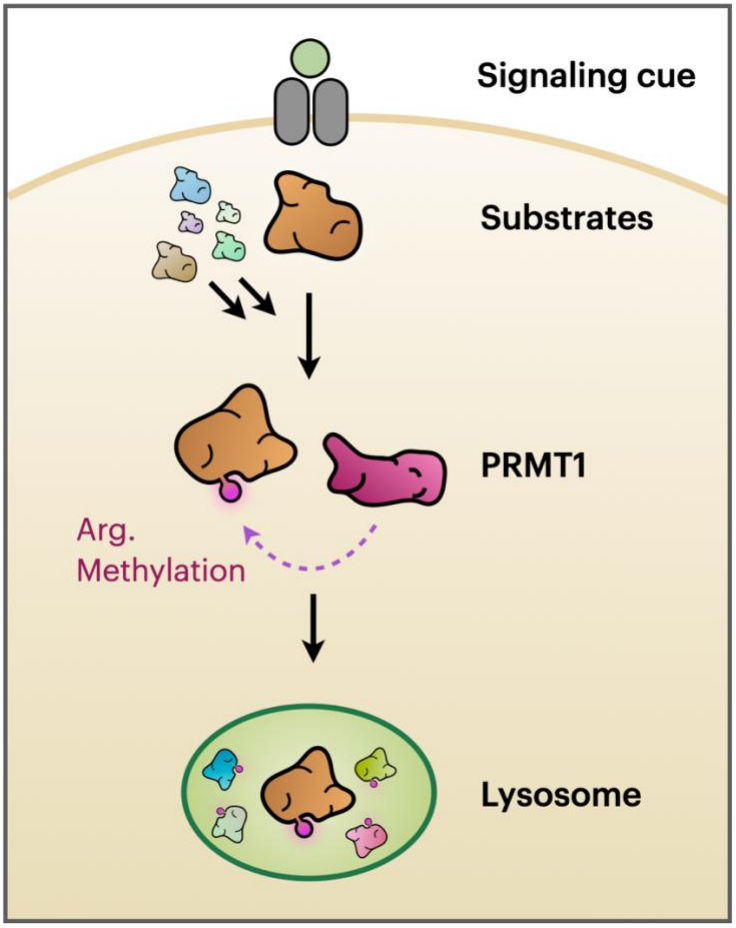

Figure 0.3 Native protein clearance by methylarginine degrons.

Model of protein clearance by methylarginine degrons, facilitated by protein arginine methyltransferase 1 (PRMT1).

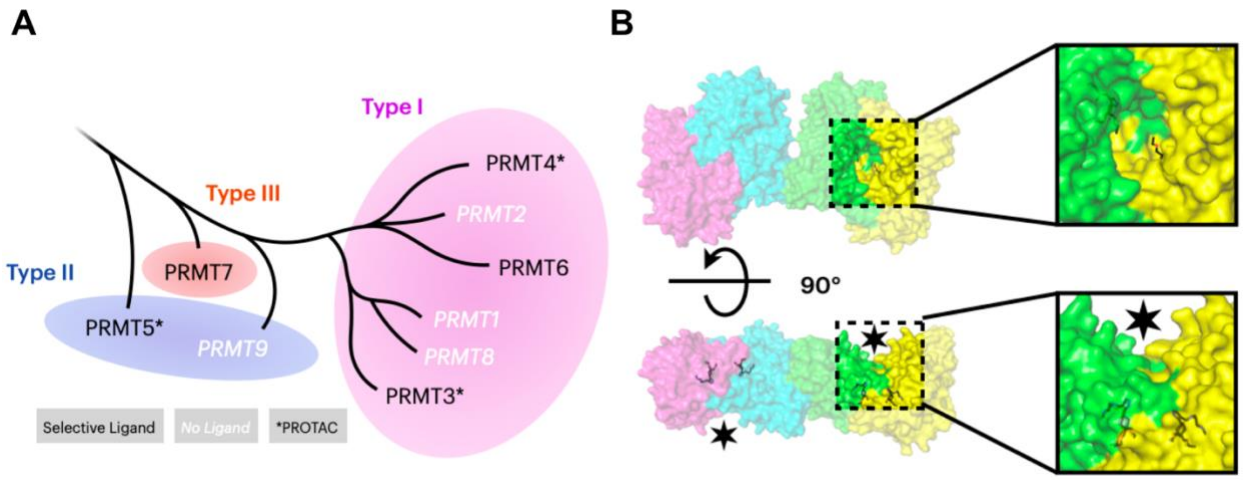

Figure 0.4 Chemical tractability of protein arginine methyltransferases (PRMTs)

(A) Phylogeny tree of the PRMT family organized by Type I, II and III. PRMTs with selective ligands are displayed in black, PRMTs without selective ligands are displayed in white, * denotes PRMTs with PROTACs. Phylogeny tree adapted from Boriack-Sjodin and Swinger 2015. **(B)** Binding mode of GSK3368715 to the PRMT1 tetramer from above (top) and from a side view (bottom), GSK3368715 shown in black and a star denotes the point of substrate entry (PRMT PDB 6NT2).

References for the Introduction

Balch, W. E., Morimoto, R. I., Dillin, A., and Kelly, J. W. Adapting proteostasis for disease intervention. Science 319, 916–919 (2008).

Li, K., and Crews, C. M. PROTACs: past, present and future. Chem. Soc. Rev. 51, 5214–5236 (2022).

Békés, M., Langley, D. R., and Crews, C. M. PROTAC targeted protein degraders: the past is prologue. Nat. Rev. Drug Discov. 21, 181–200 (2022).

Hinterndorfer, M. et al. Targeted protein degradation for cancer therapy. Nat. Rev. Cancer 25, 492-516 (2025).

Schneider, M. et al. The PROTACtable genome. Nat. Rev. Drug Discov. 20, 789–797 (2021).

Spradlin, J. N., Zhang, E., and Nomura, D. K. Reimagining druggability using chemoproteomic platforms. Acc. Chem. Res. 54, 1801–1813 (2021).

Chirnomas, D., Hornberger, K. R., and Crews, C. M. Protein degraders enter the clinic—a new approach to cancer therapy. Nat. Rev. Clin. Oncol. 20, 265–278 (2023).

Weng, G. et al. PROTAC-DB 2.0: an updated database of PROTACs. Nucleic Acids Res. 51, D1367–D1372 (2023).

Xiong, Y. et al. Chemo-proteomics exploration of HDAC degradability by small molecule degraders. Cell Chem. Biol. 28, 1514-1527 (2021).

Donovan, K. A. et al. Mapping the degradable kinome provides a resource for expedited degrader development. Cell. 183, 1714-1731 (2020).

Zhang, W. et al. Machine learning modeling of protein-intrinsic features predicts tractability of targeted protein degradation. Genomics, Proteomics Bioinf. 20, 882-898 (2022).

Martin, P. et al. Towards the targeted protein degradation of PRMT1. ChemMedChem 19, e202400269 (2024).

Crowe, C. et al. Mechanism of degrader-targeted protein ubiquitinability. Sci. Adv. 10, eado6492 (2024).

Huang, H. T. et al. Ubiquitin-specific proximity labeling for the identification of E3 ligase substrates. Nat. Chem. Biol. 20, 1227-1236 (2024).

Forte, N. et al. Targeted protein degradation through E2 recruitment. ACS Chem. Biol. 18, 897-904 (2023)

Loy, C. et al. ByeTAC: Bypassing E-Ligase-Targeting Chimeras for Direct Proteasome Degradation. J. Med. Chem. 68, 9694-9705 (2025).

Han, X., and Sun, Y. PROTACs: A novel strategy for cancer drug discovery and development. MedComm. 4, e290 (2023).

Poirson, J. et al. Proteome-scale discovery of protein degradation and stabilization effectors. Nature 629, 878-886 (2024).

Serebrenik, Y. V. et al. Pooled endogenous protein tagging and recruitment for systematic profiling of protein function. Cell Genom. 4, 100651 (2024).

Klionsky, D. J. et al. Guidelines for the use and interpretation of assays for monitoring autophagy (4th edition). Autophagy 17, 1–382 (2021).

Banik, S. M. et al. Lysosome-targeting chimaeras for degradation of extracellular proteins. Nature 584, 291-297 (2020).

Zhou, X., Xiao, Y., and Gao, Y. Challenges and opportunities for lysosome-targeting chimeras. Cell Rep. Phys. Sci. 6, 102778 (2025).

Li, Z. et al. Allele-selective lowering of mutant HTT protein by HTT–LC3 linker compounds. Nature 575, 203-209 (2019).

Schwalm, M. P. et al. Critical assessment of LC3/GABARAP ligands used for degrader development and ligandability of LC3/GABARAP binding pockets. Nat. Comm. 15, 10204 (2024).

Ji, C. H. et al. The AUTOTAC chemical biology platform for targeted protein degradation via the autophagy-lysosome system. Nat. Comm. 13, 904 (2022).

Dice, J. F. Peptide Sequences that target cytosolic proteins for lysosomal proteolysis. Trends Biochem. Sci. 15, 305-309 (1990).

Fan, X., Jin, W. Y., Lu, J., Wang, J., Wang, Y. T. Rapid and reversible knockdown of endogenous proteins by peptide-directed lysosomal degradation. Nat Neurosci. 17, 471-480 (2014).

Lv, L. et al. Acetylation targets the M2 isoform of Pyruvate Kinase for degradation through chaperone-mediated autophagy and promotes tumor growth. Mol. Cell 42(6) 719-730 (2011).

Zhao, Q. et al. o8G-modified circPLCE1 inhibits lung cancer progression via chaperone-mediated autophagy. Mol. Cancer 24, 82 (2025).

Wang, L., Klionsky, D. J., and Shen, H., The emerging mechanisms and functions of microautophagy. Nat. Rev. Mol. Cell Biol. 24, 186-203 (2022).

Li, J. et al. AMPK regulates ESCRT-dependent microautophagy of proteasomes concomitant with proteasome storage granule assembly during glucose starvation. PLoS Genet. 15, e1008387 (2019).

Nalawansha D. A. et al. LYMTACs: chimeric small molecules repurpose lysosomal membrane proteins for target protein relocalization and degradation. Nat. Comm. 16, 7812 (2025).

Zhang, Y. et al. ZZ-dependent regulation of p62/SQSTM1 in autophagy. Nat. Comm. 9, 4373 (2018).

Albrecht, L. V., Ploper, D., Tejeda-Muñoz, N., and De Robertis, E. M. Arginine methylation is required for canonical Wnt signaling and endolysosomal trafficking. Proc. Natl Acad. Sci. USA 115, E5317–E5325 (2018).

Franco, C. N. et al. Vitamin B6 is governed by the local compartmentalization of metabolic enzymes during growth. Sci. Adv. 9, eadi2232 (2023).

Maron, M. I. et al. Independent transcriptomic and proteomic regulation by type I and II protein arginine methyltransferases. iScience 24, 102971 (2021).

Schapira, M., Ferreira de Freitas, R. Structural biology and chemistry of protein arginine methyltransferases. Med. Chem. Commun. 5, 1779-1788 (2014).

Boriack-Sjodin, P. A., Swinger, K. K. Protein methyltransferases: a distinct, diverse and dynamic family of enzymes. Biochemistry 55, 1557-1569 (2016).

Lim, Y. et al. Multimerization of expressed protein-arginine methyltransferases during the growth and differentiation of rat liver. Biochim. Biophys. Acta. 1723, 240-247 (2005).

Dang, T. et al. Oligomerization of protein arginine methyltransferase 1 and its functional impact on substrate arginine methylation. J. Biol. Chem. 300, 107947 (2024).

Hwang, J. W., Cho, Y., Bae, G., Kim, S., Kim, Y.K. Protein arginine methyltransferases: promising targets for cancer therapy. Exp. & Mol. Med. 53, 788-808 (2021).

Chan, L. H. et al. PRMT6 regulates RAS/RAF binding and MEK/ERK-mediated cancer stemness activities in hepatocellular carcinoma through CRAF methylation. Cell Rep. 25, 690-701 (2018).

Larsen, S. C. et al. Proteome-wide analysis of arginine monomethylation reveals widespread occurrence in human cells. Sci. Signal. 9, rs9 (2016).

Uguen, M., Liu, T., James L. I., Frye S. V., Tudor-containing methyl-lysine and methyl-arginine reader proteins: disease implications and chemical tool development. ACS Chem. Biol. 20, 33-47 (2024).

Wang, Y., and Bedford, M. T., Effectors and effects of arginine methylation. Biochem. Soc. Trans. 51, 725-734 (2023).

Favia, A. et al. The protein arginine methyltransferases 1 and 5 affect Myc properties in glioblastoma stem cells. Sci. Rep. 9, 15925 (2019).

Chang, B., Chen Y., Zhao, Y., Bruick R. K., JMJD6 is a histone arginine demethylase. Science 318, 444-447 (2007).

Liu, H. et al. Clipping of arginine-methylated histone tails by JMJD5 and JMJD7. Prot. Natl Acad. Sci. USA 114, E7717-7726 (2017).

Hu, H. et al. Exploration of cyanine compounds as selective inhibitors of protein arginine methyltransferases: synthesis and biological evaluation. J. Med. Chem. 58, 1228-1243 (2015).

El-Khouiery, A.B. et al. Phase 1 study of GSK3368715, a type I PRMT inhibitor, in patients with advanced solid tumors. Br. J. Canc. 129, 309-317 (2023).

Lee, J., Kim, J., Hwang, I. Targeting PRMT5 in cancer: mechanistic insights and clinical progress. Biomed. Pharmacother. 193, 118754 (2025).

Shen, Y. et al. Discovery of first-in-class Protein Arginine Methyltransferase 5 (PRMT5) degraders. J. Med. Chem. 63, 9977-989 (2020).

Guo, Y. et al. Targeting PRMT5 through PROTAC for the treatment of triple-negative breast cancer. J. Exp. Clin. Cancer. Res. 30, 314 (2024).

Ju, Y. et al. Development of a selective and potent PRMT4 PROTAC degrader with efficacy against multiple myeloma in vitro and in vivo. J. Med. Chem. 68, 13973-13989 (2025).

Zou, W. et al. Discovery of PRMT3 Degrader for the Treatment of Acute Leukemia. Adv. Sci. 11, 2405963 (2024).

Lu, P. et al. Selective degradation of multimeric proteins by TRIM21-based molecular glue and PROTAC degraders. Cell 187, 7126-7142 (2024).

Shen, Y. et al. A first-in-class, highly selective and cell-active allosteric inhibitor of protein arginine methyltransferase 6. J. Med. Chem. 64, 3697-3706 (2021).

Prabhu, L. et al. Development of an AlphaLISA high throughput technique to screen for small molecule inhibitors targeting protein arginine methyltransferases. Mol. BioSyst. 13, 2509-2520 (2017).

CHAPTER 1

Methylarginine targeting chimeras for lysosomal degradation of intracellular proteins

Laurence J. Seabrook[1], Carolina N. Franco[2], Cody A. Loy [2], Jaida Osman[3], Callie Fredlender[2], Jan Zimak[4], Melissa Campos[1], Steven T. Nguyen[2], Richard L. Watson[5], Samantha R. Levine[4], Marian F. Khalil[2], Kaelyn Sumigray[6], Darci J. Trader[2,3] & Lauren V. Albrecht[1,2]

Affiliations

[1]Department of Developmental & Cell Biology, School of Biological Sciences, University of California, Irvine, Irvine, CA, USA.
[2]Department of Pharmaceutical Sciences, School of Pharmacy & Pharmaceutical Sciences, University of California, Irvine, Irvine, CA, USA.
[3]Department of Chemistry, School of Physical Sciences, University of California, Irvine, Irvine, CA, USA.
[4]Center for Neurotherapeutics, University of California, Irvine, Irvine, CA, USA.
[5]Department of Medicine, Division of Pulmonary & Critical Care, University of California, Los Angeles, Los Angeles, CA, USA.
[6]Department of Genetics, Yale School of Medicine, New Haven, CT, USA.

This chapter is derived from the manuscript published in Nature Chemical Biology:

Nat Chem Biol. 2024 Dec;20(12):1566-1576. doi: 10.1038/s41589-024-01741-y.

1.1 Abstract

A paradigm shift in drug development is the discovery of small molecules that harness the ubiquitin-proteasomal pathway to eliminate pathogenic proteins. Here we provide a modality for targeted protein degradation in lysosomes. We exploit an endogenous lysosomal pathway whereby protein arginine methyltransferases (PRMTs) initiate substrate degradation via arginine methylation. We developed a heterobifunctional small molecule, methylarginine targeting chimera (MrTAC), that recruits PRMT1 to a target protein for induced degradation in lysosomes. MrTAC compounds degraded substrates across cell lines, timescales and doses. MrTAC degradation required target protein methylation for subsequent lysosomal delivery via microautophagy. A library of MrTAC molecules exemplified the generality of MrTAC to degrade known targets and neo-substrates—glycogen synthase kinase 3β, MYC, bromodomain-containing protein 4 and histone deacetylase 6. MrTAC selectively degraded target proteins and drove biological loss-of-function phenotypes in survival, transcription and proliferation. Collectively, MrTAC demonstrates the utility of endogenous lysosomal proteolysis in the generation of a new class of small molecule degraders.

1.2 Introduction

Targeting protein stability with small molecule degraders is one of the most promising innovations in drug discovery (Balch et al., 2008; Li & Crews, 2022; Spradlin et al., 2021). Molecular glues and proteolysis targeting chimeras (PROTACs) induce the proximity of an E3 ligase and a target protein that becomes ubiquitinated for proteasomal destruction (Békés et al., 2022; Liu & Ciulli, 2023; Sakamoto et al., 2001). PROTACs are potent, and versatile and intensive research endeavors have resulted in 3,270 PROTAC molecules with over 28 in clinical trials (Li & Crews, 2022;

Spradlin et al., 2021; Chirnomas et al., 2023). Harnessing endogenous cellular proteolysis has the potential to expand druggable targets in the human proteome (20,000 proteins total) (Balch et al., 2008; Li & Crews, 2022; Spradlin et al., 2021). A recent study defines the 'PROTACtable' genome and reports that 98 distinct proteins have been degraded (Liu & Ciulli, 2023; Schneider et al., 2021; Weng et al., 2023). Incorporating alternative proteolytic pathways to build a broad palette of degrader modalities could further target proteins (Li & Crews, 2022; Bashore et al., 2023). For instance, ubiquitin-independent strategies have emerged that directly tether substrates to degradation machinery (Bashore et al., 2023; Ali et al., 2024; Takahashi et al., 2019; Ji et al., 2022; Fu et al., 2021; Li et al., 2019). The lysosome has provided a degrader modality for extracellular targets by exploiting endocytosis (Ahn et al., 2021; Banik et al., 2020; Ahn et al., 2023; Zhou et al., 2021; Caianiello et al., 2021). Intracellularly, lysosomes also catabolize macromolecules and diverse protein families (Wong & Cuervo 2010) and could provide new therapeutic opportunities.

There has been a renaissance in mapping naturally occurring proteolytic processes and degrons, amino acid sequences that regulate protein turnover (Varshavsky, 2019; Poirson et al., 2024; Owens et al., 2024; Ichikawa et al., 2022; Makaros et al., 2023; Lucas & Ciulli, 2017). Given their potential to inform degrader development, research endeavors have focused on identifying new degrons that enable E3 ligase recognition for degron ubiquitination and proteasomal degradation (Ichikawa et al., 2022; Makaros et al., 2023; Lucas & Ciulli, 2017; Nabet et al., 2018). Whether a naturally occurring and inducible degron for lysosomes, the alternative site of proteolysis could similarly be harnessed as a degrader is unknown. Recent work identifies arginine methylation as a lysosomal degron for intracellular proteins. Endogenously, type I protein arginine methyltransferase (PRMT) enzymes recognize and methylate substrates, which leads to lysosomal

degradation during homeostatic protein turnover (Albrecht et al., 2018; Franco et al., 2023). Because PRMTs are highly abundant enzymes that modify over one-third of human proteins (Larsen et al., 2016; Bedford & Clarke, 2009), a small molecule strategy capable of exploiting this pathway could offer a versatile tool for targeted protein degradation.

In this work, we evaluate whether synthetically inducing arginine methylation targets intracellular proteins for lysosomal degradation. We harness this new degradation pathway to develop a general chemical tool termed methylarginine targeting chimera (MrTAC), which uses heterobifunctional molecules that engage PRMT1 and a target protein. We show that MrTACs induce target protein methylation and degradation in the nanomolar range across diverse pathogenic targets and endogenous proteins. Together, this work provides evidence for a generalized degrader modality for intracellular proteins that is ubiquitin-independent and offers translational potential by exploiting a naturally occurring modification for lysosomes.

1.3 Results

Developing an intracellular lysosomal degrader platform

In physiological contexts, PRMT1 catalyzes arginine methylation (methylarginine degron, MrDegron) modifications on proteins that lead to their subsequent delivery into lysosomes(Albrecht et al., 2018; Franco et al., 2023). We sought to evaluate whether arginine methylation could be synthetically induced and exploited for targeted lysosomal degradation. Toward this goal, we developed a heterobifunctional MrTAC small molecule that simultaneously binds PRMT1 and a protein of interest (POI; **Figure 1.1a**). Ligand selection of endogenous proteins represents a major challenge in degrader development (Spradlin et al., 2021). Given this, we engineered a system to circumvent ligand screening for initial studies by generating a PRMT1–

HaloTag fusion protein and a POI–SNAP-tag fusion protein. HaloTag and SNAP-tag are dimerized by HaXS8 (Dotson & Ngo, 2022; Buckley et al., 2015; Erhart et al., 2013) through chloroalkane and benzylguanine ligands, respectively, which we repurposed as a MrTAC surrogate (denoted MrTAC^{HaXS8} (1); **Figure 1.7a**).

We hypothesized that recruiting PRMT1 with MrTAC will induce POI degradation. Glycogen synthase kinase 3β (GSK3β) was selected as an initial POI given its native regulation by PRMT1 (Albrecht et al., 2018) and its central role in tissue regenerative medicine, cancer and neurodegenerative disease (Kaidanovich-Beilin & Woodgett, 2011; Taelman et al., 2010). We first aimed to validate that covalent interactions between SNAP-tag and HaloTag could be induced by MrTAC^{HaXS8}. A GSK3β–SNAP-tag fusion protein was generated and cotransfected with an empty vector HaloTag control (lacking PRMT1) in HEK293T cells. Cells were treated with MrTAC^{HaXS8}, and GSK3β was evaluated by immunoblotting. In control treatments, GSK3β–SNAP was expressed at the expected monomeric molecular weight of 70 kDa (**Figure 1.1b**, lane 1). Upon MrTAC^{HaXS8} addition, GSK3β–SNAP shifted into ~110 kDa protein–protein complexes with empty HaloTag control. Complex formation gradually increased and was most efficient at 1 μM MrTAC^{HaXS8} (**Figure 1.1b**). Doses above 1 μM showed decreased complex formation, which is consistent with the hook effect, a phenomenon whereby the binary complex outcompetes the formation of a ternary complex (Douglass et al., 2013). Notably, total levels of GSK3β (monomer and complex) remained constant across all MrTAC^{HaXS8} doses (**Figure 1.1b**) validating that MrTAC^{HaXS8} induces Halo/SNAP proximity in our engineered cell system without degradative effects.

Chemically induced proximity with PRMT1 degrades GSK3β

Robust protein expression of GSK3β–SNAP and PRMT1–Halo in stably expressing HEK293 cells was confirmed by microscopy and immunoblot (**Figure 1.7b,c**). Next, DMSO or MrTAC^{HaXS8} treatments were performed, and protein levels were assessed after 24 h. GSK3β was entirely monomeric in DMSO-treated cells and shifted into complexes with PRMT1 with 0.1 nM MrTAC^{HaXS8} (**Figure 1.7c**). Notably, GSK3β degradation was observed with 1 nM MrTAC^{HaXS8}. The half-maximal degradation (DC_{50}) of GSK3β was 11.3 nM MrTAC^{HaXS8} (**Figure 1.1c**). In contrast, protein levels of endogenous and HaloTag-tagged PRMT1 remained constant across MrTAC^{HaXS8} treatment (**Figure 1.1c, Figure 1.7c**). To evaluate degradation kinetics, MrTAC dose curves were performed at shorter time points. GSK3β was robustly degraded by MrTAC^{HaXS8} after 3 h with a DC_{50} of 94.0 nM (**Figure 1.1d**). The hook effect was observed at 50 μM MrTAC^{HaXS8} with increasing monomeric GSK3β protein levels (**Figure 1.1c,d**). The higher DC_{50} for GSK3β at 3 h could be attributed to the improved efficiency of target degradation at 24 h (Haid et al., 2023). As seen with HEK293 stable lines, GSK3β was recruited and degraded by MrTAC^{HaXS8} in transiently transfected HEK293T and HeLa cells (**Figure 1.7d-g**). GSK3β degradation was similarly evident by fixed microscopy analyses comparing dimethylsulfoxide (DMSO) and MrTAC^{HaXS8} treatments for 3 h (**Figure 1.1e**). We next visualized MrTAC degradation of GSK3β in real time using live-cell microscopy. Cells expressing a GFP-tagged GSK3β–SNAP showed strong expression before treatment that was reduced by MrTAC^{HaXS8} after 30 min, supporting rapid GSK3β degradation (**Figure 1.1f**). Thus, MrTAC dose responses induce GSK3β degradation across timeframes and cell lines.

MrTAC drives the lysosomal degradation of cytosolic proteins

We next evaluated MrTAC-induced proteolytic mechanisms. Live-cell imaging showed that GSK3β reorganized into cytosolic puncta following treatment of MrTAC^{HaXS8} (**Figure 1.1f**). To evaluate whether these puncta were in fact representative of lysosomes, we visualized degradation in live cells that were stained with LysoTracker. MrTAC^{HaXS8} treatment drove stably expressed GSK3β–mCherry into puncta that overlapped with lysosomes within 25 min and over time, GSK3β fluorescence decreased (**Figure 1.2a**). Similar lysosomal delivery and degradation were observed with GSK3β–GFP upon MrTAC^{HaXS8} incubation (**Figure 1.8a**). Colocalization immunofluorescence was performed to evaluate MrTAC^{HaXS8} trafficking of GSK3β into lysosomal puncta marked by lysosomal-associated membrane protein 1 (LAMP-1) in fixed cells (**Figure 1.8b**). Proximity ligation assays (PLAs) were used as an orthogonal approach to evaluate substrate internalization into lysosomes. This assay monitors fluorescent signals that are generated from polymerase-driven rolling circle amplification when two protein targets are within 40–100 nm (Weibrecht et al., 2010) (**Figure 1.2b**). Cells were stained with anti-Flag antibody to recognize GSK3β and costained with a luminal LAMP-1 antibody to report lysosomal internalization. Compared to DMSO treatments, MrTAC^{HaXS8} increased PLA signal in GSK3β–LAMP-1 cells, whereas IgG antibody control pairs were negative (**Figure 1.2b**). These analyses using live imaging, fixed imaging and PLA show that MrTAC spatially redirects cytosolic GSK3β into lysosomes.

During cell growth, lysosomal delivery of methylated GSK3β occurs within the minute timescale (Albrecht et al., 2018; Taelman et al., 2010). Given that the induced kinetics of GSK3β trafficking into lysosomes by MrTAC^{HaXS8} similarly occurred within minutes, we next probed into the mechanisms of our synthetically induced GSK3β proteolytic process. To ensure that GSK3β was

specifically degraded in lysosomes, cells were treated with MrTAC^{HaXS8} for 24 h in the presence of lysosomal or proteasomal inhibitors. Notably, the lysosomal inhibitor bafilomycin significantly stabilized the MrTAC complex fourfold (compare lanes 2 and 4), while proteasomal inhibitors, bortezomib or MG132, had no effect (**Figure 1.2c**). This evidence supports that MrTAC^{HaXS8} induces lysosomal GSK3β proteolysis.

To further study the mechanism of MrTAC proteolysis, we used a genetic approach to disrupt lysosomal degradation. Proteins are delivered into lysosomes via the following three distinct forms of autophagy: (macro)autophagy, chaperone-mediated autophagy (CMA) and microautophagy (Wong & Cuervo, 2010; Klionsky et al., 2021; Sahu et al., 2011). Previous work demonstrates that native delivery of methyl substrates via MrDegron modifications occurs through microautophagy, which is coordinated by endosomal sorting complexes required for transport (ESCRT) signaling (Albrecht et al., 2018; Taelman et al., 2010). During microautophagy, vacuolar protein sorting 4 (VPS4) mediates the final step of invagination of the lysosomal membrane (El-Khouiery et al., 2023). To evaluate the role of microautophagy in MrTAC degradation, colocalization analyses were performed with GSK3β and VPS4 in cells expressing either wild-type VPS4 or dominant-negative VPS4. MrTAC^{HaXS8} led to colocalization of GSK3β and wild-type VPS4–GFP across cell types (**Figure 1.8c,d**). However, GSK3β entry into lysosomes was ablated by expression of a dominant-negative VPS4–GFP (**Figure 1.8c,d**). To evaluate the necessity of microautophagy for MrTAC degradation, MrTAC^{HaXS8} GSK3β degradation assays were performed in cells treated with siRNA against *VPS4A* (**Figure 1.8e**). Cells treated with si*VPS4A* showed a complete rescue of GSK3β protein levels during MrTAC^{HaXS8} treatment (**Figure 1.2d**). In contrast, knockdown of macroautophagy or CMA with siRNA against *ATG7* or *LAMP2*, respectively, were unable to

rescue MrTAC^{HaXS8} degradation of GSK3β (**Figure 1.2d, Figure 1.8e**). Furthermore, MrTAC^{HaXS8} treated cells lacked GSK3β localization with lysosomes in si*VPS4A* cells compared to control treatment (**Figure 1.2e**). Rescue by either pharmacological or genetic-based targeting of lysosomal activity supports that MrTAC co-opts endogenous degradation machinery, representing the first application of microautophagy for targeted protein degradation.

Induced methylation by MrTAC primes substrate degradation

In naturally occurring methyl-driven proteolysis, PRMT1 catalyzes asymmetric dimethylarginine (ADMA) modifications to mark substrates with MrDegrons for lysosomal delivery (Albrecht et al., 2018; Franco et al., 2023). We examined whether synthetically induced PRMT1 proximity by MrTAC led to GSK3β methylation. To first detect substrate methylation within native cellular environments, PLA assays were performed (Varshavsky, 2019) using antibodies recognizing the Flag tag on GSK3β–SNAP and ADMA. Compared to DMSO controls, MrTAC^{HaXS8} treatment resulted in a fivefold increase in PLA signal, demonstrating induced methylation (**Figure 1.3a**). PLA signal was absent in cells incubated with IgG control antibody pairs. To identify the arginine methylation sites, liquid chromatography–mass spectrometry (LC–MS) was used to evaluate GSK3β from in vitro reactions with or without purified PRMT1 protein. GSK3β was methylated at conserved arginine residues within an N-terminal intrinsically disordered region and within surface-exposed arginine residues 96, 102 and 111 (**Figure 1.3b, Figure 1.9a**). Next, LC–MS was used to study GSK3β arginine methylation in cells treated with MrTAC^{HaXS8} by isolating GSK3β–MrTAC–PRMT1 complexes from cultured HEK293 cells. Cells were treated with MrTAC^{HaXS8}, and complexes were immunoprecipitated using magnetic anti-Flag beads that recognized GSK3β. By LC–MS, PRMT1 and GSK3β peptides were both present, confirming successful protein–

protein interaction (**Figure 1.9b**). Consistent with the in vitro assays, GSK3β was methylated at multiple arginine residues, including native sites identified in vitro and at new sites (**Figure 1.9b**). These data indicate that inducing PRMT1 proximity with MrTAC is sufficient for GSK3β methylation.

We hypothesized that MrTAC induces protein methylation to drive targeted lysosomal proteolysis. To confirm that PRMT1 methyltransferase activity is required for MrTAC degradation, $MrTAC^{HaXS8}$ treatments were performed in the presence of GSK3368715, a selective type I PRMT inhibitor (El-Khoueiry et al., 2023). $MrTAC^{HaXS8}$ induced GSK3β degradation at expected doses, while co-incubation of $MrTAC^{HaXS8}$ with GSK3368715 had no effect, suggesting that GSK3β methylation precedes degradation (**Figure 1.3c**). To further substantiate these data, we used a genetic approach using a catalytically dead PRMT1 mutant, which has been comprehensively characterized to disrupt enzymatic activity, by replacing residues in the *S*-adenosyl methionine (SAM) binding site (VLD to AAA) (Albrecht et al., 2018; Bedford & Clarke, 2009; Kim et al., 2023). Stable cell lines were generated to express a Halo-tagged fusion of the catalytically dead PRMT1 (denoted $PRMT1^{Dead}$), and $MrTAC^{HaXS8}$ assays were performed. GSK3β protein levels were unaffected by $MrTAC^{HaXS8}$ treatments in $PRMT1^{Dead}$ stable cells (**Figure 1.3d**), as seen with methyl inhibitor analyses. Together, pharmacologic- or genetic-based inhibition of methyltransferase activity rescues the effects of MrTAC and supports a model that methylation drives MrTAC degradation.

MrTAC phenocopies loss-of-function biological responses

GSK3β regulates canonical WNT signaling during cell growth, embryogenesis and tissue regeneration (Kaidanovich-Beilin & Woodgett, 2011; Hooper et al., 2008). Upon stimulation, WNT ligands bind to membrane receptors, and cytosolic GSK3β becomes sequestered into lysosomes, which allows β-catenin to accumulate and initiate transcriptional activity (Bilic et al., 2007; Clevers & Nusse, 2012). Given this, we evaluated whether synthetically induced GSK3β degradation recapitulated physiological WNT signaling. Immunoblotting confirmed that MrTAC^{HaXS8} degradation of GSK3β–SNAP was maintained across several days (**Figure 1.4a**) and was sufficient to stabilize total levels of β-catenin compared to DMSO (**Figure 1.4b**). Using cells that stably express GSK3β–SNAP by CRISPR integration, we sought to evaluate the downstream consequences of targeted GSK3β degradation by directly comparing control and MrTAC^{HaXS8} treatments. In these cells, MrTAC^{HaXS8} significantly increased WNT target genes *MYC* (also known as *c-MYC*) and *BIRC5* relative to DMSO treatment (Clevers & Nusse, 2012) (**Figure 1.4c**). Finally, cell growth assays were performed to test whether induced GSK3β degradation would be sufficient to increase proliferation as seen during WNT signaling. Compared to DMSO treatment, MrTAC^{HaXS8} significantly increased rates of proliferation in cells co-expressing PRMT1–Halo and GSK3β–SNAP (**Figure 1.4d, Figure 1.10a**). By contrast, no significant changes were observed during drug treatment in control cells, which included nontransfected cells and cells expressing control Halo or SNAP empty vectors (**Figure 1.10a**). PRMT1 protein levels were stable across treatments (**Figure 1.10b**). These data directly comparing DMSO and MrTAC^{HaXS8} using stably integrated cells suggest that MrTAC reduction of global GSK3β protein levels promotes growth phenotypes.

Generalizability of MrTAC for neo-substrate degradation

We next aimed to extend MrTAC as a proof-of-concept degrader modality by targeting proteins that are classically degraded in proteasomes. MYC is a nuclear transcription factor that regulates myriad growth processes and is the most frequently upregulated oncogene in cancer (Kress et al., 2015; Chen et al., 2018). Despite intensive efforts and drug campaigns, MYC is recalcitrant to small molecules and considered undruggable (Kress et al., 2015; Chen et al., 2018, Boike et al., 2021). This prompted us to evaluate whether human MYC could be targeted specifically to lysosomes via MrTAC (**Figure 1.4e**). Human MYC was fused with SNAP-tag and expressed in HEK293 cells containing CRISPR-integrated PRMT1–Halo. We first confirmed that MrTAC^{HaXS8} could induce monomeric MYC (70 kDa) into complexes with PRMT1–Halo (150 kDa) at 0.01 μM MrTAC^{HaXS8} (**Figure 1.4e**). MrTAC doses above 0.1 μM MrTAC^{HaXS8} corresponded with decreased MYC protein levels after 24 h, indicative of degradation. Immunofluorescence analyses were performed to evaluate the cellular distribution of MYC. DMSO-treated cells displayed MYC localization in nuclear and cytosolic cellular compartments. By contrast, MrTAC^{HaXS8} treatment led to the colocalization of MYC with an arginine methylation antibody (**Figure 1.10c**) and lysosomes marked by LAMP-1 (**Figure 1.10d**). These data indicate that MrTAC could degrade and relocalize SNAP-tagged MYC.

To confirm that lysosomal activity was responsible for MYC proteolysis, short-term MrTAC assays were performed in the presence of lysosomal or proteasomal inhibitors. Assays were performed at short time points using cycloheximide, which inhibits protein synthesis, to enable sensitive analysis of protein turnover. During MrTAC^{HaXS8} treatment, MYC was readily incorporated into ternary complexes within 30 min (**Figure 1.10e**). The lysosome inhibitor bafilomycin stabilized the ternary complex, while the proteasome inhibitor MG132 had no

stabilizing effect, supporting that induced MYC degradation was mediated through lysosomes (**Figure 1.10e**). Given the role of MYC in cell growth, we next used our engineered system to test whether inducing degradation of MYC with MrTAC^{HaXS8} would be sufficient to decrease proliferation rates. DMSO or MrTAC^{HaXS8} treatments were performed in HeLa cells co-expressing MYC–SNAP and PRMT1–Halo constructs, and cell numbers were counted across 7 days. Direct comparisons between engineered cell lines showed that MrTAC^{HaXS8} treatments were associated with significantly decreased cell density after 7 days compared to DMSO (**Figure 1.4f**). Together, these assays hint at the tractability of MrTAC as a generalizable degrader toward neo-substrates.

MrTAC degrades endogenous protein targets

Degrader therapeutics rely on endogenous cellular machinery to mediate target protein degradation (Li & Crews, 2022, Chirnomas et al., 2023). The proof-of-concept degradation of multiple target proteins using SNAP-tag and MrTAC^{HaXS8} suggested that endogenous, untagged proteins could also be targeted for degradation by replacing the SNAP ligand with an endogenous protein binder. Bromodomain-containing protein 4 (BRD4) is an essential protein in mammalian biology that has been strongly linked to cancer and inflammatory diseases (Belkina & Denis, 2012). BRD4 is widely used as a model substrate in developing degrader modalities, as highlighted by ARV-825, A-1874, dBET1 and MZ-1 (Winter et al., 2017; Young et al., 1998; Hines et al., 2019). BRD4 has a well-established ligand, JQ1, with a binding affinity of 42 nM (half-maximal inhibitory concentration, IC_{50}) to the first bromodomain (Zengerle et al., 2015). Given disease relevance and a defined ligand, we nominated BRD4 as our first candidate to evaluate endogenous protein degradation using MrTAC. Three-dimensional molecular modeling was performed using the first bromodomain of BRD4 cocrystallized with JQ1 (Protein Data Bank (PDB) code: 3MXF) with

HaloTag (PDB code: 6U32) to develop a MrTAC compound that could engage BRD4 and PRMT1–Halo without steric or electrostatic clash (**Figure 1.11a**). From this, we synthesized a chloroalkane-derivatized JQ1 warhead using a polyethylene glycol (PEG) linker length of two units, which is denoted $MrTAC^{JQ1}$ (2) (**Figure 1.5a**). To evaluate target degradation, dose responses of $MrTAC^{JQ1}$ or $Control^{JQ1}$ (JQ1-PEG2-NH (3)) treatments were performed in HEK293 cells stably expressing PRMT1–Halo, and BRD4 levels were measured by immunoblotting. Compared to the control treatment, BRD4 protein levels were significantly reduced at 100 nM $MrTAC^{JQ1}$ where it also reached its D_{max} (**Figure 1.5b, Figure 1.11b**). PRMT1 protein levels were constant in control or $MrTAC^{JQ1}$ treatments (**Figure 1.11c**). Similarly, BRD4 protein levels were reduced in immunofluorescence microscopy analyses of $MrTAC^{JQ1}$-treated cells (**Figure 1.5c**). Co-immunoprecipitation of PRMT1 showed that BRD4 interactions were induced by $MrTAC^{JQ1}$ (**Figure 1.5d**). We note that cells were incubated with proteolytic inhibitors to resolve protein–protein interactions, as in previous studies (Simpson et al., 2020).

We next sought to evaluate a target from a different protein family. Histone deacetylase 6 (HDAC6) is a critical enzyme that is found in the cytoplasm and associates with microtubule cytoskeletal components (Lee et al., 2008). Given the central role of HDAC6 in several human diseases (Haberland et al., 2009), extensive drug discovery efforts have been devoted to developing HDAC6 ligands. Vorinostat, also known as suberoylanilide hydroxamic acid (SAHA), is a US Food and Drug Administration (FDA)-approved therapeutic and a potent ligand of HDAC6 with an IC50 value of 40.9 nM (Lee et al., 2008; Bradner et al., 2010; Hanswillemenke et al., 2024). We repurposed a previously synthesized chloroalkane-derivatized-SAHA molecule (Ohana et al., 2015) to enable PRMT1 recruitment to HDAC6, denoted $MrTAC^{SAHA}$ (4) (**Figure 1.5e**).

Dose–response assays with MrTAC^{SAHA} or control^{SAHA} (SAHA ligand) were performed in the aforementioned HEK293 stable line, and protein levels were evaluated by immunoblotting (**Figure 1.5f**). While HDAC6 levels were unchanged in cells treated with control^{SAHA}, a notable reduction of HDAC6 was observed in 100 nM MrTAC^{SAHA} treatments with a D_{max} occurring at 10 μM MrTAC^{SAHA} (**Figure 1.5f, Figure 1.11d**). PRMT1 protein levels and localization were unaffected by MrTAC^{SAHA} (**Figure 1.11e,f**). Furthermore, HDAC6 was also degraded in HeLa cells expressing PRMT1–Halo with a D_{max} at 1 μM MrTAC^{SAHA}, and a hook effect occurred above 5 μM (**Figure 1.11g**). Finally, microscopy immunofluorescence staining of endogenous HDAC6 further demonstrated that protein levels were reduced by MrTAC^{SAHA} in HEK293 (**Figure 1.5g**) or HeLa cells (**Figure 1.11g**). Co-immunoprecipitation assays confirmed that PRMT1 interactions were selectively induced with HDAC6 in cells treated with MrTAC^{SAHA} (**Figure 1.5h**). HDAC6 is typically degraded in the proteasome (Harberland et al., 2009), which suggests that MrTAC enables endogenous neo-substrate activity by inducing HDAC6 lysosomal proteolysis. To confirm this possibility, we performed degradation experiments in the presence of proteasome or lysosome inhibitors. In MrTAC^{SAHA}-treated cells, lysosomal inhibition stabilized HDAC6 levels, while proteasomal inhibition was unable to prevent degradation (**Figure 1.11h**). Hence, these data support a model whereby methyl-induced proteolysis by MrTAC has generalizability toward endogenous proteins.

MrTAC phenocopies loss-of-function for endogenous proteins

To further confirm the selectivity of target degradation, we next sought to determine whether downstream responses mimicked loss-of-function phenotypes with target proteins. Cells treated with MrTAC^{JQ1} reported *BCL2* and *BIRC3* (also known as *cIAP2*) downregulation and *CDKN1A*

(*P21*) upregulation (**Figure 1.6a**), consistent with previous BRD4 loss-of-function studies (Zengerle et al., 2015). *BRD4* transcript levels were unaffected, as expected. BRD4 has established roles in cell growth and proliferation (Hu et al., 2015). Consistent with this, cell proliferation rates were significantly reduced following 6 days of treatment with $MrTAC^{JQ1}$ compared to the $Control^{JQ1}$ compound (**Figure 1.6b, Figure 1.12a**). To extend HDAC6 degradation studies, we next examined whether $MrTAC^{SAHA}$ was sufficient to recapitulate classic HDAC6 loss-of-function phenotypes. HDAC6 is a deacetylase enzyme and is known to promote proliferation across multiple cell types and tissues including HEK293 cells used here (Li et al., 2015). Given this, we first evaluated whether targeted degradation of HDAC6 was sufficient to impact the acetylation status of a known substrate, tubulin (Tran et al., 2007). $MrTAC^{SAHA}$ treatments led to a 15-fold increase in acetylated tubulin levels relative to total tubulin (**Figure 1.6c**). To determine whether targeted HDAC6 degradation would similarly recapitulate biological responses after longer time points, we evaluated cell survival. $MrTAC^{SAHA}$-treated cells significantly reduced survival compared to cells not expressing PRMT1–Halo (**Figure 1.6d**). PRMT1 protein levels were unaffected by $MrTAC^{SAHA}$ treatments (**Figure 1.12b**). In HDAC6-depleted cells, levels of other HDAC family members were unaffected, confirming the selectivity of MrTAC (**Figure 1.6e**). These data suggest that selective depletion of endogenous proteins by MrTAC recapitulates loss-of-function phenotypes on cell function.

Our model supports a mechanism whereby methylation is induced by proximity with PRMT1 to enable lysosomal degradation. To evaluate methylation requirements for endogenous degradation, we evaluated MrTAC in $PRMT1^{Dead}$ or wild-type PRMT1 stable cell lines. While HDAC6 was reduced by $MrTAC^{SAHA}$ in wild-type PRMT1 cells, protein levels in $PRMT1^{Dead}$ cells were

unchanged and consistent across treatments (**Figure 1.6f,g**). These data further support that methylation drives targeted degradation by MrTAC of endogenous proteins in living cells. Collectively, MrTAC harnesses an entirely natural proteolytic pathway and opens a new class of degraders for basic research and clinical development.

1.4 Discussion

MrTAC is a small molecule that induces the proximity of PRMT1 with a target protein. With the recent discovery of the naturally occurring MrDegron (Albrecht et al., 2018; Franco et al., 2023), we evaluated whether synthetically inducing protein methylation could enable targeted proteolysis. We demonstrate that MrTAC degrades diverse substrates with distinct structural features, turnover kinetics and subcellular locations. We also show that MrTAC is amenable toward both canonical MrDegron targets and neo-substrates, which are typically degraded in proteasomes. Engineering a dual-covalent MrTAC system enabled step-wise tracking of (1) complex formation by immunoblot, (2) target protein methylation by LC–MS, (3) lysosomal delivery by live-cell imaging, (4) degradation by immunoblot/microscopy, and (5) functional effects of protein depletion. Finally, the use of a catalytic MrTAC to engage endogenous proteins led to the lysosomal proteolysis of two substrates with well-defined ligands, BRD4 and HDAC6.

The lysosome is a fundamental organelle across all tissues and is responsible for the catabolism of diverse protein families and macromolecular structures Perera & Zoncu, 2016). Additionally, lysosomes degrade proteins that are inaccessible to proteasomes, such as aggregates or targets with extended repeat motifs (Wong & Cuervo, 2010). Extracellular and membrane proteins can be degraded by endocytosis-lysosomal TPDs such as lysosomal-targeting chimeras (Ahn et al., 2021;

Banik et al., 2020), bispecific aptamer chimera (Miao et al., 2021), AbTAC (Cotton et al., 2021), GlueTAC (Hsia et al., 2024) and MoDE-A (Zhou et al., 2021). Within cells, macroautophagy sequesters proteins into autophagosomes that fuse onto lysosomes during fasting (Klionsky et al., 2021) and can be exploited by autophagy-targeting chimeras that induce target K63-ubiquitination (Takahashi et al., 2019). Subsequent strategies, ATTEC (Fu et al., 2021; Bao et al., 2024) and AUTOTAC (Ji et al., 2022), have since emerged, which tether substrates to autophagosomes. To combat cell-type variability of basal macroautophagy activity (Klionsky et al., 2021), AUTOTAC deploys a two-step mechanism that tethers substrates to p62 and stimulates autophagosome biogenesis. Microautophagy is constitutively active and delivers proteins via ESCRT machinery proteins with VPS4 operating at the critical final step (Sahu et al., 2011; Wang et al., 2023). MrTAC synthetically triggers methyl-driven proteolysis via microautophagy (Albrecht et al., 2018; Franco et al., 2023), which may have benefited by circumventing autophagosomes or ubiquitination.

PROTACs use natural degradative tags to selectively eliminate pathogenic proteins, and over 28 PROTACs have entered clinical trials (Chirnomas et al., 2023). MrTAC uses a natural but entirely distinct proteolytic pathway in lysosomes and an alternative degradative tag, arginine methylation. Acquired resistance to PROTACs has been linked to lysine mutations that block ubiquitin-proteasomal targeting (Chirnomas et al., 2023; Bashore et al., 2023). MrTAC is independent of ubiquitin and ligases, which have cell-type specific expression profiles (Chirnomas et al., 2023), and would not be impacted by lysine mutations. The chemical biology field has widely adopted the use of encoded degron tags that respond to small molecules, such as dTAGs, that enable targeted degradation of genetically modified proteins (Nabet et al., 2018; Nabet et al., 2020). We

show that MrTAC can similarly degrade proteins that lack endogenous ligands by incorporating fusion proteins for lysosomal proteolysis, which opens new possibilities for functional dissection of biological pathways in engineered living systems. Previously, HaloTag was used in PROTAC studies with ligands toward von Hippel-Lindau ligase and cereblon (Buckley et al., 2015). Our study extends this by incorporating HaloTag and SNAP-tag together to study a new degrader modality, given the absence of an established silent PRMT1 ligand recruiter. Our dual-covalent approach enabled feasible detection of ternary complex dynamics, which offered insight into MrTAC kinetics and mechanism. This approach could be readily extended to other degrader modalities like PROTAC to study complex features like substrate PROTACtability and kinetics (Schneider et al., 2021; Weng et al., 2023).

Methylation orchestrates fundamental biological processes by modifying diverse substrates such as proteins, nucleic acids, metabolites and lipids (Bedford et al., 2009). A proximity-based small molecule inducer of methylation could offer a valuable resource across a spectrum of research settings but has yet to be developed. In this study, we present a first-in-class proximity inducer of protein methylation, which we applied for targeted degradation. A growing body highlights proximity inducers of protein phosphorylation and acetylation modifications with phosphorylation-inducing chimeric small molecules and AceTAG, respectively (Wang et al., 2021; Siriwardena et al., 2020; Hines et al., 2013). Inducing methylation now broadens the range of tools available and could be used across a spectrum of fields. Previous drug development efforts have yielded effective PRMT inhibitors in cancer therapeutics (Wu et al., 2021). The potential clinical benefits of using PRMT1 activity for targeted protein degradation warrant future work to discover noncovalent, silent PRMT1 ligands for substoichiometric catalysis.

1.5 Methods

Antibodies

Antibodies used for western blots, immunofluorescence and PLA are as follows: anti-Flag (Sigma-Aldrich, 1804), anti-SNAP-tag (New England Biolabs, P9310S), anti-actin (Sigma-Aldrich, A1978), anti-LAMP-1 (D2D11; Cell Signaling Technology, 9091), anti-GSK3β (Enzo Life Sciences, ADI-KAP-ST002), anti-PRMT1 (Sigma-Aldrich, SAB2702290), anti-ADMA (21C7; Abcam, Ab413), anti-LAMP2A (EPR4207(2); Abcam, ab125068), anti-ATG7 (D12B11; Cell Signaling Technology, 8558), anti-VPS4 (Sigma-Aldrich; SAB4200025), anti-H3 (96C10; Cell Signaling Technology, 3638), anti-HDAC6 (D2E5; Cell Signaling Technology, 7558), anti-acetyl-α-tubulin (Lys40; D20G3; Cell Signaling Technology, 5335), anti-α-tubulin (DM1A; Cell Signaling Technology, 3873) and anti-BRD4 (Thermo Fisher Scientific, A301-985A-T). Antibodies were used at 1:300 dilutions for immunofluorescence with the exception of ADMA (1:50), BRD4 (1:200) and HDAC6 (1:200). Antibodies were used for immunoblot at 1:1,000.

Cell culture

All cells were obtained from American Type Culture Collection (ATCC). Cells were cultured in DMEM supplemented with 10% heat-inactivated FBS (Gibco), 1% penicillin–streptomycin, 0.25 mg ml^{-1} plasmocin (InvivoGen; ant-mpp) and 1% glutamine. The cells were maintained at 37 °C and 5% CO2. Media was replenished every 2–3 days and passaged with 0.25% trypsin when cells reached ~75% confluency. Cells were routinely tested with the MycoStrip Mycoplasma Detection Kit (InvivoGen; rep-mys). Cells were transfected using Lipofectamine 2000 as per manufacturer instructions.

Stable HEK293 cell lines expressing wild-type or catalytically dead (92-VLD/AAA-95) PRMT1–HaloTag were generated by plasmid transfection and selection for 2 weeks in 500 μg ml^{-1} G418. Cells co-expressing GSK3β–SNAP–mCherry–Flag were generated by plasmid transfection and selection for 2–3 weeks in 100 μg ml^{-1} zeocin. Cells were maintained in 0.5x selection media.

For HEK293T cell lines with CRISPR insertion of either PRMT1–Halo or PRMT1–Halo/GSK3β–SNAP, homology-independent targeted insertion (HITI) was used as previously described. HEK293T cells were transfected with PRMT1–Halo or PRMT1–Halo/GSK3β–SNAP constructs, Cas9 and gRNA targeting a safe harbor in chromosome 19 using Lipofectamine 3000 as per manufacturer instructions. Cells were selected for 4 weeks in 100 μg ml^{-1} zeocin. Cells were sorted and maintained in 100 μg ml^{-1} zeocin for 1-week postsort to ensure high stable expression.

Chemical synthesis

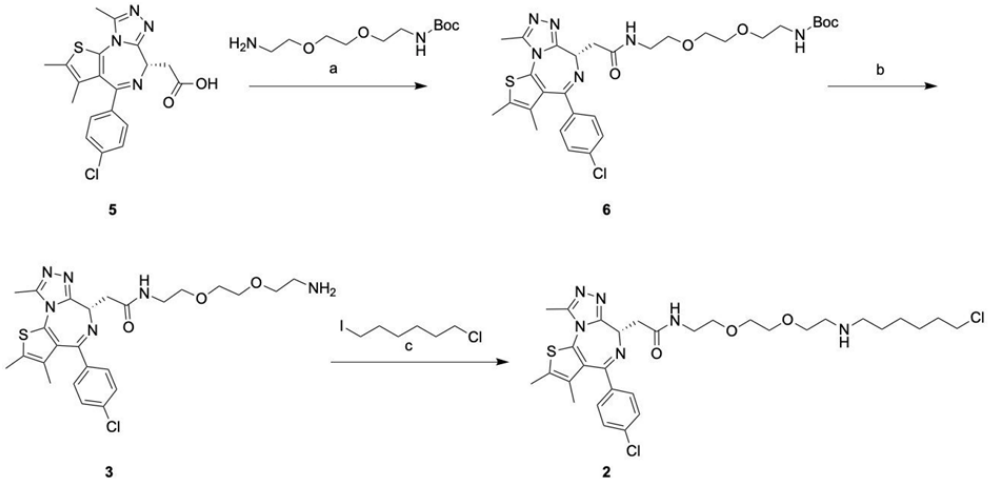

All anhydrous solvents were used under nitrogen. Purification was performed on Agilent 1260 Infinity II Analytical HPLC reverse phase with scalar (c18) column. The reactions were monitored

by thin layer chromatography (TLC) and/or LCMS on Agilent 1260 Infinity II system with Single Quadrupole LC/MS System. (S)-2-(4-(4-chlorophenyl)-2,3,9-trimethyl-6H-thieno[3,2-f][1,2,4]triazolo[4,3-a][1,4]diazepin-6-yl)acetic acid (JQ1-COOH) was purchased from BLDpharm, 1-Chloro-6-iodohexane was purchased from Thermo Fisher Scientific. Tert-Butyl (2-(2-(2-aminoethoxy)ethoxy)ethoyl)carbamate was purchased from AmBeed.

Step a: To a stirred solution of (S)-2-(4-(4-chlorophenyl)-2,3,9-trimethyl-6H-thieno[3,2-f][1,2,4]triazolo[4,3-a][1,4]diazepin-6-yl)acetic acid (**5**, JQ1-COOH) (1 eq), HOBT.H_2O (1.5 eq.), and EDC (1.5 eq.) in THF, DIPEA (6 eq.) was added and left to stir for 15 minutes before addition of the corresponding BOC protected PEG linker. After linker addition, reaction mixture was stirred at room temperature for 12 h. Upon completion of reaction (TLC monitoring and LCMS), the reaction mixture was poured into a saturated $NaHCO_3$ solution and extracted with ethyl acetate. Organic layers washed with water and brine, dried over anhydrous sodium sulfate and solvent removed under vacuum. The crude product (**6**) was moved forward without purification.

Step b: To a solution of **6** in DCM, 95% TFA was added. The reaction mixture was stirred at rt for 1 hr. After reaction completion (TLC monitoring), the reaction mixture was poured into saturated $NaHCO_3$. solution, and extracted with DCM 3x. The organic layers were washed with water and brine, dried over anhydrous sodium sulfate and the solvent removed under vacuum. Crude product (**3**) was subjected to the next step without further purification.

Step c: To a solution of **3** (1 eq) in THF, 1-Chloro-6-iodohexane (3 eq.) and DIPEA (6 eq.) was added. The reaction mixture was allowed to stir at rt for 12 hr. Upon completion of the reaction

(TLC monitoring), the reaction mixture was poured into saturated $NaHCO_3$ solution and extracted with ethyl acetate. Organic layers washed with water and brine, dried over anhydrous sodium sulfate and solvent removed under vacuum. The crude product (**2**) was purified by HPLC with a scalar (c18) column and analyzed by HRMS (**Figure S1.7**).

Plasmids

All primers were obtained from IDT. Halo–PRMT1–MYC vector was generated by ligating HaloTag (Addgene, 154144) into the PRMT1 plasmid (OriGene, RC224239) via EcoRI/KpnI; HaloTag primers were as follows: forward 5′-gatcgaattcccaccatggcagaaatcggtactgg-3′ and reverse 5′gatcggtaccggcgtttctcgttcagctttttgtacaaacttgtacc-3′. Catalytically dead PRMT1 was generated using the QuikChange site-directed mutagenesis kit (Agilent, 200523) according to the manufacturer's instructions using the following primers: forward 5′-cttcaaggacaaggtggcggcggccgtcggctcgggcaccggcatc-3′ and reverse 5′-gatgccggtgcccgagccgacggccgccgccaccttgtccttgaag-3′. The SNAP–GSK3β–Flag vector was generated by replacing *PRMT1* (OriGene, RC224239) with GSK3β using KpnI/NotI. *GSK3B* primers were as follows: forward 5′-gatcggtaccgtcagggcggcccagaaccacctcctttgc-3′ and reverse 5′-gatccggccgcggggtggagttggaagctgatgcagaag-3′ (GSK3β plasmid was a gift from W. Wang, UniProt P49841-2). The SNAP-tag gene (Addgene, 101135) was inserted into the GSK3β C terminus via EcoRI/KpnI. SNAP-tag primers were as follows: forward 5′-gatcgaattcccaccatggacaaagactgcgaaatgaagc and reverse 5′-gatcggtaccggctcgagggatcctggcgc-3′. Halo–PRMT1 and SNAP–GSK3β (GGS)2 linkers were added with 5′-phospho PCR ligation using the following primers: forward 5′p-tcagggcggcccagaac-3′ and reverse 5′p-actaccaccactaccaccacctgcaggacccagcc-3′, and forward 5′p-tcagggcggcccagaaccacctcc-3′ and

reverse 5′p-actaccaccactaccaccctcgagggatcctggcgc-3′, respectively. The 5′-phospho PCR ligation was performed again with the following primers to remove unneeded affinity tags: forward 5′p-taaacggccggccgcg-3′ and reverse 5′p-cagatcctcttctgagatgagtttctgctcgag-3′, and forward 5′p-gattacaaggatgacgacgataaggtttaaacggc-3′ and reverse 5′p-ggtggagttggaagctgatgcagaag-3′. The SNAP–GSK3β–eGFP and mCherry constructs were generated using a backbone encoding eGFP or mCherry under the human PGK promoter. SNAP–GSK3β was amplified and inserted into these plasmids using KpnI/EcoRI with the following primers: forward 5′-gatcggtaccgacaaagactgcg-3′ and reverse 5′-gatcgaattcactaccaccactaccac-3′. SNAP–MYC plasmid was generated from the SNAP–GSK3β plasmid using BamHI/NotI with the following *MYC* (Addgene, 101135) primers: forward 5′-gatcggatccatgcccctcaacgttagcttcac-3′ and reverse 5′-gatcgcggccgcttcgcacaagagttc-3′. Plasmids for CRISPR–Cas9 HITI encoded Halo–PRMT1 or Halo–PRMT1–T2A–SNAP–GSK3β–mCherry. By Gibson assembly, the Halo–PRMT1 gene was inserted into a parental HITI plasmid with the following primers: forward 5′-gaaacaggccggcgatgtggaggagaatcctggacctgcagaaatcggtactggctt-3′ and reverse 5′-aacttcgtagggtccgctgataaccgccgactattggtaatcagcgcatccggtagt-3′. By Gibson assembly, the T2A–SNAP–GSK3β–mCherry was then inserted with the following primers: forward 5′-ttctaacatgcggtgacgtggaggagaatcccggccctgacaaagactgcgaaatgaagc and reverse 5′-tggacgagctgtacaagtgattaccaatagtcggcggttatcagcggaccctacgaagtt-3′.

Immunoblotting

Cultured cells were lysed in 2x Laemmli sample buffer (4% SDS, 20% glycerol, 120 mM Tris–Cl (pH 6.8) and 0.02% bromophenol blue) with 10 mM fresh dithiothreitol (DTT). After a 10-min incubation at 95 °C, lysates were loaded on a 10% SDS–PAGE gel. Following separation, proteins

on the gel were transferred onto nitrocellulose membranes at 10 V for 75–130 min. Membranes were then blocked in milk and probed overnight with primary antibodies. The signal was detected using enhanced chemiluminescence (ECL) (Sigma-Aldrich, WBLUR0100) after a 1-h incubation in secondary antibody (mouse 1:10,000 (Invitrogen, 61-6520) or rabbit 1:20,000 (Prometheus, 20-303)). Images were acquired using the iBright FL750 imaging system. Bands were quantified using ImageJ software and normalized to the individual loading controls before normalization to the control sample. In some experiments, a treatment eliciting high ternary complex formation was quantified relative to the amount of ternary complex in a higher, degradative dose.

Immunofluorescence assays

Cells were plated and grown on glass coverslips. For HEK293/T cells, glass coverslips were coated in poly-l-lysine (Newcomer Supply, 1339A) before plating. Following the indicated treatments, cells were washed twice in PBS and fixed for 20 min in 4% paraformaldehyde (PFA). Fixed cells were washed 2x for 5 min in PBS, permeabilized in 0.2% Triton X-100 for 10 min, washed 2x for 5 min in PBS and blocked in 0.5% BSA before an overnight incubation in primary antibody. The following day, coverslips were washed 3x for 7 min in PBS, incubated in secondary antibody (1:2,000–5,000), washed 5x for 5 min in PBS and mounted with or without DAPI (Thermo Fisher Scientific, P36931 and P36930).

PLAs

The PLA of HEK293T cells was performed using the Sigma-Aldrich PLA Kit (DUO92004 and DUO92002) as per the manufacturer's instructions. In brief, HEK293T cells growing on poly-l-lysine-coated glass coverslips were treated with 10 μM HaXS8 for 60 min, fixed with 4% PFA and

prepared for staining with primary antibodies as described above. Anti-Flag, anti-LAMP-1 and anti-IgG were used at 1:300 dilutions, and anti-ADMA was used at 1:50 dilutions. Anti-IgG was used as a negative control. The next day, specimens were incubated with anti-mouse and anti-rabbit secondary antibodies conjugated to oligonucleotides. Close proximity of target antigens allows hybridization of the complementary secondary antibody nucleotide sequences. After a 30-min incubation at 37 °C with ligase and additional oligonucleotides, a closed DNA circle is formed. A subsequent step involving polymerase-driven rolling circle amplification incorporates fluorescently labeled nucleotides. Fluorescent nucleotides used in this experiment fluoresce in the red channel upon excitation. Protein–protein interactions between Flag–LAMP-1 or Flag–ADMA were visualized with confocal microscopy and quantified with ImageJ (National Institutes of Health (NIH), http://imagej.nih.gov/ij/). Data were normalized by applying the same brightness/contrast profile and threshold values. The ImageJ analyze particle feature was used to quantify PLA signals over 113–120 cells for each condition. Raw values for each paired experiment (Flag–LAMP-1 and Flag–ADMA) were then converted to fold change with respect to the appropriate control.

siRNA knockdown

HEK293T cells were seeded in six wells and transfected with 100 nM siRNA using Lipofectamine RNAiMax (Invitrogen, 13778100) according to the manufacturer's protocol. ON-TARGETplus SMARTpool siRNA targeting *LAMP2* (L-011715-00-0005), *ATG7* (L-020112-00-0005) or *VPS4A* (L-013092-00-0005) were obtained from Dharmacon. After 24 h of siRNA treatment, cells were split into 12-well dishes. The following day (day 2 of siRNA knockdown), cells were transfected with PRMT1–Halo and GSK3β–SNAP for 24 h. On day 3 of siRNA knockdown, cells

were treated for 24 h with DMSO or 10 μM MrTAC^{HaXS8}. Lysates were collected for immunoblot analysis, and cells were processed for immunofluorescence assays as described above.

Co-immunoprecipitation

HEK293 cells stably expressing Halo–PRMT1–MYC were cultured in 10 cm dishes with DMSO or 1 μM MrTAC^{SAHA} for 2 h in the presence of 400 nM bafilomycin and 10 μM MG132. Cells were lysed by scraping in lysis buffer (50 mM Tris (pH 7.9), 150 mM NaCl, 1 mM ethylene glycol-bis(β-aminoethyl ether)-*N*,*N*,*N*′,*N*′-tetraacetic acid (EGTA), 1 mM EDTA, 1 mM DTT, 10 μM leupeptin, 100 μM 4-(2-aminoethyl) benzenesulfonyl fluoride (AEBSF) and 2 mM phenylmethylsulfonyl fluoride (PMSF)) and clarified by centrifugation at 16,000*g* for 5 min at 4 °C. Clarified lysates were incubated with anti-MYC magnetic beads (Thermo Fisher Scientific, 88842; equilibrated with 3x 10 vol/vol TBS washes) for 3 h on a rotator at 4 °C. Following incubation, beads were washed twice with TBS and eluted in 4x Laemmli buffer followed by incubation at 95 °C for 20 min. Lysates and immunoprecipitated samples were analyzed by immunoblot as described above.

MrTAC treatment and proliferation assays

For dose curve and rescue experiments, variable doses of HaXS8 (MrTAC) were added to cell culture media to a final concentration of 0.1% DMSO (vol/vol). Cells were treated 1 day after transfection. The following compounds were used at the indicated concentrations and pretreatments with a final concentration of 0.1% DMSO (vol/vol): bafilomycin (100–400 nM; Cayman Chemical, 11038), bortezomib (50 nM; AvaChem Scientific, 2164), MG132 (5–10 μM; AdooQ Bioscience, A11043), GSK3368715 (10 μM, 24 h pretreatment; MedChemExpress, HY-

128717A), SAHA chloroalkane T1 (GLPBio, GC34772) and SAHA (Thomas Scientific, C835T10).

For stably integrated GSK3β proliferation experiments, HEK293 cells stably expressing PRMT1–Halo with SNAP–GSK3β–mCherry were seeded at 50,000 cells per well in 12 wells and treated with DMSO or 0.5 μM MrTAC^{HaXS8} on days 0, 1, 2 and 3. Live cells were counted on days 3 and 6 using a Trypan Blue stain with a Countess 2 Automated Cell Counter. At indicated time points, cells were lysed in 2x Laemmli buffer for immunoblot analysis.

For transient GSK3β and MYC proliferation experiments, HeLa cells were transfected in 10 cm dishes overnight and were subsequently plated in 12 wells with 50,000 cells per well. Treatment with DMSO or 0.5 μM HaXS8 began on the same day of plating (day 0). Live cells were counted on days 1, 3, 5 and 7 using a Trypan Blue stain with a Countess 2 Automated Cell Counter. At indicated time points, cells were lysed in 2x Laemmli, processed for qPCR or stained with crystal violet. For crystal violet staining, cells were grown on coverslips, fixed in 4% PFA for 20 min, washed twice with PBS and stained with 50 μg ml^{-1} crystal violet for 30 min before imaging.

For proliferation assays of endogenous BRD4, PRMT1–Halo stable HEK293 cells were seeded onto 12-well dishes at 50,000 cells per well. The following day, cells were treated in triplicate with 1 μM of MrTAC^{JQ1} or JQ1-PEG2-NH control. Cells were refreshed with media and drug treatments every day. After 5 days, wells were counted as described above. The fold changes in cell number were calculated based on the seeding density, followed by normalization against the control, where the control was always set as 1.

For the cell survival assay, PRMT1–Halo stable HEK293 cells and nontransfected HEK293 cells were seeded onto 96-well dishes at 25,000 cells per well. The following day, cells were treated with a $MrTAC^{SAHA}$ dose curve (100, 50, 10, 1, 0.5, 0.1 and 0 μM) for 72 h. Cell survival was measured using a Cell Counting Kit-8 (CCK-8; Dojindo, CK04) according to the manufacturer's instructions after a 2-h incubation with the CCK-8 reagent.

Quantitative PCR

For experiments involving gene expression analysis by quantitative PCR (qPCR), cells were plated at 50,000 cells per well in 12-well plates in complete DMEM. Cells were treated with $MrTAC^{JQ1}$ or DMSO and lysed at indicated time points. Then, RNA was isolated using the Direct-zol RNA Miniprep Kit (Zymo Research, R2050). cDNA was synthesized using 500 ng RNA per reaction using the High Capacity RNA-to-cDNA Kit (Invitrogen, 4387406). qPCR was performed using a Roche LightCycler480 and PowerUp SYBR Green qPCR Master Mix (Applied Biosystems, A25742). In total, 0.5 μg ml^{-1} primers were used for each reaction as follows: human *RPL13A* forward 5′-AAAAAGCGGATGGTGGTTC-3′ and reverse 5′-CGGTAGTGGATCTTGGCTTT-3′; *MYC*, forward 5′-CTGGTGCTCCATGAGGAGA-3′ and reverse 5′-CTCTGACCTTTTGCCAGGAG-3′; *CDKN1A*, forward 5′-TCACTGTCTTGTACCCTTGTGC-3′ and reverse 5′-GGCGTTTGGAGTGGTAGAAA-3′; *BCL2*, forward 5′-CGCTATGTCACCTCCTGTTTGC-3′ and reverse 5′-ACTCTGAGGACGAGAAGCCCTT-3′; *BIRC3*, forward 5′-GCTTTTGCTGTGATGGTGGACTC-3′ and reverse 5′-CTTGACGGATGAACTCCTGTCC-3′; *BIRC5*, forward 5′-CCACTGAGAACGAGCCAGACTT-3′ and reverse 5′-GTATTACAGGCGTAAGCCACCG-3′.

Each biological replicate was plated in technical triplicate. Fold change related to the control group was calculated using the 2ΔΔCP method with *RPL13A* as the reference gene.

Consurf modeling of GSK3β

Sequence-based GSK3β conservation was modeled using Consurf software (https://consurf.tau.ac.il/consurf_index.php). Briefly, the human GSK3β protein (UniProt ID: P49841) was aligned against 150 sequences using the HHMER search algorithm and the UniREF-90 protein database. The following settings were used: 1 iteration, *E* value cutoff = 0.0001, 95% maximal identity between sequences, 35% minimal identity for homologs, MAFFT-L-INS-i alignment, Bayesian calculation method and Best Model evolutionary substitution model.

In vitro methylation and MS

In vitro, 1 µg His–GSK3β–GST (Cayman Chemical, 33738) and 200 µM SAM (Sigma-Aldrich, A4377) were incubated in the presence or absence of 1 µg GST-PRMT1 (Cayman Chemical, 10350) in 50 µl reaction buffer (50 mM Tris–HCl (pH 8.0), 20 mM KCI, 5 mM DTT and 4 mM EDTA), and incubated at 37 °C for 1 h. The reaction was reduced with DTT (10 mM, 80 °C, 20 min) and alkylated (30 mM iodoacetamide, room temperature, dark, 1 h) before digestion with sequencing grade trypsin (Promega; 1/50 (wt/wt), 37 °C, 18 h). Samples were analyzed by LC–MS using an ACQUITY UPC H-class LC coupled to a Xevo Q-ToF (Waters). Observed *m*/*z* were mapped to an in silico digestion of GSK3β using Biopharmalynx (Waters, v 1.3.5; 30 ppm, fixed carbamidomethyl Cys, variable oxidation of Met, variable Arg methylation). In silico digestion of PRMT1 was also used to exclude PRMT1 peptides in analysis. Peptides were injected onto a reverse phase C4 column (ACQUITY UPLC Protein BEH C4 Column, 300 Å, 1.7 µm, 2.1 mm

x 50 mm; Waters) in a buffer stream of 3% ACN in 0.1% formic acid (0.3 ml min^{-1}) and desalted for 0.5 min before gradient elution from 3% to 60% acetonitrile (ACN) over 1.5 min. The Xevo Z-spray source was operated with a capillary voltage of 3,000 V and a cone voltage of 40 V (NaCsi calibration, Leu749 enkephalin lock mass). Nitrogen was used as the desolvation gas at 350 °C and a total flow of 800 l h^{-1}.

Immunoprecipitation and MS

HEK293 cells cultured in 10 cm dishes were transiently transfected with SNAP–GSK3β–FlagG and PRMT1–Halo for 24 h before treatment with 10 μM $MrTAC^{HaXS8}$ for 2 h in the presence of 400 nM bafilomycin and 10 μM MG132. Cells were lysed by scraping in lysis buffer (50 mM Tris (pH 7.9), 150 mM NaCl, 1 mM EGTA, 1 mM EDTA, 1 mM DTT, 10 μM leupeptin, 100 μM AEBSF and 2 mM PMSF) and clarified by centrifugation at 16,000*g* for 5 min at 4 °C. Clarified lysates were incubated with anti-Flag M2 magnetic beads (Sigma-Aldrich, M8823; equilibrated with 3× 10 vol/vol TBS washes) for 3 h on a rotator at 4 °C. Following incubation, beads were washed three times with TBS and eluted in 1% formic acid. Immunoprecipitated samples were loaded for LC–MS analysis as described above.

Untargeted proteomics by MS

HEK293 cells stably expressing PRMT1–Halo were cultured in six-well plates with either DMSO or $MrTAC^{SAHA}$ (1 μM, 4 h) before lysis by scraping in lysis buffer (50 mM Tris (pH 7.9), 150 mM NaCl, 1 mM EGTA, 1 mM EDTA, 1 mM DTT, 10 μM leupeptin, 100 μM AEBSF and 2 mM PMSF). Lysates were clarified by centrifugation at 16,000*g* for 10 min and snap-frozen in liquid nitrogen before processing. Samples were reduced with 10 mM DTT for 30 min at room

temperature. Next, samples were alkylated with 30 mM iodoacetamide for 30 min at room temperature in the dark. Samples were pelleted for 30 min at maximum speed at 4 °C and resuspended in ice-cold methanol for two washes and left to air dry. Once dried, samples were digested in 1% LysC in 8 M urea for 4 h at 37 °C followed by digestion with 2% trypsin in 1.5 M urea overnight at 37 °C. The following day, samples were acidified in 1% trifluoroacetic acid, desalted using Sep-Pak C18 cartridges (Waters, 186000308) and eluted in 50% acetonitrile. Digested peptides were separated and analyzed by liquid chromatography tandem mass spectrometry (LC–MS/MS) using an UltiMate 3000 RSLC liquid chromatograph (Thermo Fisher Scientific) coupled with in-line to a Thermo Fusion Lumos mass spectrometer (Thermo Fisher Scientific). Peptides were separated by reversed-phase chromatography on a Thermo Pepmap Acclaim column (50 cm x 75 μm) over a 90 min submission comprising a 60 min gradient from 4% to 22% mobile buffer B (mobile buffer A: H2O and 0.1% formic acid; mobile buffer B: ACN and 0.1% formic acid). For MS/MS analysis of peptides, each duty consisted of one FTMS scan (375–1,800 *m*/*z*, resolution of 120,000) followed by data-dependent MS/MS scans acquired in the ion trap with higher-collisional dissociation (normalized energy 30%) for 3 s at top speed in rapid mode. MS/MS data were subjected to database searching using MaxQuant (2.0.3.0) against a database obtained from SwissProt (2024.01.12) containing 20,428 human protein entries. The mass tolerances for parent ions and fragment ions were set as default, trypsin/P was set as the enzyme with two maximum missed cleavages allowed and protein N-terminal acetylation and methionine oxidation were selected as variable modifications. Cysteine carbamidomethylation was specified as a fixed modification. Peptide-spectrum match (PSM) false discovery rate (FDR), protein FDR and site decoy fraction were all reported at 0.01. Protein abundances for each sample

were measured using iBAQ, and following export, they were normalized across samples by total ion current before data analysis.

Statistical analyses

All experiments were repeated independently three times unless otherwise specified. All stated values represent the mean ± s.e.m., and values ±2x s.d. were excluded as outliers. The sample size is described in the figure captions for Figures 1–6 and Figures S1-6. Sample size n refers to independent biological experiments unless otherwise specified. GraphPad Prism 10 software was used for statistical analyses. A two-sided, unpaired Student's t-test was used to compare variables between two groups (degrees of freedom = $n_1 + n_2 - 2$). One-way analysis of variance (ANOVA) was used to compare variables between more than two groups (degrees of freedom = $n - 1$). Two-way ANOVA was used for multiday, multidose experiments testing multiple variables. Dose curve regressions were performed as described in Fig. 1 and Extended Data Fig. 1, where DC_{50} values were calculated. $*P < 0.05$, $**P < 0.01$, $***P < 0.001$ and $****P < 0.0001$ were considered to be statistically significant. Image quantification was performed as described previously (Albrecht et al., 2018; Franco et al., 2023). For microscopy experiments, samples were analyzed across indicated cell counts/fields of view in one biological replicate unless otherwise specified. Exact methods for quantification and full results of statistical tests are provided in the source data.

1.6 Data Availability

All data reporting the findings of this study are included in the Article and within the source data found in the Supplementary Information. Proteomics data have been submitted to the

ProteomeXchange Consortium in the PRIDE partner repository with the dataset identifier PXD054653. Source data are provided online at https://doi.org/10.1038/s41589-024-01741-y.

1.7 Acknowledgements

We thank members of the Albrecht Lab for their support in this research and thank J. Leonard for assistance in modeling and conceptualization. The research was supported in part by Ono Pharmaceuticals (award to L.V.A.) and we thank the Cystinosis Research Foundation (CRF) for funding. We would like to thank the UCI Mass Spectrometry Facility and B. Katz for assistance with the collection and analysis of protein MS data. Data were collected on a Waters Acquity UPLC Xevo G2-XS QTOF system (NIH supplemental funding support received by J.S. Nowick (National Institute of General Medical Sciences (NIGMS) GM097562), V.Y. Duong (NIH GM105938) and O. Cinquin (NIGMS GM102635)). We would like to thank C. Yu and L. Huang at the UCI High-end Mass Spectrometry Facility for their help and service in MS data acquisition and analysis. We would also like to thank the Comprehensive Liver Research Center at University of California, Los Angeles (UCLA).

1.8 Competing Interest Statement

The authors declare no competing interests.

1.9 Author Contributions

L.V.A., L.J.S. and C.N.F conceived the study. L.V.A. and L.J.S. designed the experiments. L.J.S., C.N.F., M.C., S.T.N., R.L.W., M.F.K. and K.S. contributed to cell biology experiments. C.A.L.,

J.O., S.R.L. and D.J.T. contributed to compound synthesis. C.F. and J.Z. contributed to CRISPR cell line construction. L.V.A. and L.J.S. analyzed the data. L.V.A. and L.J.S. wrote the manuscript.

1.10 References

Balch, W. E., Morimoto, R. I., Dillin, A. & Kelly, J. W. Adapting proteostasis for disease intervention. *Science* 319, 916–919 (2008).

Li, K. & Crews, C. M. PROTACs: past, present and future. *Chem. Soc. Rev*. 51, 5214–5236 (2022).

Spradlin, J. N., Zhang, E. & Nomura, D. K. Reimagining druggability using chemoproteomic platforms. *Acc. Chem. Res.* 54, 1801–1813 (2021).

Békés, M., Langley, D. R. & Crews, C. M. PROTAC targeted protein degraders: the past is prologue. *Nat. Rev. Drug Discov*. 21, 181–200 (2022).

Liu, X. & Ciulli, A. Proximity-based modalities for biology and medicine. *ACS Cent. Sci.* 9, 1269–1284 (2023).

Sakamoto, K. M. et al. Protacs: chimeric molecules that target proteins to the Skp1–Cullin–F box complex for ubiquitination and degradation. *Proc. Natl Acad. Sci. USA* 98, 8554–8559 (2001).

Chirnomas, D., Hornberger, K. R. & Crews, C. M. Protein degraders enter the clinic—a new approach to cancer therapy. *Nat. Rev. Clin. Oncol.* 20, 265–278 (2023).

Schneider, M. et al. The PROTACtable genome. *Nat. Rev. Drug Discov.* 20, 789–797 (2021).

Weng, G. et al. PROTAC-DB 2.0: an updated database of PROTACs. *Nucleic Acids Res.* 51, D1367–D1372 (2023).

Bashore, C. et al. Targeted degradation via direct 26S proteasome recruitment. *Nat. Chem. Biol.* 19, 55–63 (2023).

Ali, E. M. H., Loy, C. A. & Trader, D. J. ByeTAC: bypassing an E3 ligase for targeted protein degradation. Preprint at bioRxiv https://doi.org/10.1101/2024.01.20.576376 (2024).

Takahashi, D. et al. AUTACs: cargo-specific degraders using selective autophagy. *Mol. Cell* 76, 797–810 (2019).

Ji, C. H. et al. The AUTOTAC chemical biology platform for targeted protein degradation via the autophagy-lysosome system. *Nat. Commun.* 13, 904 (2022).

Fu, Y. et al. Degradation of lipid droplets by chimeric autophagy-tethering compounds. *Cell Res.* 31, 965–979 (2021).

Li, Z. et al. Allele-selective lowering of mutant HTT protein by HTT–LC3 linker compounds. *Nature* 575, 203–209 (2019).

Ahn, G. et al. LYTACs that engage the asialoglycoprotein receptor for targeted protein degradation. *Nat. Chem. Biol.* 17, 937–946 (2021).

Banik, S. M. et al. Lysosome-targeting chimaeras for degradation of extracellular proteins. *Nature* 584, 291–297 (2020).

Ahn, G. et al. Elucidating the cellular determinants of targeted membrane protein degradation by lysosome-targeting chimeras. *Science* 382, eadf6249 (2023).

Zhou, Y., Teng, P., Montgomery, N. T., Li, X. & Tang, W. Development of triantennary N-acetylgalactosamine conjugates as degraders for extracellular proteins. *ACS Cent. Sci.* 7, 499–506 (2021).

Caianiello, D. F. et al. Bifunctional small molecules that mediate the degradation of extracellular proteins. *Nat. Chem. Biol.* 17, 947–953 (2021).

Wong, E. & Cuervo, A. M. Integration of clearance mechanisms: the proteasome and autophagy. *Cold Spring Harb. Perspect. Biol.* 2, a006734 (2010).

Varshavsky, A. N-degron and C-degron pathways of protein degradation. *Proc. Natl Acad. Sci. USA* 116, 358–366 (2019).

Poirson, J. et al. Proteome-scale discovery of protein degradation and stabilization effectors. *Nature* 628, 878–886 (2024).

Owens, D. D. G. et al. A chemical probe to modulate human GID4 pro/N-degron interactions. *Nat. Chem. Biol.* 20, 1164–1175 (2024).

Ichikawa, S. et al. The E3 ligase adapter cereblon targets the C-terminal cyclic imide degron. *Nature* 610, 775–782 (2022).

Makaros, Y. et al. Ubiquitin-independent proteasomal degradation driven by C-degron pathways. *Mol. Cell* 83, 1921–1935 (2023).

Lucas, X. & Ciulli, A. Recognition of substrate degrons by E3 ubiquitin ligases and modulation by small-molecule mimicry strategies. *Curr. Opin. Struct. Biol.* 44, 101–110 (2017).

Nabet, B. et al. The dTAG system for immediate and target specific protein degradation. *Nat. Chem. Biol.* 14, 431–441 (2018).

Albrecht, L. V., Ploper, D., Tejeda-Muñoz, N. & De Robertis, E. M. Arginine methylation is required for canonical Wnt signaling and endolysosomal trafficking. *Proc. Natl Acad. Sci. USA* 115, E5317–E5325 (2018).

Franco, C. N. et al. Vitamin B6 is governed by the local compartmentalization of metabolic enzymes during growth. *Sci. Adv.* 9, eadi2232 (2023).

Larsen, S. C. et al. Proteome-wide analysis of arginine monomethylation reveals widespread occurrence in human cells. *Sci. Signal.* 9, rs9 (2016).

Bedford, M. T. & Clarke, S. G. Protein arginine methylation in mammals: who, what, and why. *Mol. Cell* 33, 1–13 (2009).

Dotson, H. L. & Ngo, J. T. SNAP-tag and HaloTag fused proteins for HaSX8-inducible control over synthetic biological functions in engineered mammalian cells. Preprint at bioRxiv https://doi.org/10.1101/2022.08.12.503781 (2022).

Buckley, D. L. et al. HaloPROTACS: use of small molecule PROTACs to induce degradation of HaloTag fusion proteins. *ACS Chem. Biol.* 10, 1831–1837 (2015).

Erhart, D. et al. Chemical development of intracellular protein heterodimerizers. *Chem. Biol*. 20, 549–557 (2013).

Kaidanovich-Beilin, O. & Woodgett, J. R. GSK-3: functional insights from cell biology and animal models. *Front. Mol. Neurosci.* 4, 40 (2011).

Taelman, V. F. et al. Wnt signaling requires sequestration of glycogen synthase kinase 3 inside multivesicular endosomes. *Cell* 143, 1136–1148 (2010).

Douglass, E. F., Miller, C. J., Sparer, G., Shapiro, H. & Spiegel, D. A. A comprehensive mathematical model for three-body binding equilibria. *J. Am. Chem. Soc.* 135, 6092–6099 (2013).

Haid, R. T. U. & Reichel, A. A mechanistic pharmacodynamic modeling framework for the assessment and optimization of proteolysis targeting chimeras (PROTACs). *Pharmaceutics* 15, 195 (2023).

Weibrecht, I. et al. Proximity ligation assays: a recent addition to the proteomics toolbox. *Expert Rev. Proteomics* 7, 401–409 (2010).

Klionsky, D. J. et al. Guidelines for the use and interpretation of assays for monitoring autophagy (4th edition). *Autophagy* 17, 1–382 (2021).

Sahu, R. et al. Microautophagy of cytosolic proteins by late endosomes. *Dev. Cell* 20, 131–139 (2011).

Bishop, N. & Woodman, P. ATPase-defective mammalian VPS4 localizes to aberrant endosomes and impairs cholesterol trafficking. *Mol. Biol. Cell* 11, 227–239 (2000).

El-Khoueiry, A. B. et al. Phase 1 study of GSK3368715, a type I PRMT inhibitor, in patients with advanced solid tumors. *Br. J. Cancer* 129, 309–317 (2023).

Kim, E. et al. Protection of c-Fos from autophagic degradation by PRMT1-mediated methylation fosters gastric tumorigenesis. *Int. J. Biol. Sci.* 19, 3640–3660 (2023).

Hooper, C., Killick, R. & Lovestone, S. The GSK3 hypothesis of Alzheimer's disease. *J. Neurochem.* 104, 1433–1439 (2008).

Bilic, J. et al. Wnt induces LRP6 signalosomes and promotes dishevelled-dependent LRP6 phosphorylation. *Science* 316,1619–1622 (2007).

Clevers, H. & Nusse, R. Wnt/β-catenin signaling and disease. *Cell* 149, 1192–1205 (2012).

Kress, T. R., Sabò, A. & Amati, B. MYC: connecting selective transcriptional control to global RNA production. *Nat. Rev. Cancer* 15, 593–607 (2015).

Chen, H., Liu, H. & Qing, G. Targeting oncogenic Myc as a strategy for cancer treatment. *Signal Transduct. Target. Ther*. 3, 5 (2018).

Boike, L. et al. Discovery of a functional covalent ligand targeting an intrinsically disordered cysteine within MYC. *Cell Chem. Biol.* 28, 4–13 (2021).

Belkina, A. C. & Denis, G. V. BET domain co-regulators in obesity, inflammation and cancer. *Nat. Rev. Cancer* 12, 465–477 (2012).

Winter, G. E. et al. BET bromodomain proteins function as master transcription elongation factors independent of CDK9 recruitment. *Mol. Cell* 67, 5–18 (2017).

Young, P., Deveraux, Q., Beal, R. E., Pickart, C. M. & Rechsteiner, M. Characterization of two polyubiquitin binding sites in the 26S protease subunit 5a. *J. Biol. Chem*. 273, 5461–5467 (1998).

Hines, J., Lartigue, S., Dong, H., Qian, Y. & Crews, C. M. MDM2-recruiting PROTAC offers superior, synergistic anti-proliferative activity via simultaneous degradation of BRD4 and stabilization of p53. *Cancer Res*. 79, 251–262 (2019).

Zengerle, M., Chan, K.-H. & Ciulli, A. Selective small molecule induced degradation of the BET bromodomain protein BRD4. *ACS Chem. Biol.* 10, 1770–1777 (2015).

Simpson, L. M. et al. Inducible degradation of target proteins through a tractable affinity-directed protein missile system. *Cell Chem. Biol.* 27, 1164–1180 (2020).

Lee, Y.-S. et al. The cytoplasmic deacetylase HDAC6 is required for efficient oncogenic tumorigenesis. *Cancer Res*. 68, 7561–7569 (2008).

Haberland, M., Montgomery, R. L. & Olson, E. N. The many roles of histone deacetylases in development and physiology: implications for disease and therapy. *Nat. Rev. Genet.* 10, 32–42 (2009).

Bradner, J. E. et al. Chemical phylogenetics of histone deacetylases. *Nat. Chem. Biol.* 6, 238–243 (2010).

Hanswillemenke, A. et al. Profiling the interactome of oligonucleotide drugs by proximity biotinylation. *Nat. Chem. Biol.* 20, 555–565 (2024).

Ohana, R. F. et al. Deciphering the cellular targets of bioactive compounds using a chloroalkane capture tag. *ACS Chem. Biol.* 10, 2316–2324 (2015).

Hu, Y. et al. BRD4 inhibitor inhibits colorectal cancer growth and metastasis. *Int. J. Mol. Sci.* 16, 1928–1948 (2015).

Li, L. et al. Histone deacetylase inhibitor sodium butyrate suppresses DNA double strand break repair induced by etoposide more effectively in MCF-7 cells than in HEK293 cells. *BMC Biochem.* 16, 2 (2015).

Tran, A. D.-A. et al. HDAC6 deacetylation of tubulin modulates dynamics of cellular adhesions. *J. Cell Sci.* 120, 1469–1479 (2007).

Perera, R. M. & Zoncu, R. The lysosome as a regulatory hub. *Annu. Rev. Cell Dev. Biol.* 32, 223–253 (2016).

Miao, Y. et al. Bispecific aptamer chimeras enable targeted protein degradation on cell membranes. *Angew. Chem. Int. Ed.* 60, 11267–11271 (2021).

Cotton, A. D., Nguyen, D. P., Gramespacher, J. A., Seiple, I. B. & Wells, J. A. Development of antibody-based PROTACs for the degradation of the cell-surface immune checkpoint protein PD-L1. *J. Am. Chem. Soc.* 143, 593–598 (2021).

Hsia, O. et al. Targeted protein degradation via intramolecular bivalent glues. *Nature* 627, 204–211 (2024).

Bao, J. et al. Discovery of novel pdeδ autophagic degraders: a case study of autophagy-tethering compound (ATTEC). *ACS Med. Chem. Lett.* 15, 29–35 (2024).

Wang, L., Klionsky, D. J. & Shen, H.-M. The emerging mechanisms and functions of microautophagy. *Nat. Rev. Mol. Cell Biol.* 24, 186–203 (2023).

Nabet, B. et al. Rapid and direct control of target protein levels with VHL-recruiting dTAG molecules. *Nat. Commun.* 11, 4687 (2020).

Wang, W. W. et al. Targeted protein acetylation in cells using heterobifunctional molecules. *J. Am. Chem. Soc.* 143, 16700–16708 (2021).

Siriwardena, S. U. et al. Phosphorylation-inducing chimeric small molecules. *J. Am. Chem. Soc.* 142, 14052–14057 (2020).

Hines, J., Gough, J. D., Corson, T. W. & Crews, C. M. Posttranslational protein knockdown coupled to receptor tyrosine kinase activation with phosphoPROTACs. *Proc. Natl Acad. Sci.* USA 110, 8942–8947 (2013).

Wu, Q., Schapira, M., Arrowsmith, C. H. & Barsyte-Lovejoy, D. Protein arginine methylation: from enigmatic functions to therapeutic targeting. *Nat. Rev. Drug Discov.* 20, 509–530 (2021).

1.11 Figures

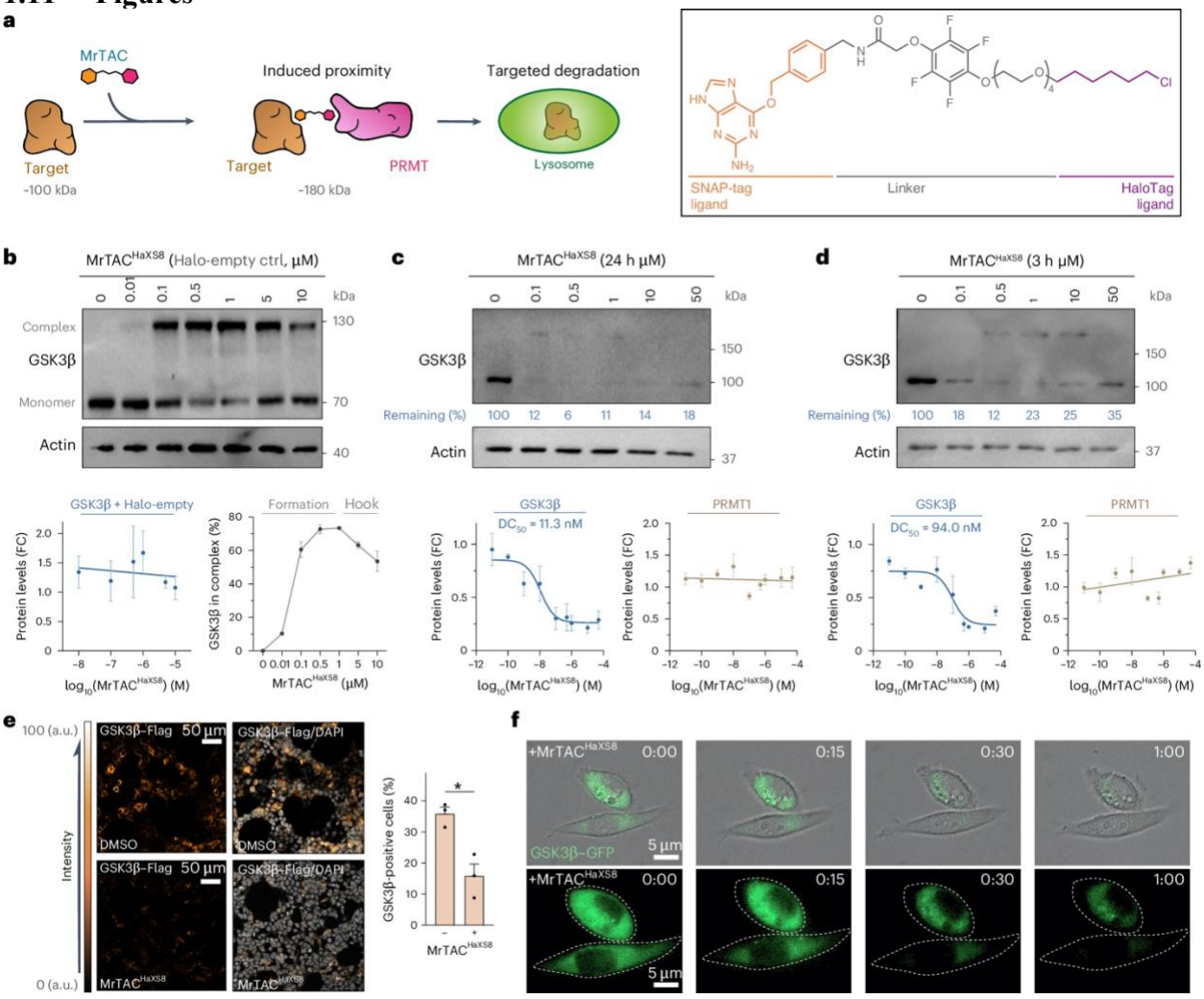

Figure 1.1 MrTAC mediates proximity with PRMT1 for target degradation.

(A) Left, scheme of MrTAC inducing proximity between a POI and PRMT1. Right, structure of MrTAC^{HaXS8}. **(B)** Top, immunoblot analysis of HEK293T cells co-expressing GSK3β–SNAP (70 kDa) and empty HaloTag control (30 kDa), in a 3-h MrTAC^{HaXS8} dose curve ($n = 3$). Bottom left, graph depicts fold change (FC) in GSK3β protein levels with linear regression analysis; bottom right, graph shows the fraction of GSK3β in the ternary complex (180 kDa) relative to the total amount of GSK3β. **(C)** Immunoblot analysis of HEK293 cells stably expressing PRMT1–Halo (70 kDa) and mCherry-tagged GSK3β–SNAP (100 kDa) in a 24-h MrTAC^{HaXS8} dose curve ($n = 3$). **(D)** Immunoblot analysis of HEK293 cells stably expressing PRMT1–Halo and mCherry-tagged GSK3β–SNAP in a 3-h MrTAC^{HaXS8} dose curve ($n = 3$). **(E)** Left, confocal microscopy of GSK3β–SNAP + HEK293T cells detected by Flag antibody following MrTAC^{HaXS8} treatment (10 μM, 3 h). Right, bars are fractions of GSK3β–SNAP-positive cells divided by total cells marked by 4',6-diamidino-2-phenylindole (DAPI) ($n = 513$ cells per condition over three fields of view). Unpaired two-sided *t*-test, $^*P < 0.0124$. Scale bar, 50 μm. **(F)** Live-cell imaging of green

fluorescent protein (GFP)-tagged GSK3β–SNAP during MrTAC treatment (0.1 μM, 1 h) in HeLa cells. Scale bar, 5 μm. For (C) and (D), the bottom left graphs depict total levels of GSK3β–SNAP, and the bottom right graphs depict total levels of PRMT1–Halo (normalized to protein levels in 0 μM conditions), DC_{50} values are by sigmoidal regression, and percentage remaining values are indicated for blots depicted. Immunoblots are representative of three independent experiments. Data are represented as mean ± s.e.m.

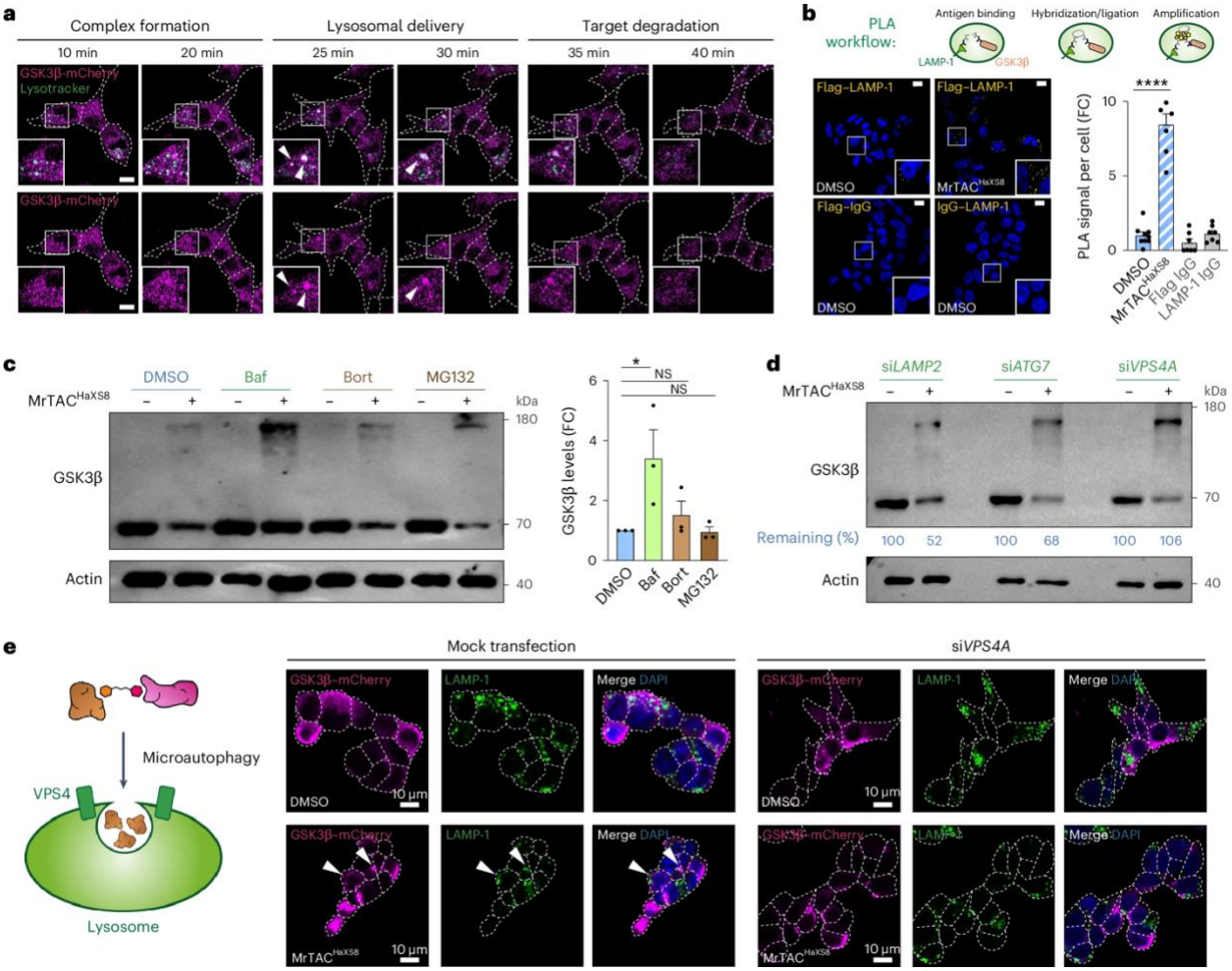

Figure 1.2 MrTAC targets GSK3β to lysosomes for degradation.

(A) Live-cell imaging of mCherry-tagged GSK3β–SNAP during MrTAC^{HaXS8} (0.5 μM, 40 min) treatment in stably expressing HEK293 cells. Lysosomes are stained with Lysotracker. Scale bars, 5 μm. Arrowheads mark colocalization. **(B)** Diagram (top) and microscopy (bottom) of PLA for GSK3β–SNAP delivery into lysosomes in MrTAC-treated cells (10 μM, 1 h). Flag antibody detects GSK3β, and LAMP-1 antibody recognizes a luminal LAMP-1 epitope. Scale bar, 10 μm. PLA of IgG–Flag and IgG–LAMP-1 control for nonspecific interactions. Right, bars are the number of PLA puncta/cell per field of view ($n = 114$ DMSO, $n = 110$ MrTAC, $n = 111$ Flag and $n = 113$ LAMP-1 cells). Unpaired two-sided *t*-test, $****P < 0.0001$. **(C)** Left, immunoblot analysis of GSK3β–SNAP levels in MrTAC-treated cells (10 μM, 24 h) in the presence of bafilomycin (Baf, 100 nM), bortezomib (Bort, 50 nM) or MG132 (5 μM; $n = 3$). Right, bars quantify GSK3β ternary complex levels with either inhibitor relative to no inhibitor (ternary complex levels first calculated by fold change to total GSK3β in MrTAC-treated condition to account for off-target inhibitor effects). One-way ANOVA with Dunnett's multiple comparisons, $*P < 0.0335$ ($*P < 0.0382$ drug effect). **(D)** Immunoblot analysis of MrTAC^{HaXS8} degradation in HEK293T cells

transiently expressing PRMT1–Halo/GSK3β–SNAP with siRNA against *VPS4A*, *LAMP2* or *ATG7* (10 μM, 24 h; $n = 3$). **(E)** Left, model of microautophagy of MrTAC complex via VPS4. Right, immunofluorescent analysis of MrTAC degradation of GSK3β–SNAP in control or si*VPS4A* HEK293T cells with a LAMP-1 co-stain (10 μM, 2 h). Scale bars, 10 μm. Immunoblots are representative of three independent experiments. Data are represented as mean ± s.e.m. NS, not significant.

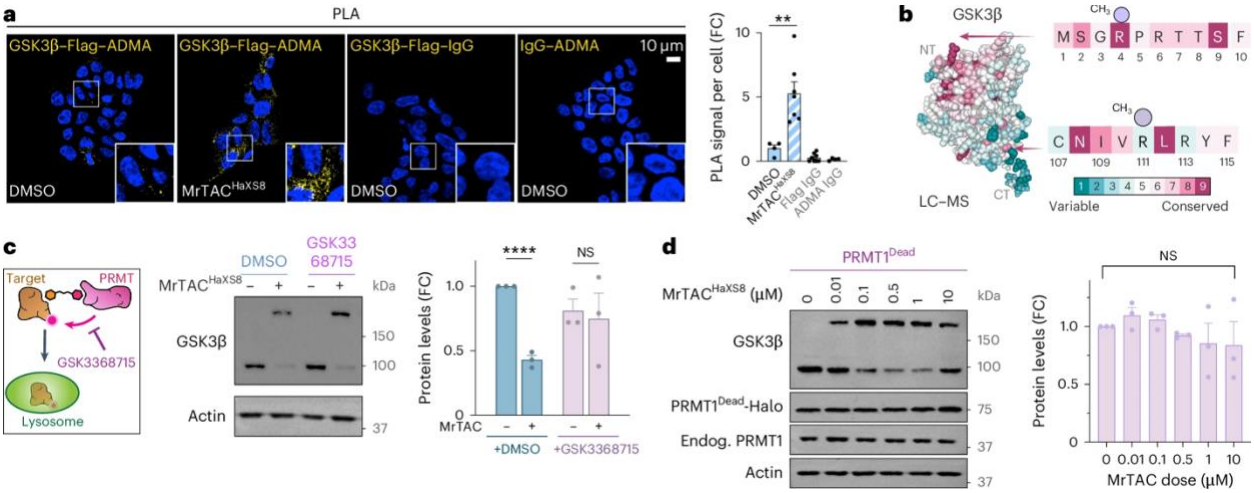

Figure 1.3 Arginine methylation of the protein target underscores MrTAC degradation.

(A) Left, PLA detection of GSK3β–SNAP methylation in MrTAC^{HaXS8}-treated HEK293T cells (10 μM, 1 h). Flag antibody detects GSK3β–SNAP, and ADMA antibody detects methylation. PLA of IgG–Flag and IgG–ADMA control for nonspecific interactions. Scale bar, 10 μm. Right, bars show the average number of PLA puncta per cell marked by DAPI across each field of view ($n = 120$ DMSO, $n = 113$ MrTAC, $n = 120$ Flag and $n = 116$ ADMA cells). Unpaired two-sided *t*-test, $^{**}P < 0.0069$. **(B)** Conservation of GSK3β by Consurf. Arrows denote R4 and R111. CT, C terminus; NT, N terminus. **(C)** Left, immunoblot analysis of GSK3β–SNAP in MrTAC-treated cells (10 μM, 3 h) in the presence of GSK3368715 (10 μM; $n = 3$). Right, total levels of GSK3β normalized to the DMSO condition. Unpaired two-sided *t*-test, $^{****}P < 0.0001$. **(D)** Left, immunoblot analysis of GSK3β–SNAP over a 24-h MrTAC dose curve in HEK293 cells stably expressing catalytically dead PRMT1–Halo (VLD to AAA) with an mCherry-tagged GSK3β–SNAP ($n = 3$). Right, bars show total levels of GSK3β as normalized to 0 μM condition. NS, not significant by one-way ANOVA with Dunnett's multiple comparisons. Immunoblots are representative of three independent experiments. Data are represented as mean ± s.e.m.

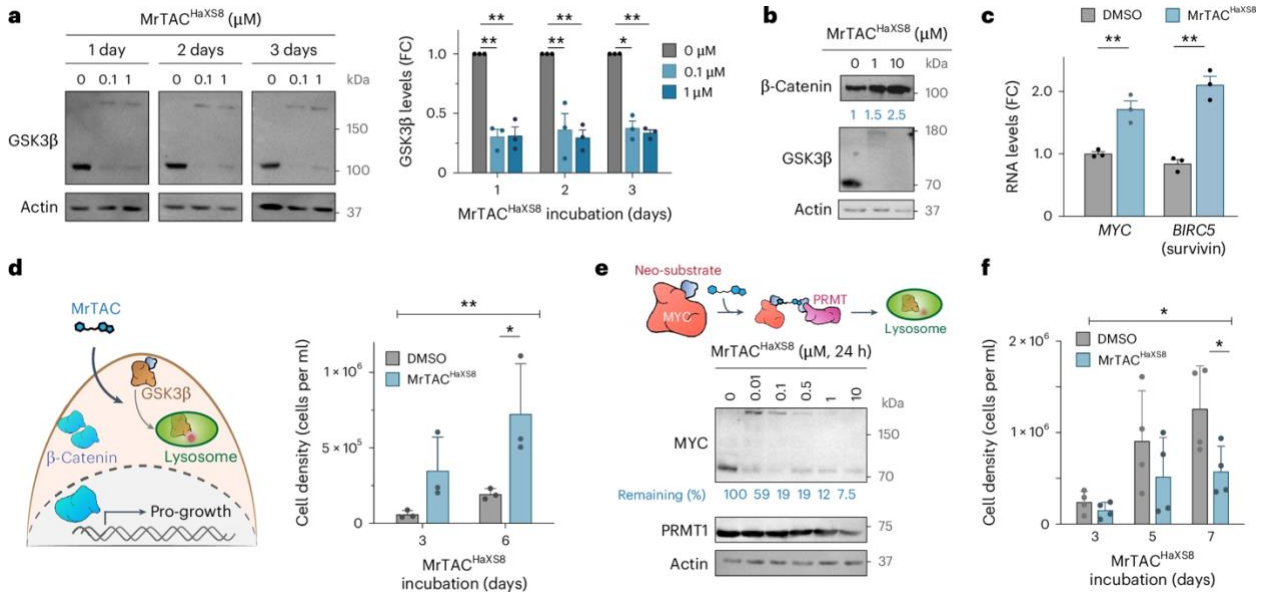

Figure 1.4 MrTAC degradation recapitulates loss-of-function phenotypes.

(A) Left, immunoblot analysis of GSK3β levels over a 3-day MrTAC treatment in HEK293 cells stably expressing PRMT1–Halo with an mCherry-tagged GSK3β–SNAP ($n = 3$). Right, total levels of GSK3β as normalized to 0 μM condition. Two-way ANOVA with Dunnett's multiple comparisons, $^{**}P_{\text{day 1:0.1 μM}} < 0.0042$, $^{**}P_{\text{D1:1}} < 0.0045$, $^{**}P_{\text{D2:0.1}} < 0.0086$, $^{**}P_{\text{D2:1}} < 0.0038$, $^{*}P_{\text{D3:0.1}} < 0.0103$ and $^{**}P_{\text{D3:1}} < 0.0061$. **(B)** Immunoblot analysis of β-catenin and GSK3β–SNAP in MrTAC-treated HEK293T cells (1 and 10 μM, 4 days; $n = 2$). **(C)** mRNA levels of *MYC* and *BIRC5* following treatment with DMSO or MrTAC^{HaXS8} (0.5 μM, 7 days; $n = 3$ experiments) in cells expressing CRISPR-integrated PRMT1–Halo with GSK3β–SNAP. $^{**}P_{BIRC5} < 0.0012$, $^{**}P_{MYC} < 0.0059$ by unpaired two-sided *t*-test. **(D)** Left, diagram of downstream consequences of GSK3β degradation. Right, proliferation (total number of cells per well) following MrTAC treatment (0.5 μM) in HEK293 cells expressing CRISPR-integrated PRMT1–Halo with GSK3β–SNAP over 3 and 6 days ($n = 3$ experiments). Two-way ANOVA with Bonferroni's multiple comparisons, $^{**}P < 0.0079$ drug effect and $^{*}P_{\text{D6}} < 0.0245$. **(E)** Immunoblot analysis of MYC–SNAP levels in MrTAC^{HaXS8}-treated HEK293 cells (24 h) expressing PRMT1–Halo ($n = 3$). **(F)** Proliferation (total number of cells per well) of MrTAC^{HaXS8}-treated HeLa cells expressing PRMT1–Halo with MYC–SNAP over 7 days (0.5 μM, $n = 4$ experiments). Two-way ANOVA with Bonferroni's multiple comparisons, $^{*}P < 0.0182$ drug effect and $^{*}P_{\text{D7}} < 0.0490$ at day 7. Immunoblots are representative of at least two independent experiments. Data are represented as mean ± s.e.m.

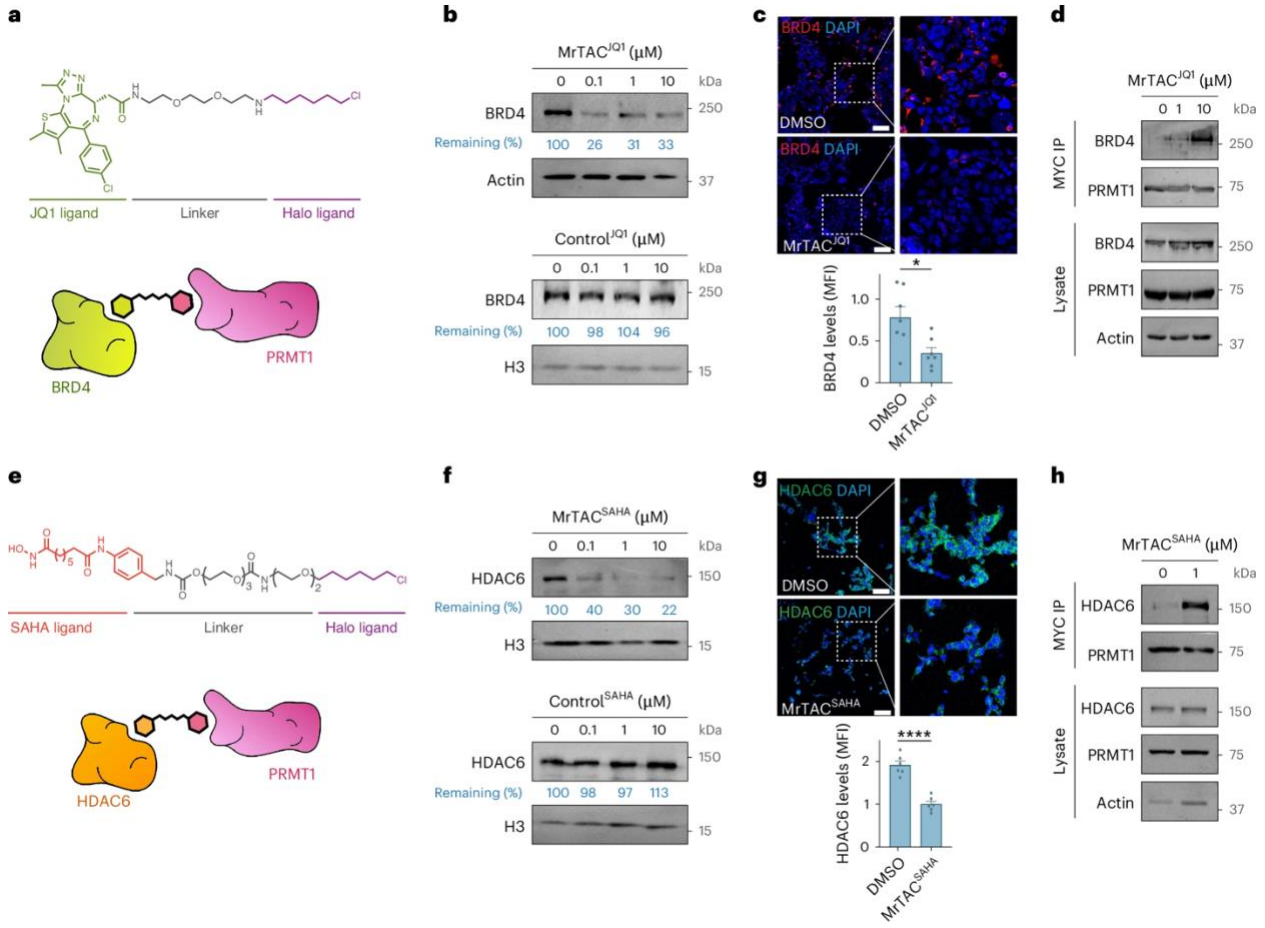

Figure 1.5 Induced degradation of endogenous substrates.

(A) Structure of MrTAC^{JQ1} (top), and schematic representation of MrTAC^{JQ1} recruiting PRMT1–Halo to endogenous BRD4 (bottom). **(B)** Immunoblot analysis of BRD4 levels following treatment with MrTAC^{JQ1} (top) or control^{JQ1} (JQ1-PEG2-NH; bottom) over 4 h ($n = 3$). **(C)** Top, immunofluorescence staining of BRD4 levels following MrTAC^{JQ1} treatment (0.5 μM, 4 h). Bottom, quantification of BRD4 intensity across total cells (marked by DAPI). *$P < 0.0139$ by unpaired two-sided *t*-test ($n = 7$ fields of view). **(D)** Co-immunoprecipitation (IP) of BRD4 by MYC pull-down of PRMT1–Halo–MYC after MrTAC^{JQ1} treatment (2 h) cotreated with bafilomycin (400 nM) and MG132 (10 μM). **(E)** Structure of MrTAC^{SAHA} (top), and schematic of MrTAC^{SAHA} recruiting PRMT1–Halo to endogenous HDAC6 (bottom). **(F)** Immunoblot analysis of HDAC6 following treatment with MrTAC^{SAHA} (top) or control^{SAHA} ligand (bottom) over 4 h ($n = 4$ MrTAC^{SAHA} and $n = 3$ control^{SAHA}). **(G)** Top, immunofluorescence staining of HDAC6 following MrTAC^{SAHA} treatment (4 h, 0.5 μM). Bottom, quantification of HDAC6 intensity across total cells (marked by DAPI). Unpaired two-sided *t*-test, ****$P < 0.0001$ ($n = 6$ fields of view). **(H)** Co-immunoprecipitation of HDAC6 by MYC pull-down of PRMT1–Halo–MYC following MrTAC^{SAHA} treatment (2 h) cotreated with bafilomycin (400 nM) and

MG132 (10 μM; $n = 3$ experiments). Assays performed in HEK293 cells stably expressing PRMT1–Halo–MYC. Immunoblots are representative of at least three independent experiments. Data are represented as mean ± s.e.m. Scale bar, 100 μm. MFI, mean fluorescence intensity.

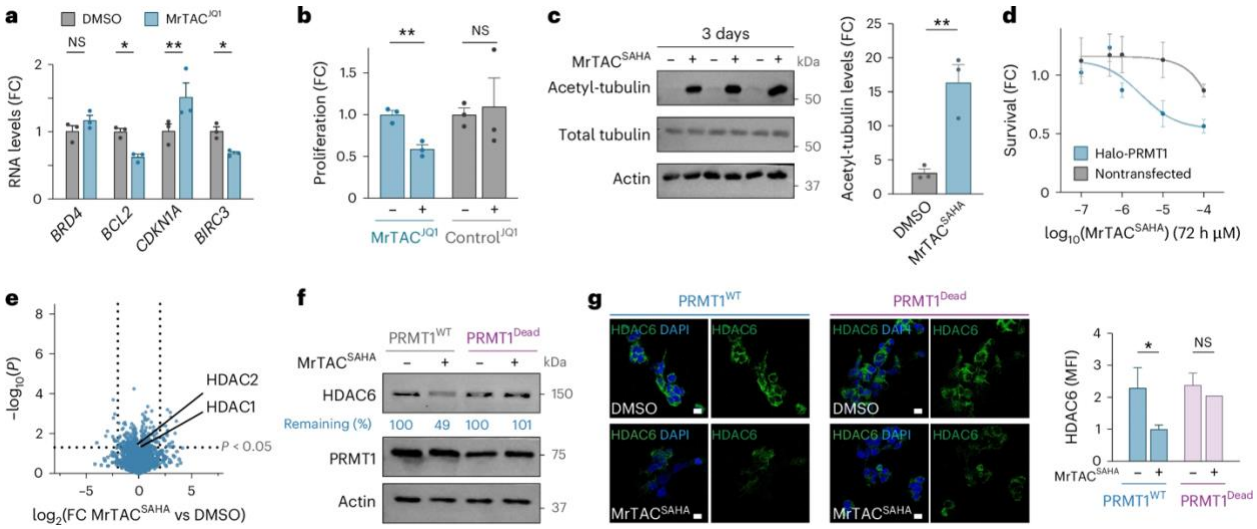

Figure 1.6 MrTAC regulates cell function via endogenous degradation.

(A) mRNA levels of *BRD4, BCL2, CDKN1A* and *BIRC3* in cells treated with DMSO or MrTAC (1 μM, 24 h; $n = 3$). Two-way ANOVA with Bonferroni's multiple comparisons, $*P_{BCL2} < 0.0155$, $**P_{CDKN1A} < 0.0023$ and $*P_{BIRC3} < 0.0319$. **(B)** Cell proliferation after 6 days of MrTAC^{JQ1} or control^{JQ1} treatment relative to DMSO (1 μM, $n = 3$ experiments). Unpaired two-sided *t*-test, $**P < 0.0051$. **(C)** Left, immunoblot of K40-acetylated α-tubulin following 3 days of MrTAC^{SAHA} treatment relative to total α-tubulin ($n = 3$). Right, quantification of acetyl-tubulin levels. Unpaired two-sided *t*-test, $**P < 0.0081$. **(D)** Cell survival over a 3-day treatment of MrTAC^{SAHA} in HEK293 cells stably expressing PRMT1–Halo with a non-transfected control by cell counting kit-8 (CCK-8) assay ($n = 6$ technical replicates). **(E)** Untargeted proteomic analysis of cells treated with MrTAC^{SAHA} or DMSO (1 μM, 4 h). *P* values by unpaired two-sided *t*-test ($n = 6$ technical replicates). **(F)** Immunoblot analysis of HDAC6 levels in MrTAC^{SAHA}-treated HEK293 cells (1 μM, 4 h) stably expressing wild-type or catalytically dead (VLD to AAA) PRMT1–Halo ($n = 3$). **(G)** Left, immunofluorescence staining of HDAC6 levels following MrTAC^{SAHA} treatment in HEK293 cells stably expressing wild-type or catalytically dead PRMT1 (0.5 μM, 4 h). Right, quantification of HDAC6 intensity across total cells (marked by DAPI). One-way ANOVA with Bonferroni's multiple comparisons, $*P < 0.0477$ ($n_{WT} = 2$ experiments with 80_{DMSO} and 79_{MrTAC} pooled cells; $n_{Dead} = 3$ experiments over 98_{DMSO} and 89_{MrTAC} pooled cells). Scale bars, 20 μm. Assays performed in HEK293 cells stably expressing PRMT1–Halo–MYC unless otherwise specified. Immunoblots are representative of three independent experiments. Data are represented as mean ± s.e.m.

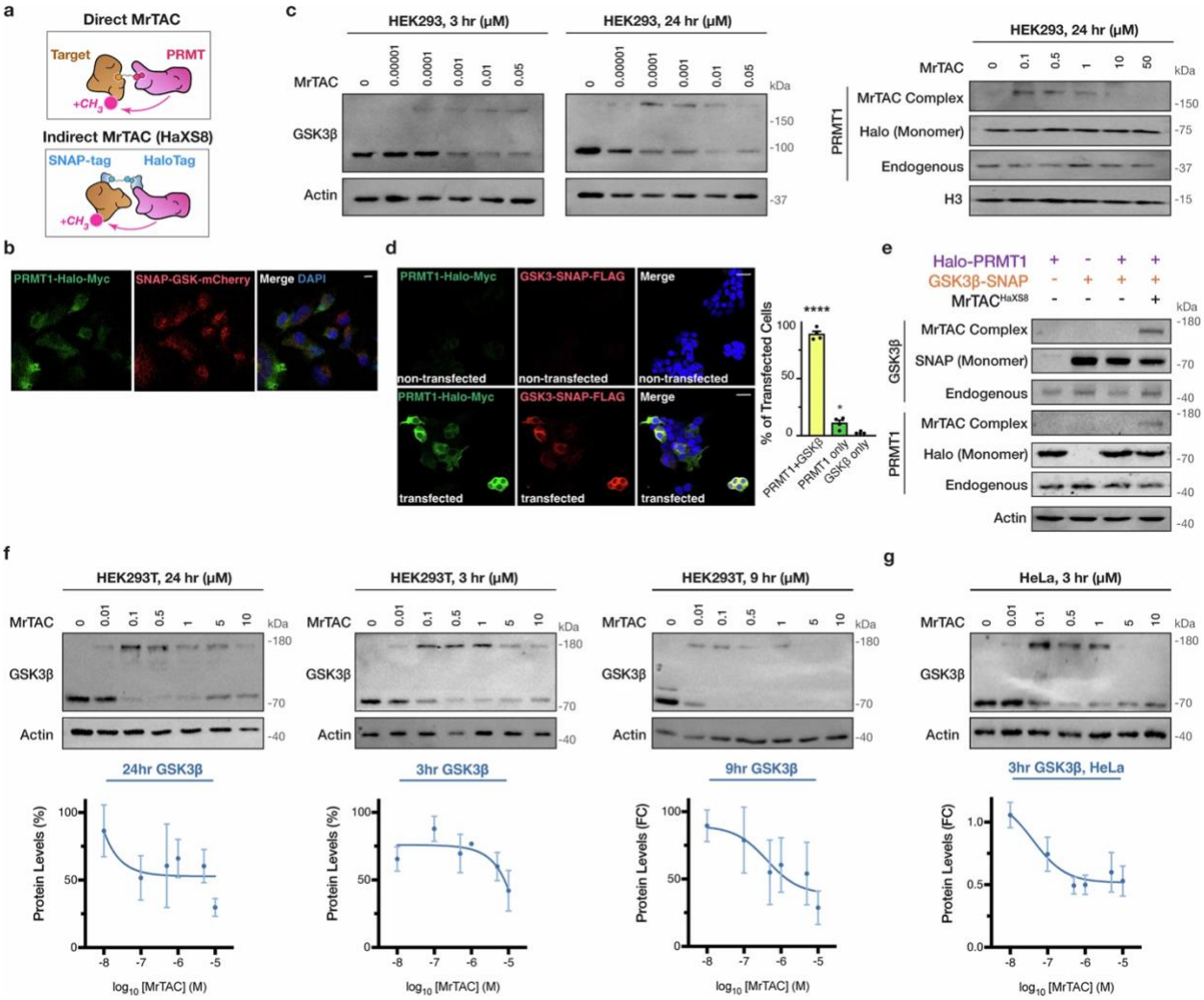

Figure 1.7 Expression and degradation of GSK3β by MrTAC.

(A) Schematic of types of MrTAC compounds to mediate proximity between a protein target and a protein arginine methyltransferase (PRMT). Indirect MrTAC dimerizes HaloTag and SNAP-tag fusion proteins that are encoded alongside the PRMT and target. **(B)** Representative immunofluorescence of HEK293 cells stably expressing GSK3β-SNAP-mCherry-FLAG (red) and Halo-PRMT1-Myc (green). **(C)** Immunoblot analysis of GSK3β levels (left) and PRMT1 levels (endogenous, Halo-tagged monomer and Halo-tagged in MrTAC complex; right) during either a 24- or 3-h MrTAC^{HaXS8} dose curve in stably expressing HEK293s. **(D)** Confocal microscopy of HEK293T cells either non-transfected or transfected with GSK3β-SNAP-FLAG (red) and Halo-PRMT1-Myc (green; left). Quantification (right) shows proportion of cells expressing both constructs or just one construct relative to the total number of transfected cells over three fields of view. ****$P < 0.0001$, *$P < 0.0217$ by one-sided t-test relative to 0% ($n = 3$ fields of view). **(E)** Immunoblot analysis of endogenous GSK3β and PRMT1, overexpressed GSK3β-SNAP and Halo-PRMT1 and GSK3β-MrTAC-PRMT1 complexes (0.5 μM, 1 h). **(F)** Immunoblot analysis of HEK293T cells

transiently expressing Halo-PRMT1 and GSK3β-SNAP in a 24 (left), 3 (middle) or 9-h (right) MrTAC dose curve (top). Bottom graphs show total levels of GSK3β relative to 0 μM. **(G)** Immunoblot analysis of HeLa cells expressing Halo-PRMT1 and GSK3β-SNAP in a 3-h MrTAC dose curve (top). Bottom graph shows total levels of GSK3β relative to 0 μM. Scale bars are 10 μm. Immunoblots are representative of three independent experiments. Data are represented as means ± SEM.

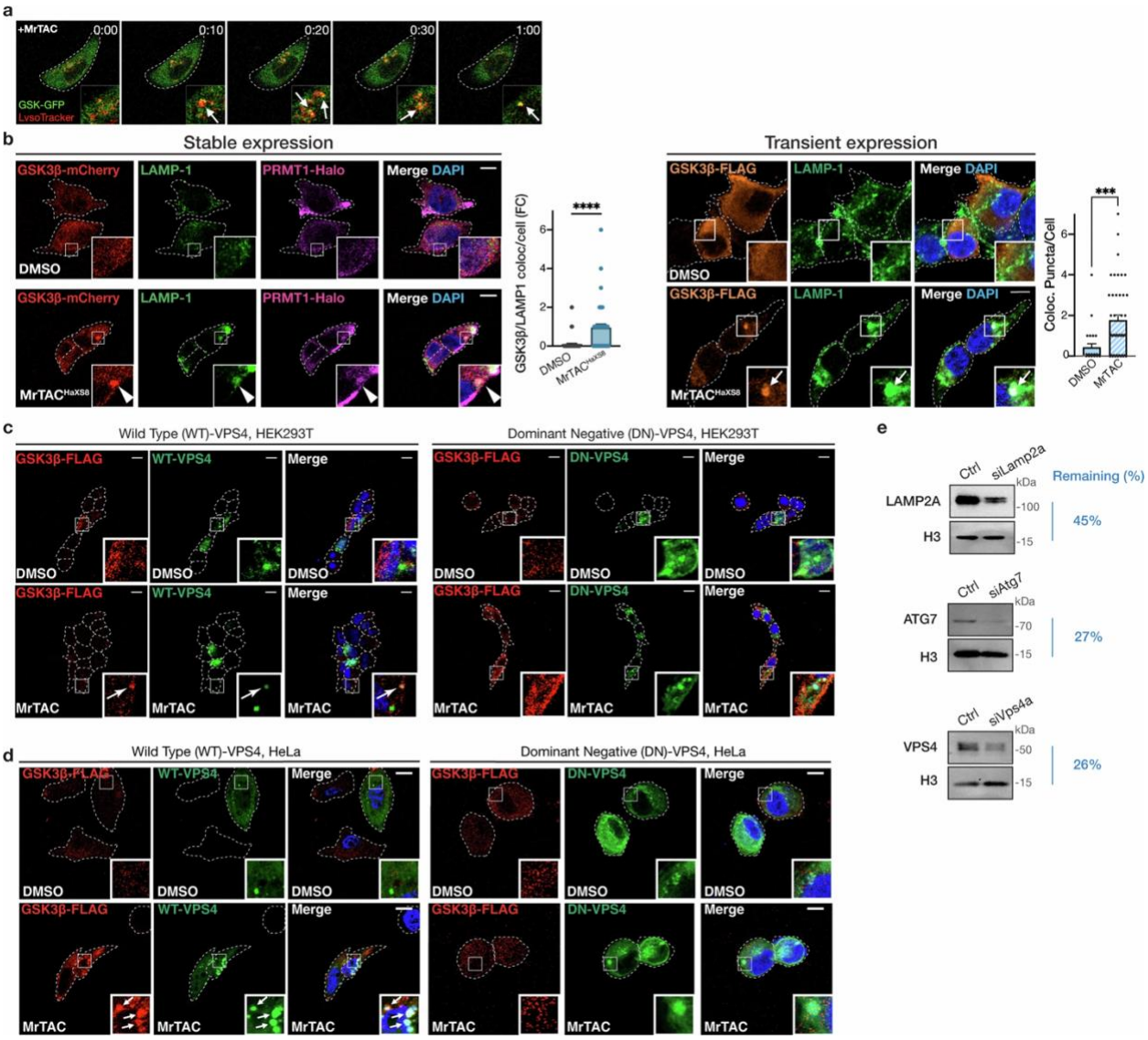

Figure 1.8 VPS4-mediated GSK3β sequestration during MrTAC treatment.

(A) Live-cell confocal microscopy of GSK3β-SNAP-GFP in HeLa cells incubated with Lysotracker over 60 min with 0.5 µM MrTAC^{HaXS8}. Image was captured every 10 min. Arrows note colocalization. **(B)** Colocalization of GSK3β-SNAP-FLAG with lysosomal-associated membrane protein (LAMP-1) after MrTAC^{HaXS8} treatment in stable HEK293 cells (0.5 µM, 3 h, mean colocalizing structures over $n = 39_{DMSO}$ and 54_{MrTAC} cells; left) or transiently expressing HEK293T cells (10 µM, 3 h, mean colocalizing structures over $n = 24_{DMSO}$ and 45_{MrTAC} cells; right). Arrows mark colocalization. For either experiment, graphs depict the number of colocalized GSK3β/LAMP-1 puncta within each cell. $^{****}P < 0.0001$ and $^{***}P < 0.0010$ by unpaired two-sided t-tests. **(C)** Colocalization of HEK293T cells expressing GSK3β-SNAP-FLAG (red) with either wild-type (WT) or dominant negative (DN) VPS4-GFP after MrTAC^{HaXS8} treatment (10 µM, 1 h). **(D)** Colocalization of HeLa cells expressing GSK3β-SNAP-FLAG

(red) with either wild-type (WT) or dominant negative (DN) VPS4-GFP after MrTAC^{HaXS8} treatment (0.5 μM, 2 h). **(E)** Immunoblot analysis of target protein levels of siRNA-mediated knockdown of *Lamp2a*, *Atg7* or *Vps4a* (100 nM) collected on day of experiment completion (n = 3 experiments). Scale bars are 10 μm. Data are represented as means ± SEM.

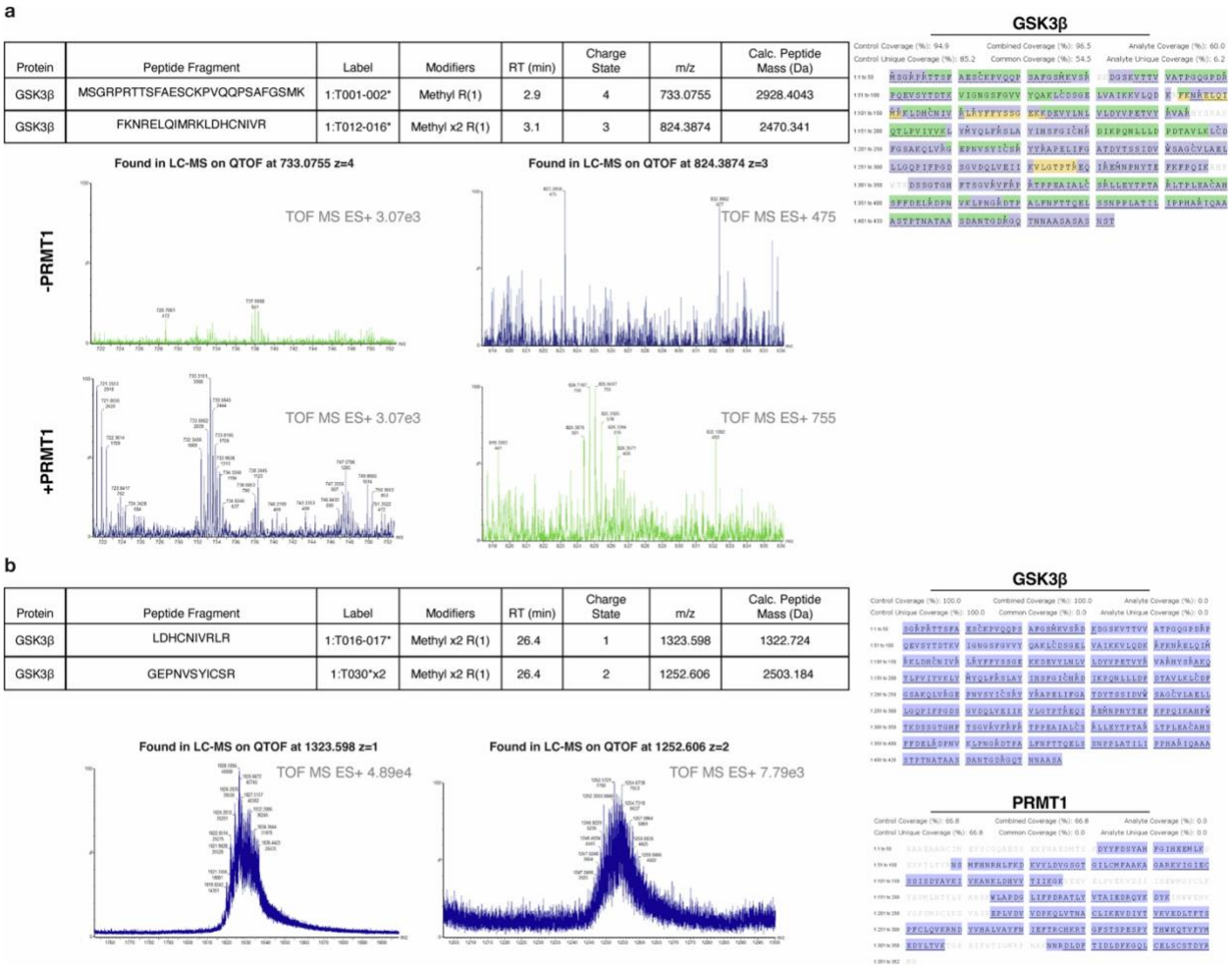

Figure 1.9 Methylation of GSK3β by PRMT1.

(A) Mass spectrometry of in vitro methylated GSK3β samples in presence (bottom) or absence (top) of PRMT1 and the associated protein coverage by LC–MS QTOF (left). Associated coverage map of GSK3β by LC–MS QTOF (right). **(B)** Mass spectrometry of methylated GSK3β following FLAG immunoprecipitation of MrTAC-treated HEK293 cells that transiently express PRMT1-Halo and GSK3β-SNAP-FLAG (10 µM, 2 h with 400 nM bafilomycin and 10 µM MG132; left). Associated coverage maps of GSK3β and recruited PRMT1 by LC–MS QTOF (right).

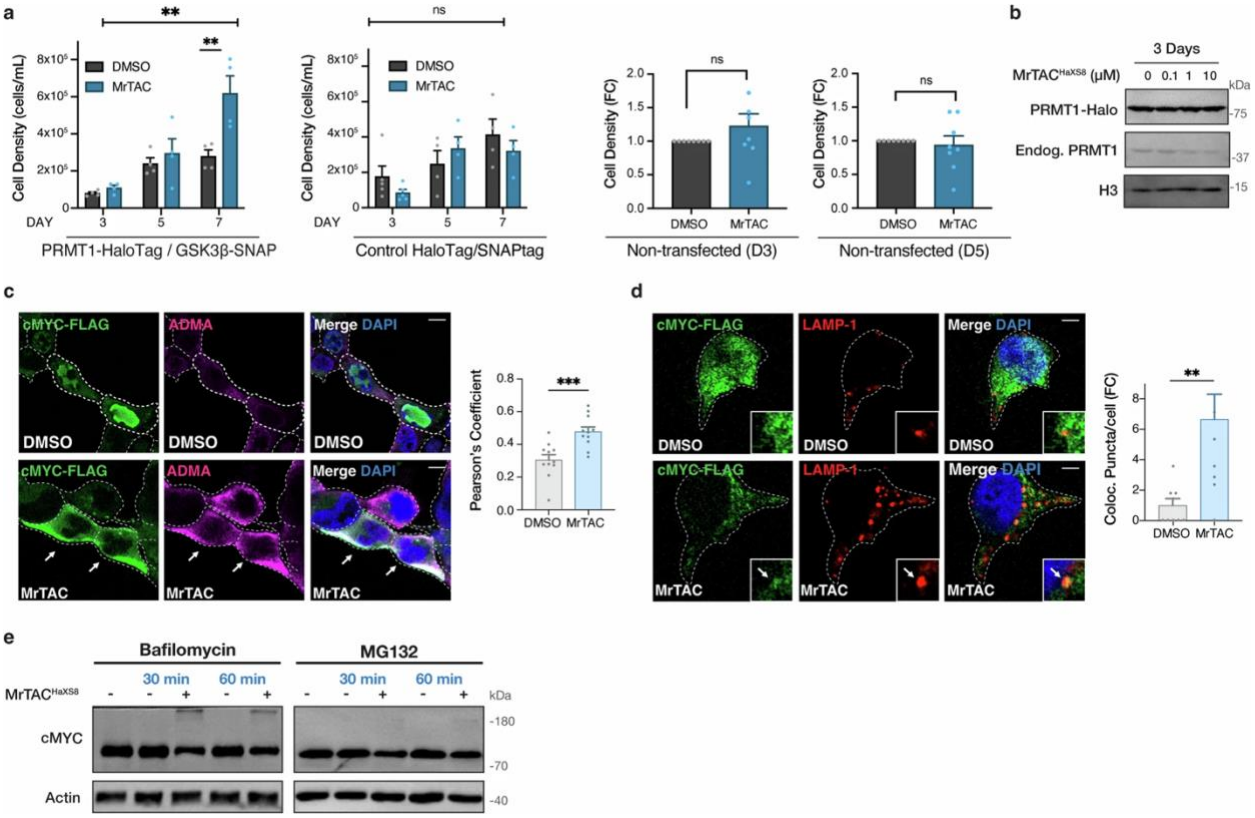

Figure 1.10 MrTAC degradation of SNAP-tagged proteins reshapes cell signaling.

(A) Proliferation following MrTAC^{HaXS8} treatment (0.5 μM) in HeLa cells expressing either Halo-PRMT1/GSK3β-SNAP or Halo-empty/SNAP-empty over seven days (n = 4 experiments; left). $^{**}P < 0.0051$ drug effect and $^{**}P_{D7} < 0.0010$ by two-way ANOVA with Bonferroni's multiple comparisons. Proliferation of non-transfected HeLa cells treated with MrTAC^{HaXS8} at indicated times (n = 8 experiments), ns by unpaired two-sided t-tests (right). **(B)** Immunoblot analysis of PRMT1 protein levels (Halo-tagged and endogenous) in MrTAC^{HaXS8}-treated HEK293 cells expressing CRISPR-integrated PRMT1-Halo/GSK3β-SNAP over 3 days (n = 3 experiments). **(C)** Confocal microscopy of c-MYC-SNAP-FLAG colocalization with asymmetric dimethylarginine (ADMA) antibody after MrTAC treatment (1.5 h, 10 μM; left). Thick outlines mark low colocalization, and arrows mark high colocalization. Scale bar is 5 μm. Bars (right) show average Pearson correlation coefficient between FLAG/ADMA channels across all cells marked with DAPI (n = 11 fields of view). $^{***}P < 0.0009$ by two-sided unpaired t-test. **(D)** Confocal microscopy of c-MYC-SNAP-FLAG colocalization with lysosomal-associated membrane protein (LAMP-1) in MrTAC-treated cells (1 h, 10 μM; left). Arrows indicate colocalization, scale bar is 10 μm. Bars (right) show average number of colocalized structures within a cell over 9 fields of view as normalized to DMSO condition. $^{**}P < 0.0046$ by two-sided unpaired t-test. **(E)** Immunoblot analysis of c-MYC-SNAP levels in cells treated with MrTAC (10 μM) at indicated times with cycloheximide (10 μM). Cells were treated in

the presence of bafilomycin (100 nM) or MG132 (5 μM; n = 2 experiments). Data are represented as means ± SEM.

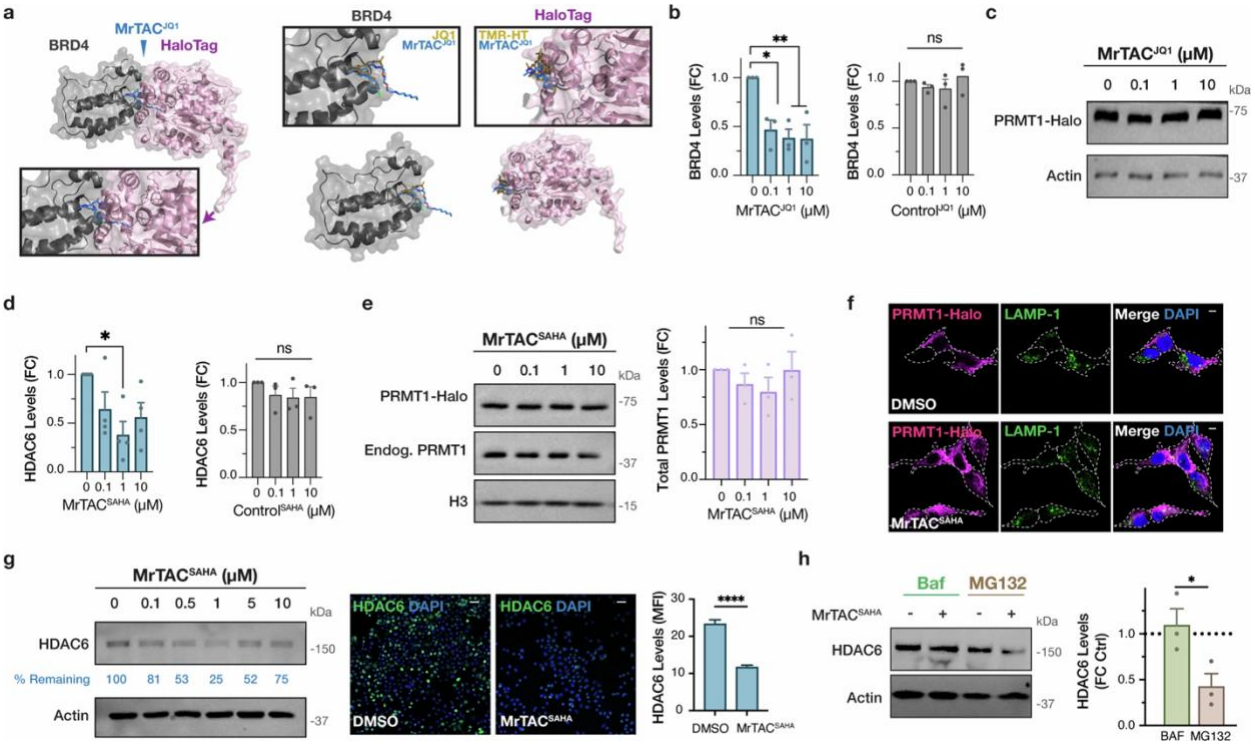

Figure 1.11 Degradation of endogenous targets.

(A) Modeling of MrTAC^{JQ1}. MrTAC^{JQ1} bound to BRD4 bromodomain 1 (BD1; PDB: 3MXF) and HaloTag (PDB: 6U32). Pink arrow shows direction of PRMT1 fusion (left). BRD4 BD1 binding to MrTAC^{JQ1} compared against JQ1 ligand (gold; middle). HaloTag binding to MrTAC^{JQ1} compared against tetramethylrhodamine-HaloTag (TMR-HT) ligand (gold; right). **(B)** Quantification of immunoblot in Fig 5b by one-way ANOVA with Bonferroni's multiple comparisons, $*P_{0.1} < 0.0169$, $**P_1 < 0.0076$, $**P_{10} < 0.0069$. **(C)** Immunoblot analysis of PRMT1-Halo levels through a 4-h MrTAC^{JQ1} treatment (n = 3). **(D)** Quantification of immunoblot in Fig 5f by one-way ANOVA with Bonferroni's multiple comparisons, $*P < 0.0221$ ($n_{MrTAC} = 4$, $n_{Control} = 3$). **(E)** Immunoblot analysis of PRMT1 levels through a 4-h MrTAC^{SAHA} treatment in HEK293s stably expressing PRMT1-Halo (n = 3; left). Right quantifies levels of total PRMT1 (Halo-tagged and monomeric, uncropped blot in source data) relative to 0 μM; ns by one-way ANOVA with Bonferroni's multiple comparisons. **(F)** Immunofluorescence of PRMT1-Halo in stably expressing HEK293 cells following a 4-h MrTAC^{SAHA} treatment with a lysosome-associated membrane protein 1 (LAMP-1) costain; scale bar is 5 μm. **(G)** Analysis of HDAC6 levels through a 4-h MrTAC^{SAHA} treatment in HeLa cells transiently expressing PRMT1-Halo by immunoblot (n = 3; left) and immunofluorescence (n = 200 cells; middle); graph shows HDAC6 intensity over total cells marked by DAPI. $****P < 0.0001$ by unpaired two-sided t-test (right). **(H)** Immunoblot analysis of HDAC6 levels with MrTAC^{SAHA} (1 μM, 4 h) in HEK293s stably expressing PRMT1-Halo co-treated with lysosome inhibitor bafilomycin (400 nM, 2 h pre-treatment) or

proteasome inhibitor MG132 (10 μM; n = 3; left). Right, total levels of HDAC6 in +MrTAC cells relative to either group's -MrTAC condition. *$P < 0.0445$ by unpaired two-sided t-test. Immunoblots are representative of at least three independent experiments. Data are represented as means ± SEM.

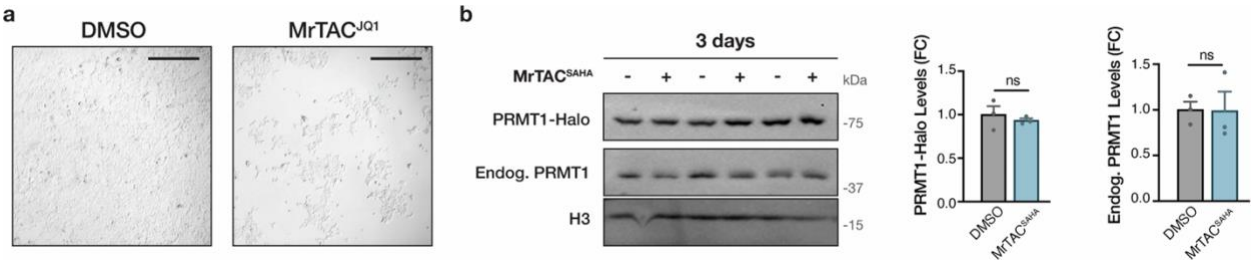

Figure 1.12 Effect of endogenous MrTAC degradation on cell function.

(A) Representative cell density of HEK293 cells stably expressing PRMT1-HaloTag following 6 days of 1 μM MrTAC^{JQ1} or DMSO vehicle (n = 3 experiments); scale bar is 500 μm. **(B)** Immunoblot analysis of Halo-tagged and endogenous PRMT1 levels through a 3-day MrTAC^{SAHA} treatment at 1 μM in HEK293s stably expressing PRMT1-Halo (left; n = 3 experiments). Middle and right quantify total levels of PRMT1-Halo and endogenous PRMT1, respectively, as normalized to the DMSO condition, ns by unpaired two-sided t-test. All quantified values are means ± SEM.

CHAPTER 2

Exploration of protein degradability enables fully endogenous MrTAC degraders

Laurence J Seabrook[1], Endri Karaj[2,11], Shaimaa Sindi[2,11], Glen Brodie[3], Catherine R Livelo[4], Carolina N Franco[4], Melissa Campos[1], Jack T Leonard[5], Fangyuan Gao[6,7], Dorota Skowronska-Krawczyk[6,7], Matthew E Griffin[4,5,8], Stuart J Conway[3], Amit Choudhary[2,9,10,*] & Lauren V Albrecht[1,4,12*]

Affiliations

[1] Department of Developmental & Cell Biology, School of Biological Sciences, University of California, Irvine, Irvine, CA, USA
[2] Chemical Biology and Therapeutics Science Program, Broad Institute of MIT and Harvard, Cambridge, MA, United States
[3] Department of Chemistry and Biochemistry, University of California, Los Angeles, CA, USA
[4] Department of Pharmaceutical Sciences, School of Pharmacy & Pharmaceutical Sciences, University of California, Irvine, Irvine, CA, USA
[5] Department of Chemistry, School of Physical Sciences, University of California, Irvine, Irvine, CA, USA
[6] Center for Translational Vision Research, Department of Ophthalmology, Gavin Herbert Eye Institute, University of California, Irvine, Irvine, California, USA
[7] Department of Physiology and Biophysics, University of California, Irvine, California, USA
[8] Department of Biochemistry and Molecular Biology, School of Biological Sciences, University of California, Irvine, Irvine, CA, USA
[9] Divisions of Renal Medicine and Engineering, Brigham and Women's Hospital, Boston, MA, United States
[10] Department of Medicine, Harvard Medical School, Boston, MA, USA
[11] These authors contributed equally
[12] Lead contact
* Correspondence achoudhary@bwh.harvard.edu (A.C.), lvalbrec@uci.edu (L.A.)

This chapter is derived from the manuscript published in Cell Chem:

Chem *12*, 102998, Jun 11 2026. doi: 10.1016/j.chempr.2026.102998.

2.1 Abstract

Proteins can be degraded by hijacking natural degrons with small molecules, but most degraders rely on the same proteasome-targeting degron. Motivated by the need for chemically exploitable degrons, this study leverages the lysosome-targeting methylarginine degron for development of Methylarginine TArgeting Chimeras (MrTACs). First, lysosomal-capture proteomics identified substrates naturally modified by methylarginine degrons. Next, a tag-based protein library was used to understand the characteristics that affect degradation by MrTAC, which induces methylarginine degrons by recruiting protein arginine methyltransferases (PRMTs). MrTAC degraded proteins regardless of their native proteolytic route, including targets that have eluded classic degrader modalities, across multiple PRMTs. We leveraged this for endogenous MrTACs that recruit PRMTs with repurposed inhibitors, which could be transformed into silent recruiters by group-transfer chemistry. MrTACs drove <95% target degradation across disease-linked proteins at nanomolar doses. Overall, this study integrates native and chemically-induced degradation to platform fully endogenous, therapeutically viable degraders.

2.2 Introduction

Quality control is fundamental to all living organisms and requires constant surveillance of the proteome. Dynamic regulation of the proteome is enabled by degrons, which are short peptide sequences (12-30 amino acids) that serve as degradation codes which facilitate recognition of degradation machinery (Bachmair et al., 1996; Rechsteiner and Rogers, 1996). For example, N-degrons and C-degrons signal E3 ubiquitin ligases to recognize a target protein that should be degraded through the ubiquitin-proteasome system (Varshavsky, 2019; Tasaki et al., 2005). The rise of targeted protein degradation (TPD) exemplifies the power of using degrons for controlled

elimination of disease-causing proteins. Molecular glues and proteolysis targeting chimeras (PROTACs) are small molecule 'degraders' that force proteins into proximity with the ubiquitin-proteasome system (Schreiber, 2021). Degrader molecules have the potential to revolutionize therapeutics by overcoming limitations of small molecule inhibitors such as poor protein druggability, acquired resistance, and low tissue specificity (Pettersson and Crews, 2019; Békés et al., 2022). Novel chemical approaches have expanded the repertoire of proteins that can be targeted by degraders and the E3 ligases available for recruitment (Pergu et al., 2023; Reddi et al., 2021; Xiao et al., 2025). Degron discovery efforts have provided a key framework to effectively prioritize 'likely degradable' proteins using empirical data, predictive modeling, and machine learning tools (Bondeson, et al., 2018; Schneider et al., 2021; Zhang et al., 2022; Li et al., 2022). Emerging research shows that degron selectivity can be a result of many features, including encoded motifs, three-dimensional structural features, and post-translational modifications (Jevtić et al., 2021; Seabrook et al., 2025; Lee et al., 2023). The complete repertoire of endogenous degrons across the proteome is incompletely defined.

Previously, our work uncovered an endogenous lysosomal degron that is activated by protein arginine methylation (Seabrook et al., 2024; Franco et al., 2023; Albrecht et al., 2018). We show that protein arginine methyltransferase 1 (PRMT1) catalyzes asymmetric dimethylarginine modifications on a select set of proteins to initiate their lysosomal proteolysis, which regulates downstream cellular function (Albrecht et al., 2018). However, arginine methylation occurs as frequently as serine phosphorylation, which suggests that methyl-proteolysis may regulate many substrates throughout the proteome (Larsen et al., 2016; Bedford and Clarke, 2009). We recently adapted this degron into a targeted protein degrader modality, methylarginine targeting chimera

(MrTAC), where recruiting a HaloTagged PRMT1 to a target protein could induce target methylation and downstream lysosomal degradation (Seabrook et al., 2024). Proximity-based modalities can recruit endogenous enzymes without disturbing activity by using activators, silent ligands, or inhibitor-elimination strategies (Pergu et al., 2023). In contrast, endogenous MrTACs have thus far been limited by the lack of a suitable ligand that does not block methyltransferase activity.

In the present work, we provide a proteomic resource that maps arginine methylated substrates within the lysosome, constituting the lysosomal methyl-degrome. Newfound rules and determinants of degradation are leveraged into a chemically induced space to address how biological variance affects MrTAC, the degrader counterpart of the methylarginine degron. By exploring protein degradability with a modular fusion protein tagging system, we shed light onto the rules underlying effective MrTAC degradation and discover that all three classes of PRMT enzymes are capable of MrTAC degradation. We leverage this to develop MrTAC degraders capable of recruiting PRMTs through two mechanisms: repurposing inhibitors to recruit endogenous PRMTs, or by transforming inhibitors into silent recruiters for inhibitor-directed group-transfer (Pergu et al., 2023; Reddi et al., 2021). Successful transformation of a native degron into a generalizable degrader highlights the therapeutic potential of this class of molecules.

2.3 Results

Enrichment of Methylarginine Degron Substrates by Lysosomal Proteomics

Discoveries of proteasomal degrons provide crucial mechanistic insight into how cells maintain proteostasis in steady-state conditions and in response to stimuli (Varshavsky 2019). Our goal was

to delineate the role of lysosomal degrons in proteomic maintenance. Arginine methylation modifications occur as frequently as serine phosphorylation, where over 15,386 arginine methylation events have been identified over 5,255 unique proteins (25.4% of proteome) (Maron et al., 2021). To approximate the global prevalence of methylarginine degron substrates, we probed lysosomal proteomic datasets to identify potential substrates of this degron (Akter et al., 2023). We excluded lysosomal membrane proteins and proteolytic enzymes to focus our analyses on proteins that associate with lysosomes but are not involved in lysosomal function, signaling, or structure. Within this pool of putative lysosomal substrates, a substantial fraction has at least one arginine methylation site (30.3%), which is higher than the global abundance of arginine methylation within the human proteome (25.4%) (Larsen et al., 2016). The enrichment of arginine methylation across lysosome-associated proteins provides a basis for mapping substrates modified by methylarginine degrons, constituting the methyl-degrome.

Prior reports show that methylarginine degrons are deposited across several cytosolic proteins in response to stimuli. Canonical Wnt stimuli rapidly cause an enrichment of arginine methylated proteins within lysosomes after minutes (Albrecht et al., 2018). Given this, we leveraged Wnt as an initial degron discovery platform to map the lysosomal methyl-degrome. Intact lysosomes were isolated from cells by lysosomal immunoprecipitation (LysoIP) under basal or Wnt-stimulated conditions (**Figure 2.1A**). HEK293T cells stably expressing HA-tagged TMEM192 were stimulated with Wnt3a for 20 minutes and subjected to HA immunoprecipitation to isolate intact lysosomes. Treatment with lysosomal inhibitor bafilomycin prevented breakdown of lysosomal substrates. Proteomics reveal 264 proteins unique to Wnt-activated conditions (**Figure 2.1B**). Over half of these proteins (56%) are modified by arginine methylation on at least one site, which is

much higher than that of the aforementioned lysosomal datasets (30.3%) and the global human proteome (25.4%) (**Figure 2.1B**). Gene ontology (GO) of putative methylarginine degron substrates shows enrichment across diverse biological pathways (**Figure 2.1C**). Our previous studies identify pyridoxal kinase (PDXK), a rate-limiting metabolic enzyme that is methylated and degraded in lysosomes (Franco et al., 2023). In line with this, our analyses similarly show a significant enrichment in metabolic processes, which suggests that methylarginine degrons may function as a generalized metabolic control switch. Crosstalk between growth factor signaling networks is a central tenet of tissue-wide signal transduction (Massagué et al., 2023). Our analyses identify several constituents of MAPK signaling as methylarginine degron substrates, including RAS, MAPK3, MAP2K7, MAP4K4, which suggests that lysosomal proteolysis may act as an underlying mechanism of the Wnt-MAPK signaling axis (Albrecht et al., 2021). Cellular compartment analysis showed methylarginine degron substrates are found within the cytosol, organelles, protein-protein complexes, and in membranes (**Figure 2.1C**). To exclude proteins that may have been in complexes with bona fide methylarginine degron substrates during the LysoIP, additional filtering was performed to focus on targets that have been empirically shown to be PRMT substrates (**Figure 2.1D**). Arginine methylated substrates were associated with enzymatic functions while the unmethylated proteins were more strongly associated with binding functions (**Figure 2.1D**). This may suggest that the proteins directly modified by PRMTs for degradation are critical for cell dynamics and are priority targets for native degradation by this pathway.

Previously, protein size has been shown to be a crucial determinant of whether a protein is degraded through proteasomes or lysosomes (de Duve and Wattiaux, 1996). In our system, protein size analyses showed that the methylated substrates were of a larger size than their unmethylated

counterparts across the 264 lysosomal proteins, which may reflect increased protein surface area and arginine accessibility for methylation by PRMTs (**Figure 2.1E**). Protein flexibility and disorder have been correlated with both increased degradability (Fishbain et al., 2015; van der Lee et al., 2014; Zammit et al., 2025; Kaushik and Cuervo, 2012) and with higher levels of protein arginine methylation (Wang and Bedford, 2023). However, protein disorder was similar across the methylated and unmethylated protein subsets identified in lysosomes (**Figure 2.1F**), indicating that disorder is independent of methylarginine degron potential. Finally, analyses were performed to assess correlations of protein half-life and methylarginine degron substrates. Classically, lysosomes are thought to be the primary site for degrading long-lived proteins, as defined by a turnover rate above 8 hours (Li et al., 2021). Both methylated and unmethylated subsets were predominantly composed of long-lived proteins, validating that turnover is fundamental to lysosomal substrates beyond the methylarginine degron (**Figure 2.1G**).

A Modular Approach to Screen Protein Degradability by MrTAC

To this point, our datasets provide insight into the endogenous methylarginine degron pathway. Recent studies show the power of degron discovery efforts to improve efficacy of proteasomal degrader modalities (Bondeson et al., 2018; Schneider et al., 2021; Zhang et al., 2022; Li et al., 2022). MrTAC exploits endogenous methylarginine degrons for targeted lysosomal proteolysis by recruiting PRMT enzymes to substrates (Seabrook et al., 2024). Given this, we sought to evaluate how endogenous properties could be applied to advance targeted degradation and inform substrate selection for MrTAC.

To explore the effects of biological variance on MrTAC degradation, we generated a diverse library of protein targets and screened degradation by MrTAC. We used a modular tagging system to probe target degradation using a heterobifunctional MrTAC molecule that recruits a HaloTagged PRMT to a SNAP-tagged protein target (**Figure 2.2A**), as previously described (Seabrook et al., 2024). By recruiting proteins via fusion tags, this strategy overcomes the confounding chemical variables of endogenous target recruitment, such as binding affinity and residence time, which affect TPD (Fan et al., 2025). We selected PRMT1 for these degradation assays given its sufficiency for MrTAC degradation and role in native regulation by methylarginine degrons (Seabrook et al., 2024; Albrecht et al., 2018). Through simultaneous expression of a PRMT1-Halo and a SNAP-tagged protein target, PRMT1 can be recruited to a protein target through treatment with HaXS8 (denoted here as $MrTAC^{HaXS8}$), which binds HaloTag and SNAP-tag. In developing the SNAP-tagged library, we nominated proteins that demonstrate diversity in structure, function, and localization in order to understand how target protein differences affect proteolysis (Schneider et al., 2021) (**Figure 2.2B**). We evaluated features known to affect PROTAC degradation, including turnover and subcellular localization. We also sought to understand whether the features affecting natural methylarginine degrons would affect chemically induced degradation, including protein disorder, the number of surface-exposed arginines, and the native methylation status of the protein.

We first evaluated protein levels in response to $MrTAC^{HaXS8}$ treatment to assign protein degradation values. Degradation screens of the SNAP library were performed in HEK293 cells stably expressing PRMT1-Halo. Cells expressing each SNAP-target were treated with $MrTAC^{HaXS8}$ and the stepwise process of target protein engagement, ternary complex formation,

and degradation was assessed (**Figure 2.3A**). Maximal degradation was calculated for 24 hour MrTAC^{HaXS8} treatments and protein levels were measured by immunoblotting. Previous work shows that 1 μM MrTAC^{HaXS8} leads to efficient Halo-SNAP interaction across multiple cell lines regardless of differences in target localization, characteristics, and expression levels (Seabrook et al., 2024; Dotson and Ngo, 2022; Erhart et al., 2013). Given this, cells were treated with 1 μM MrTAC^{HaXS8} in these analyses. We first validated that protein levels of a model substrate, glycogen synthase kinase 3β (GSK3β), were significantly reduced in MrTAC^{HaXS8} treated cells relative to the DMSO control (**Figure 2.3A**). Individual SNAP-fused protein levels were similarly evaluated by immunoblotting (**Figure 2.3A, Figure 2.7A**). Compared to DMSO controls, MrTAC^{HaXS8} treated cells displayed reduced levels of novel protein targets, AXIN1, Rab5b, phosphofructokinase 1 (PFK-1), nucleoporin 43 (NUP43), YTH N6-methyladenosine RNA binding protein 1 (YTHDF1), calcium/calmodulin dependent protein kinase 2 (CAMKK2), and mitochondrial import receptor subunit 20 (TOMM20) (**Figure 2.3A, Figure 2.7A**). Notably, several proteins associated with oncogenic progression could also be reduced by MrTAC treatment including AXIN1, PFK-1, YTHDF1, CAMKK2, GSK3β, and TOMM20, which have been the focus of drug discovery efforts (Wang et al., 2021; Peng et al., 2023; Sun et al., 2022; Vijay et al., 2019; Tomaszewski et al., 2022; Yin et al., 2025). PRMT1-Halo was stably expressed in excess to each target and was therefore unaffected by treatment (**Figure 2.7B**). To validate whether proximity-induced methylation is required for target degradation, protein levels were evaluated in cells expressing a catalytically dead PRMT1 (Lin et al., 1996). No significant changes were observed upon MrTAC treatments across the top SNAP library hits (AXIN1, Rab5b, PFK-1, NUP43, and GSK3β), despite differences in the structure, function, and localization of each target (**Figure 2.3B, Figure 2.7C**). These data are consistent with the model that methylation enables

target degradation. Notably, five of the top hits degraded by MrTAC are structurally elucidated and have known ligands, which could enable rational design (**Figure 2.2C-D**). Established GSK3β ligands have been leveraged by PROTAC molecules (Guiardigni et al., 2023; Qu et al., 2021; Holmqvist et al., 2025) and could similarly enable endogenous MrTAC recruiting ligands. These empirical analyses show MrTAC is capable of degrading a library of proteins through chemically induced PRMT1 recruitment.

We next aimed to understand how structural features of the target protein may contribute to differences in protein degradation. Research into native degrons reveals that protein disorder often trends with increased protein degradation. However, there was no apparent difference in protein disorder in our LysoIP datasets (**Figure 2.1F**). Consistent with this, we also found that in response to MrTAC^{HaXS8} treatment, there was no clear difference in degradability of proteins with high disorder and those with low disorder (**Figure 2.3C**). For example, the most ordered proteins NUP43 and Rab5b degraded at approximately the same rate as the most disordered protein, AXIN1 (49%, 58%, and 67%, respectively). Degraders are also affected by the natural turnover rate of the target protein, which may reflect the inherent degradability of the protein and behave as a proxy for new protein synthesis (Riching et al., 2018). Although many of the long-lived proteins could be degraded by MrTAC, we were surprised to see that proteins with intermediate half-lives like AXIN1 (17 hours) could also be strongly degraded (**Figure 2.3C**). Together, these data show that the guidelines initially thought to control PROTAC degradability may not dictate MrTAC degradability.

To examine whether MrTAC degradation is affected by the same variables as native methylarginine degrons, we compared methylation-related variables against MrTAC degradation. LysoIP experiments showed that methylated lysosomal proteins have larger molecular weights relative to their unmethylated counterparts (71.5 kDa versus 42.9 kDa), which could suggest selectivity of the native methylarginine degron. Chemically inducing methylation via MrTAC was sufficient to reduce the levels of both Rab5b, the smallest tested protein (24 kDa), and HDAC6, the largest tested SNAP protein (131 kDa). Thus, MrTAC deviates from endogenous preferences of methylarginine degron proteolysis and can be generalizable across target molecular weights. We reasoned that MrTAC degradation might also be affected by differences in the abundance of surface-exposed arginines available for a methylation event. However, we found that proteins with relatively low arginine counts could still be degraded (**Figure 2.3C**). This finding is consistent with our previous observations that the methylation of even a single arginine residue can be sufficient for degradation during native methylarginine degron proteolysis (Franco et al., 2023). Finally, we hypothesized that endogenous PRMT protein substrates would be most susceptible to MrTAC degradability. Top MrTAC hits by this assay included both natural substrates (GSK3β and PFK-1) and neo-substrates (Rab5b, NUP43, and CAMKK2), which highlights the ability of MrTAC to degrade proteins regardless of whether they are natively regulated by methylarginine degrons (**Figure 2.3C**). The rules governing endogenous methylarginine degrons may not apply to chemically induced settings, which opens MrTAC application towards a wide range of protein families and undruggable targets.

To further extend our analyses of how different protein properties influence MrTAC, we compared side-by-side degradability of protein isoform pairs. For these analyses, we selected AXIN1 and

AXIN2, crucial scaffolding proteins that share 45% sequence homology, similar cellular localization, and activity (Clevers and Nusse, 2012). Cells treated with MrTAC^{HaXS8} showed stable ternary complex formation of PRMT1 with AXIN1 and AXIN2 (**Figure 2.7A**). AXIN1 protein levels were significantly reduced by MrTAC^{HaXS8} treatment. In contrast, AXIN2 protein levels were maintained across MrTAC^{HaXS8} and DMSO treatments, indicating that ternary complex formation was insufficient for subsequent proteolysis. Sequence analyses revealed a distinct difference in arginine content between AXIN1 and AXIN2 with 69 surface-exposed arginines for AXIN1 and 54 for AXIN2, suggesting that either differences in arginine content or PRMT accessibility may influence targeted degradation (**Figure 2.3A**). This aligns with the recent discovery that successful degradation by molecular glues correlates with increased lysine abundance in structurally defined regions, presumably due to an increased density of lysine residues available for modification by E2 ubiquitin ligases (Baek et al., 2025). Next, we assessed two proteins in the TGFβ pathway, SMAD4 and SMAD7, which share similar functional domains. In contrast to the isoform-selective degradation profiles of AXIN1 and AXIN2, MrTAC reduced the levels of both SMAD4 and SMAD7 with similar efficiency despite minor differences in protein structure (**Figure 2.3A**). These data show that MrTAC degradation is robust against differences in protein structure and activity but may be affected by a protein's ability to be methylated by PRMTs.

Prior work shows that MrTAC can degrade soluble proteins within the cytosol and nucleus (Seabrook et al., 2024). Our SNAP library includes several soluble proteins as well as proteins associated with more complex cellular structures that may affect successful MrTAC targeting. Among the top hit proteins, MrTAC reduced levels of proteins localized to unique structures,

including AXIN1 (phase-separated condensates), TOMM20 (on mitochondrial membranes), and Rab5b (on early endosomal membranes). As our top degraded protein, AXIN1 was nominated for immunofluorescent analysis in response to MrTAC^{HaXS8} treatment. While AXIN1 is typically observed as a cytosolic protein that is associated with phase condensates, a 2 hour incubation with MrTAC^{HaXS8} led to relocalization of AXIN1 towards lysosomal structures marked by LAMP1, consistent with prior MrTAC^{HaXS8} degradation kinetics (**Figure 2.3D**). Similar results were observed in tracking the localization of an mTurquoise-tagged TOMM20-SNAP, which lines the outer membrane of mitochondria and could be effectively targeted by MrTAC^{HaXS8} (**Figure 2.7D**). These data demonstrate that MrTAC can target proteins across different subcellular domains.

Effective target selection is a crucial element to any degrader campaign. Thus far, these data show that MrTAC can target proteins across diverse features and properties. We sought to understand whether aggregating the tested features could be used to generate a predictive scoring system for MrTAC degradation. We averaged each tested variable's score (disorder, turnover, arginine count, methylation, localization) and compared the aggregated score against degradation data. We found that the highest-scoring proteins (PFK-1, AXIN1, HDAC6) were all successful MrTAC targets. However, the strength of degradation did not always correlate with the aggregated score as in the case of SMAD4, which was only mildly degraded but scored the same as our model substrate, GSK3β (47.8 and 58.9, respectively). Reducing the number of variables to only include disorder, turnover, and arginine count improved the correlative strength of this prediction, where all proteins with a score of over 40 could be strongly degraded (**Figure 2.3E**). This included several of the top hits, such as AXIN1, PFK-1, GSK3β, and CAMKK2. Understanding how innate differences in

protein degradability affect MrTAC degradation results in a predictive model that will streamline target selection in future MrTAC campaigns.

Generalizability of PRMTs for MrTAC Degradation

PRMTs are divided into three classes organized by the type of methylation they catalyze: Type III PRMTs catalyze monomethylation (MMA, PRMT7), Type II PRMTs catalyze symmetric dimethylation (SDMA, PRMT5, 9), and Type I PRMTs catalyze asymmetric dimethylation (ADMA, PRMT-1, 2, 3, 4, 6, 8) of arginine residues (Bedford and Clarke, 2009) (**Figure 2.4A**). Thus far, only PRMT1 has been assessed in MrTAC degradation. Whether alternative PRMTs can also be leveraged for TPD is unknown. To explore this, we used our modular tagging system to assess degradability of a model target, GSK3β-SNAP, using HaloTagged PRMTs from each of the three PRMT classes (**Figure 2.4B-C**). Cells expressing 4 HaloTagged PRMTs were evaluated following 24 hour MrTAC^{HaXS8} (1 μM) or DMSO treatments. Immunoblotting showed that PRMT1 efficiently degraded GSK3β (60% degraded), as expected (**Figure 2.4C**). Another ADMA-catalyzing enzyme was also sufficient to degrade GSK3β as demonstrated by PRMT4 (60% degraded). Surprisingly, GSK3β was also degraded by alternative arginine modification types, where inducing SDMA via PRMT5 recruitment led to 51% protein degradation. Finally, MMA addition by recruitment of PRMT7 also degraded GSK3β (48% degraded). To validate that MrTAC degradation was on-mechanism when using PRMT4, 5, and 7, we assessed the levels of GSK3β-SNAP degradation when MrTAC was treated in the presence of methylation or lysosome inhibitors. Across three classes of PRMT enzymes, degradation could be rescued by lysosomal inhibition with bafilomycin or methylation inhibition with adenosine dialdehyde (AdOx) (**Figure 2.4D-E**). This demonstrates a shared mechanism of MrTAC degradation across the PRMT family.

Together, these data suggest that PRMTs are equally capable of depositing methylarginine degrons on protein targets and that all three PRMT classes may be used for targeted degradation by MrTAC.

Repurposing Inhibitors for Endogenous PRMT Recruitment

Recruiting endogenous proteolytic machinery is crucial for the therapeutic utility of a new degrader modality (Schreiber, 2024; Chirnomas et al., 2023). For endogenous MrTAC degraders, PRMT enzymes must be recruited while retaining their enzymatic activity. This is challenging as silent or non-inhibitory binders of PRMTs are scarce. In contrast, many PRMT inhibitors have been identified, including several in clinical trials of hematologic malignancies (Wu et al., 2021; Wu et al., 2022; Watts et al., 2024). Methyltransferase inhibitors have been repurposed into PROTAC degraders designed to eliminate PRMTs by attaching E3 ligands onto ligands for PRMT1, PRMT4, and PRMT5 (Shen et al., 2020; Guo et al., 2024; Ju et al., 2025). PRMT5 PROTACs have shown the most success with defined exit vectors and highly potent compounds. Several studies suggest that in some cases, inhibitors can be used to recruit enzymes without altering activity through a catch-and-release mechanism, where the enzyme is recruited to the target protein and is subsequently released from the compound as an active enzyme. For example, Gray, Crabtree, and colleagues used CDK9 inhibitors to recruit CDK9 kinase for target phosphorylation of RNA polymerase II, thereby enhancing transcription elongation (Sarott et al., 2024). We hypothesized that MrTACs could be developed using the same approach with PRMT inhibitors previously employed in PROTACs, with PRMTs now serving as effectors rather than targets.

To recruit endogenous PRMT5, we leveraged GSK3326595 as a ligand given that it potently binds to the active site and is cell permeable (Watts et al., 2024; Shen et al., 2020; Guo et al., 2024; Ju et al., 2025). BRD4 was selected as an initial target protein as it is a hallmark target for TPD, has a well-established ligand (JQ1), and could be degraded by MrTAC in prior studies (Seabrook et al., 2024). As linker length is crucial to heterobifunctional design, MrTAC compounds linking GSK3326595 to JQ1 were synthesized with varying linker lengths with polyethylene glycol (PEG) linkers of 1 or 3 units (MrTAC-1 and -2). Cells were treated with MrTAC dose curves for 24 hours and BRD4 levels were assessed by immunoblotting. No significant changes in BRD4 protein levels were observed upon MrTAC treatment (**Figure 2.8A**). Similar results were observed using MrTACs to recruit PRMT5 to cytoplasmic FKBP12^{F36V}-tagged fusion proteins via AP1867 ligands where MrTAC-3 and -4 treatment had no effect on the levels of AXIN1-FKBP12^{F36V} (**Figure 2.8B**). These data suggest that recruitment of PRMT5 with the inhibitor GSK3326595 impedes MrTAC degrader activity.

We next evaluated degradation of MrTACs using endogenous recruiters of PRMT3, a Type I PRMT that performs asymmetric dimethylation. We utilized the small molecule SGC707, which binds tightly to PRMT3 with a K_D of 53 nM and has high selectivity over other Type I PRMTs, including PRMT1 (Kaniskan et al., 2018; Siarheyeva et al., 2012). MrTACs were synthesized with PEG linker lengths of 2 or 3 units and with a chloroalkane ligand recruiter of fusion proteins (MrTAC-5 and -6) (**Figure 2.5A**). Protein levels of GSK3β, a validated MrTAC target protein (Seabrook et al., 2024), were evaluated following a 24-hour incubation. Relative to control treatments, GSK3β levels were most reduced at the 0.1 μM dose of MrTAC-5 with a DC_{50} of 2.0 nM. Notably, the shortest PEG length with MrTAC-5 led to the strongest level of degradation with

a D_{MAX} of 50%. PRMT3 protein levels were consistent across MrTAC treatments (**Figure 2.8C**). As expected, MrTAC degradation was disrupted in the absence of methyltransferase activity using a catalytically dead PRMT3 (**Figure 2.8D**). Degradation could also be achieved using MrTAC-5 in HeLa cervical cancer cells or U87 glioblastoma cells expressing a HaloTagged GSK3β (**Figure 2.5B**). MrTAC degradation was rescued by pharmacological inhibition of either lysosomal activity or methyltransferase activity using bafilomycin and AdOx, respectively (**Figure 2.5C-D**). Molecular modeling suggests that following ternary complex formation, the release of PRMT3 from its allosteric binder could position the target protein near the PRMT3 active site for proximity-induced methylation (**Figure 2.5E**). Global proteomics were performed on cells treated with MrTAC-5, which showed high levels of Halo- GSK3β degradation (**Figure 2.5F**). Additional changes were observed in the levels of several GSK3β substrates in support of the role of GSK3β as a master regulator of cellular activity. These data indicate that MrTAC retains degrader activity when using the allosteric PRMT3 recruiter SGC707.

Group-Transfer MrTACs for Endogenous PRMT Recruitment

To this point, our data shows variable degradation efficiency when using inhibitors to recruit the PRMT, depending on the inhibitor moiety used for PRMT recruitment. Thus, a generalizable approach that could repurpose all PRMT inhibitors would accelerate the development of MrTAC degraders. Recent studies show that inhibitors can be used for silent enzyme recruitment, as seen in the case of kinases for phosphorylation-inducing chimeras (PHICS), employing group-transfer chemistry in a process referred to as inhibitor-directed group-transfer (Pergu et al., 2023; Reddi et al., 2021; Matsuo et al., 2018; Tsou et al., 2001; Ward et al., 2013; Zhuang et al., 2020; Reddi et al., 2021; Choudhary, 2021). Here, bifunctional molecules are synthesized with a cysteine- or

lysine-reactive group placed between the enzyme inhibitor and the linker. Once the inhibitor binds the enzyme active site, a covalent bond is formed between the reactive group and a neighboring lysine or cysteine. Covalent binding to the linker results in elimination of the inhibitor, thereby preserving native enzyme activity (**Figure 2.6A**). Given the prevalence of active site PRMT inhibitors, we sought to assess whether inhibitors could be transformed into silent PRMT recruiters for MrTAC degradation by group-transfer chemistry.

Recruitment of PRMT5 with GSK3326595 was not sufficient for MrTAC degradation (**Figure 2.8A-B**). Thus, we explored whether GSK3326595 could be used to recruit active PRMT5 via an inhibitor-directed group-transfer approach. PRMT5 has an exposed cysteine near the GSK3326595 exit vector site (C487), which suggests that GSK3326595 could be modified for group-transfer chemistry. Molecular docking of PRMT5 with a modified GSK3326595 probe showed that this C487 is angled optimally for PRMT5 labeling (**Figure 2.6A**). Recent work identified the optimal leaving groups to mediate inhibitor elimination when using group-transfer chimeras[ref]. Cysteine-reactive methacrylamides and lysine-reactive N-acyl-N-alkyl phenylsulfonamides (NASA) can be readily applied for an inhibitor elimination strategy through the addition of leaving groups (spacers) that allow for inhibitor elimination, with modifications that allow for improved stability, size, and scalability. To identify the optimal chemistry to enable selective PRMT5 recruitment, PRMT5 labeling was compared between alkyne-modified GSK3326595 probes bearing different group-transfer warheads (cysteine-reactive methacrylamide or lysine-reactive *N*-(2,2,2-trifluoroethyl) sulfonamide) with different spacer lengths between GSK3326595 and the warhead (**Figure 2.6B**). In vitro, PRMT5 labeling was observed with both the methacrylamide- and sulfonamide-based probes, where the cysteine-reactive methacrylamide

showed high selectivity for PRMT5 labeling (**Figure 2.6B**). Increased spacer length between the methacrylamide and GSK3326595 allowed for more efficient PRMT labeling using Compound 2, which was nominated as the lead PRMT5 probe. We confirmed that Compound 2 could similarly label PRMT5 within HEK293 cells (**Figure 2.6B**). Efficient in-cell PRMT5 labeling using Compound 2 demonstrates potential for using active site group-transfer chemistry to enable MrTAC degraders.

We next tested whether the modified PRMT5 probe could be used for TPD in a series of MrTACs. To determine whether group-transfer chemistry could be used for MrTAC degraders, we synthesized group-transfer MrTACs to bind $FKBP12^{F36V}$-tagged proteins. We nominated AXIN1 as an initial target given its strong degradation in the SNAP library (**Figure 2.3**) and links to human disease (Wang et al., 2021). MrTACs using GSK3326595 did not degrade AXIN1-$FKBP12^{F36V}$ with either MrTAC-3 or MrTAC-4 treatment (**Figure 2.8B**). In contrast, modifying this scaffold for group-transfer chemistry resulted in significant reduction of AXIN1-$FKBP12^{F36V}$ levels over a 24 hour treatment with MrTAC-7 (**Figure 2.6C**). As expected, PRMT5 protein levels were consistent across all cell conditions. These data highlight the utility of group-transfer chemistry for the development of endogenous MrTAC degraders.

To extend these analyses, we next evaluated the utility of the modified PRMT5 probe for the development of fully endogenous MrTACs. To generate an endogenous series of MrTACs, we appended Compound 2 to JQ1 with varying PEG linkers (PEG-1, -3, and -4) (**Figure 2.6D**). BRD4 protein levels were evaluated by immunoblotting after 24-hour treatment with 1 or 10 μM MrTAC. Strikingly, MrTACs reduced BRD4 protein levels across all linker lengths (**Figure 2.6D**). The

shortest PEG1 linker (MrTAC-8) demonstrated the highest potency with strong degradation at 1 μM and was nominated for lead compound verification across a wider range of doses. Dose response curves were performed with MrTAC-8 over 24 hours in HEK293 cells, cervical cancer HeLa cells, and glioblastoma U87 cells (**Figure 2.6E**). MrTAC-8 potently degraded BRD4 with 93% D_{MAX} and a DC_{50} of 46 nM in HeLa cells. Similarly, MrTAC-8 degraded BRD4 in U87 cells with a D_{MAX} of 79% and a DC_{50} of 67 nM. HEK293 cell treatments with MrTAC-8 elicited similar levels of degradation with a D_{MAX} of 82% but was slightly less potent with a DC_{50} of 4.8 μM. Degradation in all three cell lines contrast the results of the initial MrTAC compounds (MrTAC-1 and -2) that lack the methacrylamide for group-transfer chemistry, which were unable to induce degradation of BRD4 due to retention of the PRMT5 inhibitor in the final ternary complex (**Figure 2.8A**). Similarly, degradation was not observed when treating cells with either warhead of the group transfer MrTACs and requires PRMT5 and BRD4 to interact (**Figure 2.9A**). Across MrTAC treatment, PRMT5 levels were unaffected (**Figure 2.9B**). Untargeted proteomics revealed that MrTAC degradation was highly selective towards bromodomain-containing proteins in cells treated with MrTAC-8 relative to control treatments of either warhead (**Figure 2.6F**). We confirmed that MrTAC induces methylation of endogenous BRD4 by immunoprecipitating methylated proteins with an antibody against symmetric dimethylarginine. In response to a 2 hour treatment with MrTAC-8, BRD4 migrated from the unmethylated fraction to methylated fraction, demonstrating induced target methylation (**Figure 2.6G**). We performed additional validation to confirm the requirement of induced methylation for target degradation and found that overexpressing a catalytically dead PRMT5 blocked MrTAC degradation of BRD4 (**Figure 2.6H**). Consistent with prior MrTAC results, BRD4 degradation could be rescued by inhibition of

lysosomes using bafilomycin and chloroquine (**Figure 2.6I**). These data demonstrate that MrTAC degrades endogenous BRD4 in multiple cell types in a methylation-dependent manner.

BRD4 binds acetylated chromatin in cancer to promote oncogenic growth programs. As such, we evaluated HeLa cell proliferation over 72 hour treatments with MrTAC-8 or with MrTAC-1, which lacks the cysteine-reactive methyacrylamide. A significant reduction in cell proliferation was observed in HeLa cells treated with MrTAC-8 at 100 nM, compared to DMSO-treated cells (**Figure 2.6J**). Cell treatments with the control MrTAC-1 compound had only a minimal effect on cell growth, even at the highest dose of 10 μM, which was presumably due to the inhibitory effects of either warhead within MrTAC-1. To model the 3-dimensional tumor environment, we evaluated the effects of MrTAC treatment on cancer growth in spheroid cultures. Over a 5 day treatment, MrTAC dramatically suppressed the growth of cervical cancer spheroids derived from HeLa cells using 1 μM MrTAC-8 (**Figure 2.6K**). Spheroids treated with the MrTAC-1 control compound could not elicit this effect, highlighting that the anti-oncogenic effects of MrTAC are a direct consequence of targeted BRD4 degradation. Treating spheroids with the either warhead of MrTAC-8 (Cmp 2 and JQ1) also had no effect on spheroid growth, indicating that targeted degradation by MrTAC provides a more potent anti-cancer response than the parental inhibitor. Similar anti-proliferative phenotypes were observed in both 2-D and 3-D glioblastoma culture models using U87 cells (**Figure 2.9C**). The present work highlights the potential of connecting fundamental degron biology to targeted protein degradation platforms for the ultimate goal of expanding protein degradability. By leveraging the generalizability of PRMTs for targeted degradation, these data enable the first series of fully endogenous MrTAC degraders.

2.4 Discussion

Hijacking proteasome-targeting degrons enables precise control of protein turnover (Li and Crews, 2022). An analogous post-translational modification for the lysosomal degradation is lacking, which has limited development of lysosome-targeting degraders. Thus, the potential of targeted proteolysis to revolutionize therapeutics has yet to be realized (Schneider et al., 2021). The present work was motivated by the need to identify exploitable degron pathways. We catalogued the methyl-degrome, an endogenous lysosomal degron, and evaluate how native properties of this degron translate into a chemically induced setting. Mechanistic analyses identified the molecular properties of protein degradability across diverse target substrates in chemically induced contexts. Exploration of the MrTAC mechanism revealed that all three classes of PRMT enzymes can be recruited for MrTAC degradation beyond PRMT1. Insights from these studies enabled the development of a series of endogenous MrTAC degraders that recruit different PRMT-substrate pairs. Together, these findings provide a foundation to streamline target prioritization in degrader development and establish a precedent for future MrTAC clinical applications.

Proteostasis is essential for development, homeostasis, and disease, and continues to inspire the discovery of new degron families. However, the size, dynamics, and complexity of the human proteome suggests that the complete repertoire of degrons is incompletely defined. We show that methylarginine degron modifications underlie a conserved eukaryotic proteolytic pathway that regulates diverse cellular processes. Previous studies show individual protein substrates that undergo methylarginine degron modification for lysosomal proteolysis. Here, proteomic mapping of a lysosomal degron uncovered the utility of methylarginine degron for endogenous proteolysis across substrates with a range of sizes, subcellular localization, and activities. Lessons learned

from the endogenous methylarginine degron pathway were translated into mechanistic dissection of MrTAC, a chemically-inducible cellular system.

Effective target selection is a crucial step in a successful targeted protein degradation campaign. Studies using pan-binding PROTACs that simultaneously engage hundreds of proteins have revealed that compatibility with PROTACs can vary greatly from one protein to another (Bondeson et al., 2018; Donovan et al., 2020). While ternary complex formation is crucial for PROTAC degradation, target-E3 interaction does not guarantee degradation and can be affected by intrinsic protein features such as basal protein half-life, subcellular distribution, and protein synthesis rates (Donovan et al., 2020). Several reports offer predictive modeling and machine learning strategies to effectively prioritize 'likely degradable' proteins for PROTACs (Schneider et al., 2021; Zhang et al., 2022; Li et al., 2022) but these strategies remain largely unexplored for alternative degrader technologies beyond PROTAC. Thus, a remaining challenge is the inability to predict which protein should be targeted by different degrader modalities. The present work focuses on lysosomal proteolysis and provides a new lens for understanding degradability of specific protein families. Defining the underlying requirements for methylarginine degron addition via endogenous or chemically-induced approaches establishes a new framework to predict whether the strategy for target degradation should harness proteasomal or lysosomal approaches.

The advent of degrader technologies is highlighted by a continually emerging line of novel small-molecule approaches such as deubiquitination, acetylation, phosphorylation, and O-GlcNAcylation (Liu and Ciulli, 2023). However, there is a need for silent recruiters that bind enzymes without impairing activity. Proof-of-concept MrTAC studies relied on a genetically modified PRMT1 for ligand recruitment (Seabrook et al., 2024). In this work, we show that

repurposed PRMT inhibitors can be used for PRMT recruitment through a catch-and-release mechanism, but this success depended on the ligand being used. This complements the research from Gray & Crabtree (Sarott et al., 2024), who found that it is challenging to predict which inhibitors can be effectively used for catch-and-release of enzymes. We demonstrate that this challenge can be overcome through group-transfer chemistry, which was shown previously using phosphorylation-inducing chimeras (PHICs), where inhibitors could be used to recruit active kinases through inhibitor-directed group-transfer (Pergu et al., 2023; Reddi et al., 2021; Vedagopuram et al., 2025). Leveraging this chemistry, we converted the PRMT5 inhibitor, GSK3326595, into a silent PRMT5 recruiter by installing a cysteine-reactive methacrylamide that covalently labels PRMT5 and eliminates GSK3326595 following binding. This chemistry led to a series of fully endogenous MrTACs that align with the hallmarks of modern degraders, including high potency and on-target degradation. This approach provides a valuable resource for other proximity-driven post-translational modification approaches and opens MrTAC as an entirely new, clinically viable modality. Future endeavors will focus on assessing whether this chemical strategy can be applied using other inhibitors to recruit additional PRMTs.

2.5 Methods

Antibodies

Antibodies used for immunoblots and immunofluorescence include anti-SNAP-tag (New England Biolabs, P9310), anti-FLAG (Cell Signaling Technology, 2368), anti-GSK3β (Cell Signaling Technology, 9832), anti-Actin (Sigma-Aldrich, A1978), anti-LAMP-1 (D2D11; Cell Signaling Technology, 9091), anti-H3 (96C10; Cell Signaling Technology, 3638), anti-PRMT3 (E9R7B; Cell Signaling Technology, 72593) anti-BRD4 (ThermoFisher, A-700-004), anti-SDMA (Cell Signaling Technology, 13222), anti-PRMT1 (Cell Signaling Technology, 2449). Antibodies were

used at 1:300 dilutions for immunofluorescence. Antibodies were used at either 1:1,000 (Actin, H3, BRD4, PRMT3) or 1:2,000 (SNAP-tag, GSK3β, FLAG, PRMT1) for immunoblotting.

Plasmids

Plasmids encoding the SNAP-tag library were obtained as either full SNAP-tagged constructs (TOMM20 Addgene 197496, NUP43 Addgene 98276, Rab5b Addgene 169069, YTHDF1 Addgene 155346) or as genes (AXIN1 Addgene 109370, AXIN2 Addgene 82099, SMAD7 Addgene 11733, PFK-1 SinoBiological HG14133-ANG, CAMKK2 Addgene 170577, HDAC6 Addgene 13823, cMyc Addgene 101135) that were cloned into the previously described SNAP-GSK3β-Flag plasmid by Gibson Assembly. Plasmids encoding the Halo-PRMT library were generated by obtaining PRMT open-reading frames from either Addgene (PRMT4 81118, PRMT7 34693) or IDT (PRMT5) and were cloned into the previously described Halo-PRMT1-Myc construct by Gibson Assembly. Generation of the catalytically dead (E444Q) PRMT5 was performed using the KLD kit. Catalytically dead (E338Q) PRMT3 was obtained from Addgene (164696). Fkbp12F36V-AXIN1 was generated by replacing the SNAP-tag gene in the CMV-SNAP-AXIN1 construct with the $Fkbp12^{F36V}$ gene by Gibson Assembly (Addgene 91793). For plasmids generated by Gibson Assembly, primers (all obtained from IDT) were designed to amplify the target gene with overlapping homology to the corresponding plasmid, which was digested by restriction enzymes for gene insertion as per manufacturer instructions.

Cell culture

Cells were obtained from the American Type Culture Collection (ATCC). Cells were cultured in DMEM (HEk293, HeLa) or EMEM (U87) supplemented with 10% heat-inactivated FBS (Gibco),

1% penicillin–streptomycin, 0.25 mg /mL plasmocin (InvivoGen; ant-mpp) and 1% glutamine. The cells were maintained at 37 °C and 5% CO2. Media was replenished every 2–3 days and passaged with 0.25% trypsin when cells reached ~75% confluency. Cells were routinely tested with the MycoStrip Mycoplasma Detection Kit (InvivoGen; rep-mys). HEK293T cells stably expressing HA-tagged TMEM192-RFP were a generous gift from Dr. Roberto Zoncu (UC Berkeley). Stable HEK293 cell lines expressing wild-type or catalytically dead (92-VLD/AAA-95) PRMT1–HaloTag were generated by plasmid transfection and selection for 2 weeks in 500 µg/mL G418 as previously described (Seabrook et al., 2024). Cells were maintained in 0.5x selection media.

For MrTAC^{HaXS8} treatments, cells were seeded into 12 wells at 60-70% density. The next day, cells were transfected with DNA using Lipofectamine-2000 as per manufacturer instructions. For SNAP library experiments, 500 ng SNAP-target DNA was transfected into HEK293 cells stably expressing Halo-PRMT1. For Halo library experiments, 500 ng SNAP-GSK3β DNA and 500 ng Halo-PRMT DNA was transfected into HEK293 cells. 24 hours after transfected, cells were treated with 1 µM MrTAC^{HaXS8} (MedChemExpress, HY-131015) for 24 hours before lysis by scraping and boiling in 2x Laemmli buffer (4% SDS, 20% glycerol, 120 mM Tris–HCl (pH 6.8) and 0.02% bromophenol blue with 10 mM fresh dithiothreitol (DTT)). For MrTAC treatments against Halo-GSK3β, HEK293, HeLa, or U87 cells were seeded into 12 wells at 50-60% density and the next day cells were transfected with 0.5-1 µg of plasmid DNA. After overnight transfection, cells were treated with compounds at the indicated times and concentrations before lysis and boiling in 2x Laemmli buffer with DTT. For MrTAC treatments against BRD4, HEK293 or HeLa cells were seeded into 12 wells at 60-70% density. The following day, cells were dosed with MrTAC at

indicated timeframes and concentrations with matched concentrations of DMSO before lysis by scraping and boiling in RIPA buffer (25 mM Tris pH 7.6, 150 mM NaCl, 1% NP-40, 1% sodium deoxycholate, 0.1% SDS) and 2x Laemmli sample buffer.

Proliferation assays

To evaluate cell proliferation during MrTAC treatment, HeLa or U87 cells were first plated in 12 wells at 40% confluence. The following day, cells were treated with DMSO or variable amounts (0.1, 1 or 10 μM) of MrTAC-1 or MrTAC-8. Media was replenished daily. 72 hours later, representative images of cells were acquired and total cell count per well was determined using a Countess 2 Automated Cell Counter. For spheroid culture, HeLa or U87 cells were seeded into Sphera Ultra Low Attachment U-Bottom plates (ThermoFisher 174929) at $1x10^4$ cells per well. After 48 hours of spheroid formation, cells were dosed daily with 1 μM of respective drug and brightfield images were captured on day 5. Cross-sectional spheroid area was quantified for each condition with 6 spheroid technical replicates per condition.

Immunoblotting

Lysates were loaded on a 10% SDS–PAGE gel and transferred onto nitrocellulose membranes at 10 V for 90-120 min. Membranes were then blocked in milk and probed overnight with primary antibodies at the above dilutions. Membranes were washed in PBS and incubated for 1 hour in secondary antibody (Invitrogen, 61-6520) or rabbit 1:20,000 (Prometheus, 20-303) before imaging using enhanced chemiluminescence (ECL) (Sigma-Aldrich, WBLUR0100). Images were acquired using an iBright FL750 and bands were quantified using ImageJ software with normalization to the loading control and the DMSO control sample.

Immunofluorescence

Cells were plated and grown on poly-L-lysine coated glass coverslips (Newcomer Supply, 1339A). After treatment, cells were washed twice in PBS and fixed for 15 minutes in 4% paraformaldehyde (PFA). Cells were washed 2x for 5 min in PBS, permeabilized in 0.2% Triton X-100 for 10 min, washed 2x for 5 min in PBS and blocked in 0.5% bovine serum albumin (BSA) for 30 min before an overnight incubation in primary antibody. The following day, coverslips were washed 3x for 7 min in PBS, incubated in secondary antibody at 1:1,500 (goat anti-rabbit Alexa Fluor 488 Invitrogen A-11008, goat anti-mouse Alexa Fluor 568 Invitrogen A-11004) for 40 minutes, washed 5x for 5 min in PBS and mounted onto glass slides with ProLong Gold antifade reagent with 4′,6-diamidino-2-phenylindole (DAPI) (Thermo Fisher Scientific, P36931).

Immunoprecipitation of methylated proteins

HeLa cells were seeded in 10 cm dishes at 60% confluence and were pre-treated with 500 nM Bafilomycin and 5 μM MG132 before a 2 hour incubation with either DMSO or 1 μM MrTAC-8. Cells were then washed with TBS and lysed in 500 uL lysis buffer (25 mM Tris pH 7.4, 150 mM NaCl, 1 mM EDTA, 1% NP40, 5% glycerol with 100 μM IOX1 and Roche cOmplete EDTA-free protease inhibitor cocktail tab). Lysates rested on ice for 10 minutes before centrifugation at 16,000 rcf for 10 minutes at 4°C. Antibody detecting SDMA-modified proteins (Cell Signaling Technology, 13222) was then added with 5 μg antibody per lysate and incubated overnight at 4°C on a rotator. The next day, a total lysate sample was collected before addition of 25 μg pre-equilibrated Pierce Protein A/G Beads (Thermofisher, 88802, equilibrated 4x with TBS) and rotation for 1 hour at room temperature. Beads were collected on a magnetic rack before 2x washes

in TBS and were eluted in 2x Laemmli buffer at room temperature for 10 minutes. Immunoprecipitated samples were then analyzed by immunoblotting.

Lysosomal immunoprecipitation mass spectrometry

HEK293T cells stably expressing 3xHA-tagged TMEM192-RFP were used to immunoprecipitated lysosomes, as previously described (cells were a generous gift from Dr. Roberto Zoncu) (Franco et al., 2023). Cells were grown to 90% confluency in 10 cm dishes and pre-treated with 5 μM IWP-2 (MilliporeSigma, I0536) for 4 hours before treatment with Wnt3a ligands (PeproTech, 315-20) diluted 1:1000 in L cell (catalog no. CRL-2648) media for 20 min with one 10 cm dish per condition. Lysosome-inhibited samples were pre-treated with 400 nM Bafilomycin (Cayman Chemical, 11038) for 4 hours, which continued through treatments. Following treatments, cells were washed and scraped with PBS, clarified by centrifugation, and resuspended in KPBS buffer [136 mM KCl, 10 mM KH_2PO_4, 0.5 mM tris(2-carboxyethyl)phosphine (TCEP), and Opti-Prep protease inhibitor cocktail, (pH 7.25)] and lysed with 23G syringes followed by another round of centrifugation to remove nuclei. The post-nuclear supernatant (PNS) was incubated with PBS-equilibrated anti-HA beads (Thermo Fisher Scientific, 88836) and rotated at 4°C for 2 hours. The anti-HA beads were placed on magnetic racks and were washed in KBPS buffer five times for 5 min rotating at 4°C. Next, 0.1% NP-40 in PBS was added to the samples, which were then incubated at 30 °C for 30 minutes. The supernatant was collected after magnetic separation, and the elution was repeated two more times for a total of three rounds. Samples were reduced in 5 mM dithiothreitol (DTT) at room temperature for 30 min, alkylated in 20 mM iodoacetamide at room temperature for 30 min and centrifuged. Cell pellets were washed twice with 4 volumes of ice-cold methanol and centrifuged. After air-drying, the pellets were

digested with 1% LysC in 8 M urea prepared in 50 mM ammonium bicarbonate for 4 hours at 37 °C. Peptides were further digested in 0.5 µg trypsin overnight at 37 °C. The following day, samples were acidified with 0.1% TFA and desalted using SepPak C18 cartridges (Waters, WAT054955). Columns were washed with 0.1% TFA followed by 0.5% acetic acid, and peptides were eluted with 50% acetonitrile. Eluates were dried by SpeedVac and subjected to mass spectrometry analysis.

Global proteomics mass spectrometry

For proteomic analysis of PRMT3 MrTACs, HEK293 cells were seeded in 6-well plates with $8x10^5$ cells per well and were transfected with 1 µg Halo-GSK3β as described above. The following day, cells were treated for 24 hours with either MrTAC-5 (0.1 µM) or DMSO control. Cell pellets were then snap frozen in liquid nitrogen and stored at -80°C before downstream processing. For proteomic analysis of PRMT5 MrTACs, HEK293 cells were seeded in 6-well plates with $8x10^5$ cells per well and were treated for 24 hours with either MrTAC-8 (1 µM) or a combination of either warhead (Cmp 2 and JQ1, both 1 µM). Cell pellets were then snap frozen in liquid nitrogen and stored at -80°C before downstream processing.

Cell pellets were suspended in RIPA buffer (Cell Signaling Technology) containing protease inhibitor cocktail (cOmplete™ Protease Inhibitor Cocktail, Roche). The suspension was sonicated at 4 °C for 10 min, followed by centrifugation at 16,000 g for 10 min at 4 °C. The supernatant was collected and digested by the filter-aided sample preparation (FASP) method. Briefly, the supernatant was transferred into a spin filter column (10 kDa cutoff). Proteins were reduced with 10 mM DTT for 1 hr at 56 °C, and alkylated with 20 mM iodoacetic acid for 30 min at room

temperature in the dark. Next, the buffer was exchanged with 50 mM NH_4HCO_3 by washing the membrane three times. Free trypsin was added into the protein solution at a Trypsin to protein ratio of 1:50 and incubated overnight at 37 °C. The tryptic digests were recovered in the supernatant after centrifugation, and an additional wash with water. The combined supernatants were vacuum-dried and then adjusted to 200 µL with 0.5% acetic acid. The peptide mixture was then subjected to C18 solid-phase extraction (The Nest Group, Inc.) for desalting.

Proteomics data were acquired via LC-MS/MS using an UltiMate 3000 UHPLC (Thermo Fisher Scientific), coupled in-line with an Orbitrap Fusion Lumos mass spectrometer (Thermo Fisher Scientific) with an ESI nanospray source. Mobile phase A was composed of 0.1% formic acid (FA) in water, and Mobile phase B was composed of 0.1% formic acid (FA) in ACN. The total flow rate was 300 nL min^{-1}, and peptides were separated over a 57 min gradient from 4% to 25% buffer B (total run time 90 min per sample) on an Acclaim PepMap RSLC column (50cm x 75 µm). Survey (MS) scans were acquired in Orbitrap (FT) with automated gain control (AGC) target 8E5, maximum injection time 50 msec, and dynamic exclusion of 30 sec across the scan range of 375-1800 m/z. MS/MS spectra were acquired in data-dependent acquisition mode at top speed for 3 sec per cycle; the AGC target was set to 1E4 with maximum injection time of 35 msec. Ions were subjected to stepped-energy higher-energy collision dissociation (seHCD) fragmentation at a normalized collision energy (NCE) of 20±5 %.

The raw LC-MS/MS data files were analyzed using MaxQuant (version 2.6.3.0), with the spectra searched against the Uniprot mouse database (updated on May 21st, 2018). For identification of the peptides, the mass tolerances were 20 ppm for initial precursor ions, and 0.5 Da for fragment

ions. Two missed cleavages in tryptic digests were allowed. Cysteine residues were set as static modifications. Oxidation of methionine was set as the variable modification. Filtering for the peptide identification was set at a 1% false discovery rate (FDR). GSK3B substrates were annotated based on Taelman et al., 2010. P-values calculated by Two-sided Unpaired T-test.

Protein purification

PRMT5 was purified from BL21 DE3 *E. coli* expressing AviTag-GST-His-PRMT5-FLAG. Cells were grown at 37°C before inoculation at OD 0.6-0.8 with 0.5 mM IPTG and were subsequently grown at 16°C for 18 hours. Cell pellets were frozen at -20°C before lysis in 20 mM NaH_2PO_4 pH 7.6, 300 mM NaCl, 1 mM DTT, 5 mM EDTA, 1% Triton X-100, 200 µg/mL lysozyme, and freshly prepared 1 mM PMSF, 5 µM AEBSF, and 25 U/mL Pierce Universal Nuclease. Lysates rested on ice for 30 minutes before sonication for 6 minutes total sonication time in 30 second intervals on ice. Lysates were then clarified by centrifugation at 16,000 rcf for 20 minutes at 4°C and the supernatant was then filtered. Soluble protein was loaded onto an EconoFit Profinity GST column and separated at 4°C as per manufacturer instructions. GST-tagged protein was washed using lysis buffer before elution over a 0-100% gradient in 100 mM Tris pH 8, 5 mM EDTA, 20 mM and reduced glutathione. Eluate was analyzed by SDS-PAGE and PRMT5-containing fractions were combined and buffer exchanged into storage buffer (50 mM Tris pH 7.5, 100 mM NaCl, 1 mM DTT) before storage at -80°C.

Molecular modeling

Consurf modeling was performed as previously described[18] using default settings. Molecular modeling of PRMT3 (PDB: 4RYL) with MrTAC-5 and HaloTag (PDB: 6U32) was modeled based

on reference positions of protein-ligand co-crystals. Molecular docking of Compound 2 with PRMT5 (PDB code 9MGL) was performed using Autodock Vina in PyMOL using GSK3326595 as a reference ligand to position Compound 2, free energy binding scores are described in the figure legend.

Click labeling

Purified PRMT5 labeling was performed using Compounds 1-3, where 2 µM GST-PRMT5 was incubated with 2 µM of each probe for 2 hours at room temperature. Click reaction was then performed in a total volume of 30 µL using 5 µM sulfoCy5.5 azide (Lumiprobe), 5.5 µM tris(3hydroxypropyltriazolylmethyl)amine (THPTA) (Combiblocks), 1.1 µM CuSO4, and 16.7 µM sodium ascorbate. After a 30 minute incubation at room temperature, 7 uL of 4x laemmli sample reducing buffer was added, and samples were heated at 100°C for 5 minutes. Prepared sample was resolved on NuPAGE 4-12% Bis-Tris gels (ThermoFisher, NP0321BOX) with MOPS SDS running buffer (ThermoFisher, NP0001) at 200V for 1 hour. Labeled protein was detected using sulfo-cy5-azide using the Li-COR Odyssey infrared (IR) fluorescent imaging system.

In-cell PRMT5 labeling was performed using Compound 2 in HEK293 cells. Cells were seeded at $1x10^6$ cells/well in a 6-well plate. The following day, cells were treated with Compound 2 at 1 or 10 µM or with DMSO for 2 hours. Cells were washed 2x with 1mL PBS before lysis in 300 uL RIPA with Roche cOmplete EDTA-free protease inhibitor cocktail. Lysates incubated on ice for 10 minutes before centrifugation at 16,000rcf for 10 minutes at 4°C. Next, 100 µg lysate was incubated with 50 µM biotin azide (Vector Laboratories, #CCT-1265), 50 µM 4-[[bis[[1-(1,1-dimethylethyl)-1H-1,2,3-triazol-4-yl]methyl]amino]methyl]-1H-1,2,3-triazole-1-acetic acid

(BTTAA) (Vector Laboratories, CCT-1236), 500 µM $CuSO_4$, 500 µM tris(2-carboxyethyl)phosphine (TCEP) in a final volume of 100 µL. Samples reacted for 30 minutes at room temperature before adding 33 uL of 4x Laemmli with DTT and boiling for 5 minutes at 95°C. Samples were loaded onto a 6% gel and transferred onto a nitrocellulose membrane as described above before probing with HRP-conjugated streptavidin (Cell Signaling Technologies, #3999) at 1:500. Chemiluminescent signal was detected as described above.

Bioinformatic analyses

The LysoIP-MS data were analyzed using multiple bioinformatic tools. Gene Ontology (GO) Analysis, which includes biological process, cellular compartment, and molecular function analyses, were performed using Pan-GO software (Feuermann et al., 2025). As indicated, the LysoIP-MS samples were analyzed either as the total methylarginine degron-activated pool, just the methylated subset, or just the unmethylated subset. Methylation status was evaluated based on Maron et al., 2021 which aggregates their arginine methylomics with prior reports of arginine methylomics. For the purposes of this analysis, the methylation status was compared as a binary assessment of either no methylation or 1 or more sites of arginine methylation. Protein size was calculated using data available from UniProtKB based on the canonical isoform of each protein (The Uniprot Consortium, 2025). Protein disorder was predicted using DisordEred PredIction CenTER2 (DEPICTER2) with the computational tool fIDPnn using non-standardized disorder scores (Hu et al., 2021). Protein turnover data were sourced from Schneider et al., 2021, which summarize half-life data obtained by Mathieson et al., 2018 across four cell lines. The fastest recorded turnover time (hours) across the four cell lines was used for this study. Proteins with undetectably fast turnover were denoted as having a half-life 0.5 hours.

The SNAP-tagged libraries were analyzed separately depending on the variable tested. Disorder was approximated using PondR (Xue et al., 2010) based on the average disorder across all residues. Surface-exposed arginine count was determined based on Consurf modeling as previously described (Franco et al., 2023). The localization was scored according to Uniprot characterization of protein localization where cytosolic or nuclear proteins were scored as favorable (100% in heatmap) and other proteins were scored as less favorable (membrane- or organelle-bound or phase separated, 66.67% in heatmap) (The Uniprot Consortium, 2025). Native methylation status and turnover were mapped as described above. Ligandability analysis was performed using Cansair software where each score was calculated across druggability categories. Existence of PROTAC/degraders were cross-checked using PROTAC databases, Pubmed, and BiorXiv (Weng et al., 2023). Binary scoring systems are presented separately from spectral scoring systems. Expression profiles of each gene was sourced from The Cancer Genome Atlas (TCGA) and plotted on a log2(TPM+1) scale where proteins were segregated based on patterns and levels of expression (Cerami et al., 2012).

Chemical synthesis of PRMT3 MrTACs

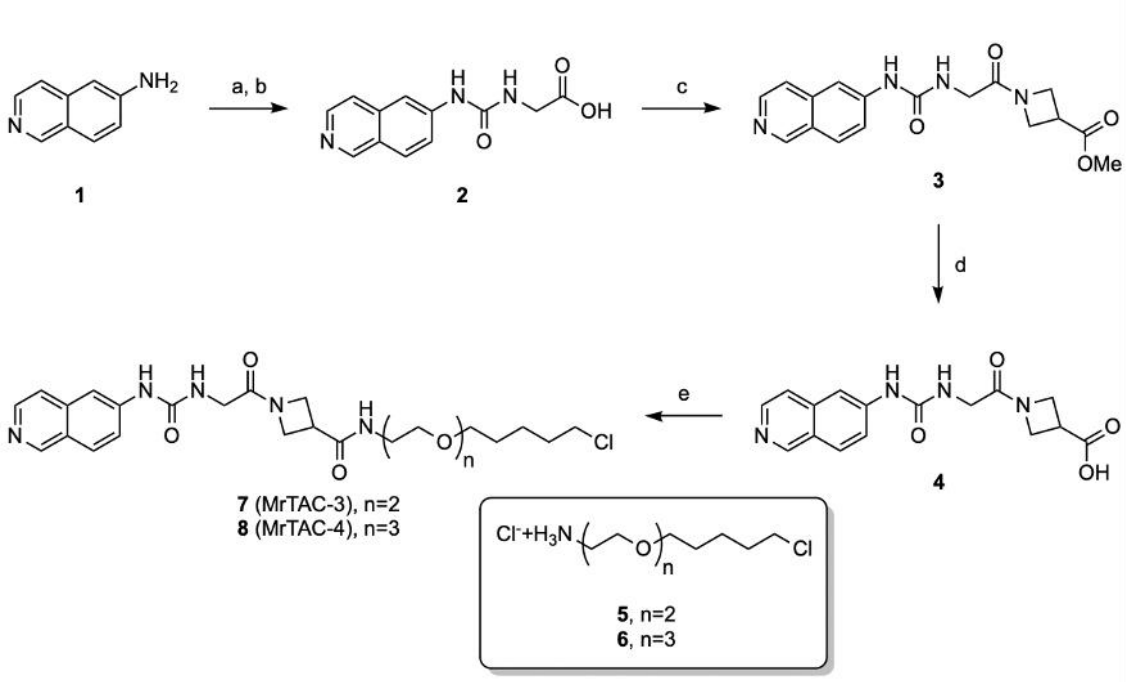

Reagents and solvents used were of commercially available reagent grade quality from Fisher Scientific, ThermoFisher, VWR, TCI, Apollo Scientific or Ambeed, and were used without further purification, unless stated. All reactions requiring anhydrous conditions were carried out under an argon atmosphere in a flame-dried flask. Concentration under reduced pressure was performed at 40 °C using a Buchi™ rotary evaporator. Brine refers to a saturated aqueous solution of NaCl. Petroleum ether refers to the fraction of light petroleum ether boiling in the range 40–60 °C. ^{1}H NMR spectra were measured on a Bruker Avance III HD 500 (500 MHz) in the stated solvent. Chemical shifts (δ_H) are quoted in parts per million (ppm) relative to tetramethylsilane (δ_H = 0.00 ppm). Spectra are calibrated using residual protic solvent peaks with the data provided by Fulmer *et al.* were processed using MestReNova 14.2.2 or Bruker Topspin 4.4.0 software (Fulmer et al., 2010). ^{1}H NMR spectra are reported as follows: chemical shift (multiplicity [s (singlet); d (doublet); t (triplet); q (quartet); p (pentet); sext (sextet); hept (heptet); m (multiplet) or combinations thereof], coupling constants *J* (to the nearest 0.1 Hz, with identical coupling

constants averaged), number of protons, assignment). ^{13}C NMR spectra were measured on a Bruker Avance III HD 500 (126 MHz). Chemical shifts (δ_C) are quoted in parts per million (ppm) relative to tetramethylsilane (δ_C = 0.00 ppm). The spectra are calibrated using the solvent peak with the data provided by Fulmer *et al*. NMR data were processed using MestReNova 14.2.2 or Bruker Topspin 4.4.0 software. The multiplicity of signals is singlet unless otherwise stated. Mass spectra were acquired from solutions of methanol or acetonitrile using Shimadzu LCMS 2020 (low resolution), or Waters LCT Premier (high resolution) using electrospray ionization (ESI), or a Thermo DART-Orbitrap (high resolution) using direct analysis in real-time (DART) ionization. *m/z* values are reported in Daltons and followed by their percentage abundance in parentheses. Melting points were determined using a Griffin capillary tube melting point apparatus and are uncorrected. The solvent(s) from which the sample was crystallized is given in parentheses. Infrared (IR) spectra were obtained from thin films or neat samples, using a diamond ATR module. The spectra were recorded on a Cary 630 FTIR Spectrometer. Absorption maxima ($\tilde{\nu}_{max}$) are reported in wavenumbers (cm^{-1}). Semi-preparative high performance liquid chromatography (HPLC) was carried out using a Shimadzu using either a HPLC Shimadzu shim-pack GIS C18 column [5 µm, 250 mm × 10 mm], with isocratic elution, at 20 mL min^{-1} or Shimadzu shim-pack GIS C18 column [5 µm, 250 mm × 20 mm], with isocratic elution at 40 mL min^{-1}. Analytical high performance liquid chromatography (HPLC) was performed using a Shimadzu system with a shim-pack Velox C18 column [5 µm, 100 mm × 4.6 mm] reverse phase column]; [95:5 water: acetonitrile → 5:95 water: acetonitrile with 0.1% formic acid, 1 min hold; 10 min 95-5% H_2O; 5 min hold; 1 mL min^{-1}]. Sample purity was measured using the UV absorbance at the indicated wavelengths. Analytical thin-layer chromatography (TLC) was carried out on normal phase Merck silica gel 60 F254 aluminum-supported thin layer chromatography sheets. Visualization was

carried out by absorption of UV light (λ_{max} 254 nm) or thermal development after staining with a basic aqueous solution of $KMnO_4$. UV light was provided by a lamp (UVA, 365 nm, P = 0.2 × 60 W). Normal phase flash silica gel column chromatography was carried out manually using SiliaFlash Irregular Silica Gel P60, 40 - 63 μm, 60 Å, eluting with solvents as supplied, under a positive pressure of compressed air. Characterization of novel material can be found online via doi: 10.1016/j.chempr.2026.102998.

(Isoquinolin-6-ylcarbamoyl)glycine: Based on the procedure of Kaniskan *et al.*, To 6-aminoisoquinoline (3.00 g, 20.8 mmol, 1.0 eq) in CH_2Cl_2 (125 mL), was added ethyl isocyanatoacetate (2.81 mL, 25 mmol, 1.2 eq.) and the resulting mixture was stirred for 16 h at room temperature, at which time HPLC showed complete consumption of starting material (Kaniskan et al., 2015). Volatile components were removed *in vacuo,* yielding the desired crude ethyl ester (5.63 g, 99%) as pale-yellow solid which was used without further purification. LRMS *m/z* (ESI^+) 274.15 ($[M+H]^+$ 100%). A portion of this material (3.00 g, 11.0 mmol, 1.0 eq) was then dissolved in THF (10 mL) and H_2O (5 mL), and LiOH (526 mg, 22.0 mmol, 2.0 eq) was added. The reaction mixture was stirred for 16 h at room temperature, until complete consumption of the starting material was confirmed by LCMS analysis. The mixture was concentrated *in vacuo* to remove THF, and the pH of the remaining aqueous solution was adjusted to approximately 6–7 by the addition of 1 M aqueous HCl, causing the desired compound to precipitate. The resulting solid was collected by filtration, and the filter cake was dried under vacuum at 40 °C overnight, yielding isoquinolin-6-ylcarbamoyl)glycine as an off-white solid (1.97 g, 73%): m.p. >220 °C (dec., from H_2O); $\bar{\boldsymbol{\nu}}_{max}$ (solid)/cm^{-1} 3356, 1675, 1499, 1400, 1364, 818; ^1H NMR (500 MHz, D_6-DMSO) δ_H 12.68 (s, 1H), 9.30 (s, 1H), 9.11 (s, 1H), 8.37 (s, 1H), 8.09 (d, J = 2.1 Hz, 1H), 7.98 (d, J = 8.9 Hz,

1H), 7.65 (s, 1H), 7.55 (dd, J = 8.9, 2.1 Hz, 1H), 6.60 (t, J = 5.7 Hz, 1H), 3.84 (d, J = 5.7 Hz, 2H); ^{13}C NMR (126 MHz, D_6-DMSO) δ_C 172.0, 155.0, 151.4, 143.1, 142.0, 136.5, 128.5, 124.2*, 120.5, 119.7, 110.1, 41.4. (*observed by HMBC analysis); LRMS *m/z* (ESI^+) 246.15 ($[M+H]^+$, 100%); HRMS *m/z* ($DART^-$) [Found: $[M-H]^-$ 244.0729, $C_{12}H_{10}N_3O_3$ requires M^-, 244.0728]. HPLC retention time 2.04 min, 254 nm (98.5%), 220 nm, (99.0%), 310 nm (98.7%).

Methyl 1-[(isoquinolin-6-ylcarbamoyl)glycyl]azetidine-3-carboxylate: Based on the procedure of Zou *et al.*, to a solution of (isoquinolin-6-ylcarbamoyl)glycine (1.40 g, 5.71 mmol, 1.0 eq) in DMF (19 mL) was added DIPEA (3.98 mL, 22.8 mmol, 4.0 eq) (Zou et al., 2024). Once the solid had fully dissolved, HATU (2.39 g, 6.28 mmol, 1.1 eq) was added, and the reaction mixture was stirred for 15 min. After this time, methyl azetidine-3-carboxylate hydrochloride (1.04 g, 6.85 mmol, 1.2 eq) was added to the reaction mixture, which was allowed to stir for 16 h, after which, LCMS confirmed the reaction was complete. The reaction was then quenched by the addition of distilled H_2O (100 mL), and extracted with CH_2Cl_2 (3 × 100 mL). The combined organic extracts were dried over Na_2SO_4, filtered, and concentrated *in vacuo*. The resulting residue, which contained a small amount of DMF, was purified immediately using silica gel column chromatography eluting with a gradient of 0–15% MeOH in CH_2Cl_2, yielding methyl 1-[(isoquinolin-6-ylcarbamoyl)glycyl]azetidine-3-carboxylate as a brown amorphous solid (2.12 g, 75%): R_f 0.32 (10% MeOH in CH_2Cl_2); $\bar{\nu}_{max}$ (solid)/cm^{-1} 2954, 1729, 1622, 1436, 1398, 1202, 1167, 839, 826; ^{1}H NMR (500 MHz, MeOD) δ_H 8.98 (s, 1H), 8.24 (d, J = 5.8 Hz, 1H), 8.02 (d, J = 2.1 Hz, 1H), 7.91 (d, J = 8.9 Hz, 1H), 7.58 (d, J = 5.8 Hz, 1H), 7.52 (dd, J = 8.9, 2.1 Hz, 1H), 4.49 (dd J = 9.0, 9.0 Hz, 1H), 4.42 (dd, J = 9.0, 6.0 Hz, 1H), 4.24 (dd, J = 9.7, 9.7 Hz, 1H), 4.15 (dd, J = 9.7, 6.0 Hz, 1H), 3.91 (d, J = 16.9 Hz, 1H), 3.87 (d, J = 16.9 Hz, 1H), 3.75 (s, 3H), 3.62 – 3.55 (m,

1H); ^{13}C NMR (126 MHz, MeOD) δ_C 174.2, 171.5, 157.4, 151.9, 143.7, 142.4, 138.8, 129.9, 126.1*, 122.4, 121.8, 112.5, 53.6, 52.86[#], 52.85[#], 52.1, 40.8, 33.6 (*observed by HMBC, [#]diastereotopic carbon); LRMS *m/z* (ESI^+) 343.20 ($[M+H]^+$, 100%); HRMS *m/z* ($DART^+$) [Found: $[M+H]^+$ 343.1392, $C_{17}H_{19}N_4O_4$ requires M^+, 343.1401]. HPLC retention time 3.69 min, 254 nm (89.3%), 220 nm, (90.2%), 310 nm (89.3%).

1-[(Isoquinolin-6-ylcarbamoyl)glycyl]azetidine-3-carboxylic acid: Based on the procedure of Zou *et al.*[3], to methyl 1-((isoquinolin-6-ylcarbamoyl)glycyl)azetidine-3-carboxylate (877 mg, 2.56 mmol, 1.0 eq) in THF (3.20 mL) and DMF (1.07 mL), was added aqueous NaOH (2 M, 1.66 mL, 3.33 mmol, 1.3 eq). The reaction mixture was stirred at room temperature for 16 h until the reaction was completed as judged by LCMS. The reaction was then quenched by the addition of aqueous HCl (1 M, 3.33 mL), and the volatile components were removed *in vacuo*. The remaining residue was purified using multiple injections on to a reverse phase isocratic preparative HPLC column, which eluted with 20% MeCN in water, with 0.1% formic acid. Subsequent lyophilization yielded 1-[(isoquinolin-6-ylcarbamoyl)glycyl]azetidine-3-carboxylic acid as a colorless fluffy powder (500 mg, 56%): $\bar{\nu}_{max}$ (solid)/cm^{-1} 1701, 1629, 1545, 1472, 1400, 1221, 1155, 883, 829; ^{1}H NMR (500 MHz, D_6-DMSO) δ_H 9.54 (s, 1H), 9.08 (s, 1H), 8.34 (d, J = 5.8 Hz, 1H), 8.08 (d, J = 2.1 Hz, 1H), 7.97 (d, J = 8.9 Hz, 1H), 7.62 (d, J = 5.8 Hz, 1H), 7.55 (dd, J = 8.9, 2.1 Hz, 1H), 6.80 (t, J = 5.2 Hz, 1H), 4.32 (dd, J = 8.6, 8.6 Hz, 1H), 4.24 (dd, J = 8.6, 6.0 Hz, 1H), 4.03 (dd, J = 9.3, 9.3 Hz, 1H), 3.92 (dd, J = 9.3, 6.0 Hz, 1H), 3.77 (d, J = 5.2 Hz, 2H), 3.40 – 3.28 (m, 1H); ^{13}C NMR (126 MHz, D_6-DMSO) δ_C 174.2, 168.9, 154.9, 151.4, 143.1, 142.1, 136.5, 128.5, 124.2, 120.4, 119.7, 109.9, 52.3, 50.8, 45.5, 32.7; LRMS *m/z* (ESI^+) 329.20 ($[M+H]^+$ 100%); HRMS *m/z*

(DART$^-$) [Found: $[M-H]^-$ 327.1100, $C_{16}H_{15}N_4O_4$ requires M^+, 327.1099]; HPLC Retention time = 3.15 min, 254 nm (93.4%), 220 nm, (94.8%), 310 nm (93.3%).

N-(2-(2-((6-Chlorohexyl)oxy)ethoxy)ethyl)-1-((isoquinolin-6-ylcarbamoyl)glycyl)azetidine-3-carboxamide (MrTAC-3): 1-[(Isoquinolin-6-ylcarbamoyl)glycyl]azetidine-3-carboxylic acid (26.0 mg, 79 μmol, 1.0 eq.) was dissolved in DMF (400 μL), and to this was added DIPEA (41 μL, 0.24 mmol, 3.0 eq), followed by HATU (45 mg, 0.12 mmol, 1.5 eq), and the reaction mixture stirred for 15 mins. 2-(2-((6-Chlorohexyl)oxy)ethoxy)ethanamine hydrochloride (31 mg, 0.12 mmol, 1.5 eq) was gently warmed so that it was liquid, and using a pipette, the linker was added to the solution, and the reaction was allowed to proceed for 16 h, after which time LCMS analysis confirmed the reaction had gone to completion. The reaction mixture was then acidified by the addition of two drops of formic acid and purified using a reverse phase isocratic preparative HPLC column with an eluent of 25% MeCN in H_2O with 0.1% formic acid. The resulting product was lyophilized to give *N*-(2-(2-((6-chlorohexyl)oxy)ethoxy)ethyl)-1-((isoquinolin-6-ylcarbamoyl)glycyl)azetidine-3-carboxamide as an off-white hygroscopic powder (21 mg, 50%): $\bar{\nu}_{max}$ (thin film)/cm^{-1} 2935, 2863, 1635, 1550, 1457, 1227, 1094, 882, 828; ^{1}H NMR (500 MHz, MeOD) δ_H 9.05 (s, 1H), 8.30 (d, *J* = 5.9 Hz, 1H), 8.11 (d, *J* = 2.1 Hz, 1H), 8.00 (d, *J* = 8.9 Hz, 1H), 7.68 (d, *J* = 5.9 Hz, 1H), 7.60 (dd, *J* = 8.9, 2.1 Hz, 1H), 4.45 (dd, *J* = 8.7, 8.7 Hz, 1H), 4.38 (dd, *J* = 8.7, 5.9 Hz, 1H), 4.19 (dd, *J* = 9.5 Hz, 1H), 4.11 (dd, *J* = 9.5, 5.9 Hz, 1H), 3.94 (d, *J* = 16.8 Hz, 1H), 3.86 (d, *J* = 16.8 Hz, 1H), 3.62 – 3.54 (m, 8H), 3.51 – 3.45 (m, 3H), 3.41 (t, *J* = 5.4 Hz, 2H), 1.80 – 1.73 (m, 2H), 1.63 – 1.56 (m, 2H), 1.51 – 1.43 (m, 2H), 1.43 – 1.35 (m, 2H); ^{13}C NMR (126 MHz, MeOD) δ_C 174.1, 171.3, 157.4, 152.0, 143.8, 142.6, 139.0, 130.0, 126.3, 122.4, 121.9, 112.6, 72.2, 71.3, 71.2, 70.4, 53.7, 52.2, 45.7, 40.8, 40.6, 34.5, 33.8, 30.5, 27.7, 26.5; LRMS

m/z (ESI^+) 534.30 ($[M+H]^+$ 100%); HRMS *m/z* (ESI^+) [Found: $[M+H]^+$ 534.2482, $C_{26}H_{37}ClN_5O_5$ requires M^+, 534.2484]; HPLC retention time 5.40 min, 254 nm (97.8%), 220 nm, (96.0%), 310 nm (98.0%).

N-(2-(2-(2-((6-Chlorohexyl)oxy)ethoxy)ethoxy)ethyl)-1-((isoquinolin-6-ylcarbamoyl)glycyl)azetidine-3-carboxamide (MrTAC-4): 1-[(Isoquinolin-6-ylcarbamoyl)glycyl]azetidine-3-carboxylic acid (21 mg, 64 µmol, 1.0 eq) was dissolved in DMF (320 µL), and to this was added DIPEA (45 µL, 0.26 mmol, 4.0 eq), followed by HATU (27 mg, 70 µmol, 1.1 eq), and the reaction mixture was allowed to stir for 15 mins. 2-(2-(2-((6-Chlorohexyl)oxy)ethoxy)ethoxy)ethan-1-amine hydrochloride (23 mg, 77 µmol, 1.2 eq) was gently warmed so that it was liquid, and using a pipette, the linker was added to the solution, and the reaction was allowed to proceed for 16 h, after which time LCMS analysis confirmed the reaction had gone to completion. The reaction mixture was then acidified by addition of two drops of formic acid and purified using a reverse phase isocratic preparative HPLC column with an eluent of 25% MeCN in H_2O with 0.1% formic acid. Following lyophilization, the compound was redissolved in MeCN and treated with macroporous triethylammonium methylpolystyrene carbonate resin for 2 h. The resin was then removed, and the solution lyophilized to give *N*-(2-(2-(2-((6-chlorohexyl)oxy)ethoxy)ethoxy)ethyl)-1-((isoquinolin-6-ylcarbamoyl)glycyl)azetidine-3-carboxamide as an off-white hygroscopic powder (11 mg, 30%): $\bar{\nu}_{max}$ (thin film)/cm^{-1} 2933, 2865, 1636, 1551, 1457, 1227, 1096, 882, 828; ^1H NMR (500 MHz, MeOD) δ_H 9.03 (d, *J* = 0.9 Hz, 1H), 8.29 (d, *J* = 5.9 Hz, 1H), 8.10 (d, *J* = 2.1 Hz, 1H), 7.98 (d, *J* = 8.9 Hz, 1H), 7.65 (d, *J* = 6.1 Hz, 1H), 7.58 (dd, *J* = 8.9, 2.1 Hz, 1H), 4.44 (dd, *J* = 8.7, 8.7 Hz, 1H), 4.38 (dd, *J* = 8.7, 5.9 Hz, 1H), 4.19 (dd, *J* = 9.5, 9.5 Hz, 1H), 4.11 (dd, *J* = 9.5, 5.9 Hz, 1H), 3.94 (d, *J* = 16.9 Hz, 1H), 3.86 (d, *J*

= 16.9 Hz, 1H), 3.68 – 3.52 (m, 12H), 3.51 – 3.46 (m, 3H), 3.41 (t, *J* = 5.4 Hz, 2H), 1.79 – 1.71 (m, 2H), 1.63 – 1.54 (m, 2H), 1.50 – 1.42 (m, 2H), 1.42 – 1.34 (m, 2H); ^{13}C NMR (126 MHz, MeOD) δ_C 174.1, 171.3, 157.5, 152.2, 143.6, 143.0, 138.9, 129.9, 126.3, 122.3, 121.8, 112.6, 72.2, 71.60, 71.58, 71.3, 71.1, 70.4, 53.7, 52.2, 45.70, 45.68, 40.2, 40.6, 34.5, 33.8, 30.6, 27.74, 27.72, 26.5; LRMS *m/z* (ESI^+) 578.35 ($[M+H]^+$ 100%); HRMS *m/z* (ESI^+) [Found: $[M+H]^+$ 578.2745, $C_{28}H_{41}ClN_5O_6$ requires M^+, 578.2745]; HPLC retention time 5.44 min, 254 nm (97.7%), 220 nm, (97.7%), 310 nm (97.3%).

Chemical Synthesis of PRMT5 MrTACs

For chemical synthesis, all building blocks and reagents were purchased and used as received from commercial sources without further purification or characterization. Reactions were performed in round-bottom flasks or vials (depending on scale) and stirred with Teflon®-coated magnetic stir bars. Normal phase separations were performed using flash column chromatography on silica gel (60 Å mesh, 20–40 μm) on a Teledyne Isco CombiFlash Rf system. Reverse phase HPLC purifications were performed on Teledyne ISCO ACCQPrep™ HP150 equipped with an XBridge BEH Prep Column (19 mm x 250 mm). Reactions and compound purity were monitored using UPLC-MS on a Waters ACQUITY UPLC I-Class 15 PLUS system with an ACQUITY SQ Detector 2. Nuclear magnetic resonance (NMR) spectra were collected on a Bruker AVANCE III HD 400 MHz spectrometer at room temperature (1H NMR, 400 MHz; 13C, 101 MHz). 1H and 13C chemical shifts are indicated in parts per million (ppm) and internally referenced to residual solvent signals. NMR solvents were purchased from Cambridge Isotope Laboratories, Inc., and NMR data were obtained in CDCl3, CD3OD, and DMSO-d6 using non-deuterated traces as reference. Data for 1H NMR are reported as follows: chemical shift value in ppm, multiplicity (s

= singlet, br s = broad singlet, d = doublet, t = triplet, dd = doublet of doublets, and m = multiplet), integration value, and coupling constant value in Hz. High-resolution mass spectra were recorded on a Thermo Q Exactive Plus mass spectrometer system equipped with a HESI-II electrospray ionization source at Harvard Center for Mass Spectrometry at the Harvard FAS Division of Science Core Facility. Characterization of novel material can be found online via doi: 10.1016/j.chempr.2026.102998.

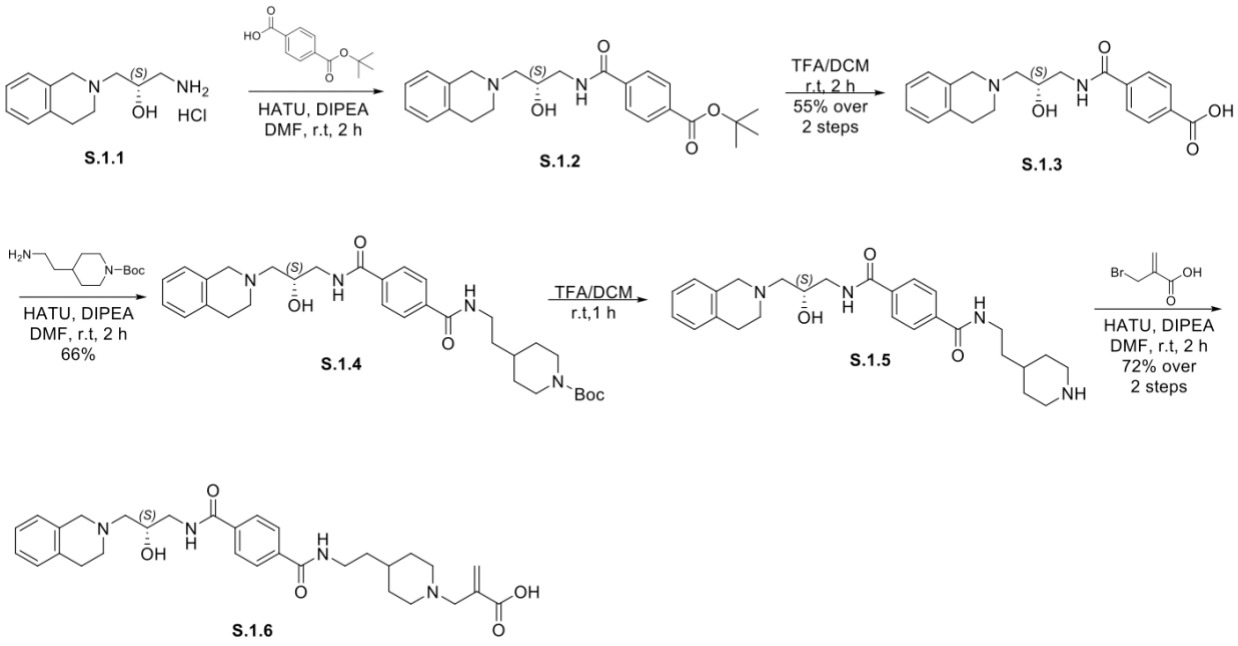

tert-butyl (S)-4-((3-(3,4-dihydroisoquinolin-2(1H)-yl)-2-hydroxypropyl)carbamoyl)benzoate: To a stirred solution of (S)-1-amino-3-(3,4-dihydroisoquinolin-2(1H)-yl)propan-2-ol (1 mmol, 242 mg) in DMF (3 mL) at r.t., were added HATU (1.5 equiv.) and DIPEA (3 equiv.). Product formation was monitored by LC-MS. Upon reaction completion the resulting mixture was stirred at r.t. for 2 h, after which it was diluted with EtOAc and saturated aqueous $NaHCO_3$. The organic layer was collected and concentrated under reduced pressure. The resulting crude mixture was

purified through silica gel chromatography using a gradient of DCM/MeOH (0->50% MeOH) and then used for the next step without further characterization.

(S)-4-((3-(3,4-dihydroisoquinolin-2(1H)-yl)-2-hydroxypropyl)carbamoyl)benzoic acid: To a stirred solution of tert-butyl (S)-4-((3-(3,4-dihydroisoquinolin-2(1H)-yl)-2-hydroxypropyl)carbamoyl)benzoate (1 mmol, obtained from the previous step) in DCM (2 mL), TFA (2 mL) was added. The resulting mixture was stirred at r.t. for 2 h, after which volatiles were removed under reduced pressure. The crude mixture was then purified by reverse phase prep HPLC using a gradient of water/MeCN (5-100% MeCN), providing 196 mg pure acid (55% over 2 steps). ^{1}H NMR (400 MHz, DMSO) δ 8.68 (t, *J* = 5.5 Hz, 1H), 7.98 – 7.86 (m, 4H), 7.17 – 7.01 (m, 4H), 3.97 (p, *J* = 6.0 Hz, 1H), 3.77 – 3.64 (m, 2H), 3.45 (dt, *J* = 13.2, 5.4 Hz, 1H), 3.28 (dt, *J* = 12.9, 6.1 Hz, 1H), 2.88 – 2.73 (m, 4H), 2.66 – 2.52 (m, 3H). ^{13}C NMR (101 MHz, DMSO) δ 167.4, 166.2, 163.8, 138.6, 135.0, 134.4, 133.9, 129.6, 128.9, 127.8, 126.9, 126.5, 126.0, 67.0, 62.7, 56.3, 51.5, 45.4, 40.9, 28.9.

N1-(2-(2-(2-((S)-4-(4-chlorophenyl)-2,3,9-trimethyl-6H-thieno[3,2-f][1,2,4]triazolo[4,3-a][1,4]diazepin-6-yl)acetamido)ethoxy)ethyl)-N4-((S)-3-(3,4-dihydroisoquinolin-2(1H)-yl)-2-hydroxypropyl)terephthalamide (MrTAC-1): To a stirred solution of (S)-4-((3-(3,4-dihydroisoquinolin-2(1H)-yl)-2-hydroxypropyl)carbamoyl)benzoic acid (22 mg, 0.06 mmol) in DMSO (0.3 mL) were added HATU (1.5 equiv.), DIPEA (5 equiv.) and (*S*)-JQ1-PEG1-NH2 (HCl salt) (1.1 equiv,). The resulting mixture was stirred at r.t. for 1 h after which it was diluted with DMSO and purified on reverse phase HPLC using water/MeCN (+0.1 Formic acid) as eluent, providing 14 mg (28% yield) of pure compound. ^{1}H NMR (400 MHz, MeOD) δ 7.90 – 7.77 (m,

4H), 7.42 (q, *J* = 8.7 Hz, 4H), 7.30 – 7.11 (m, 4H), 4.60 (dd, *J* = 9.3, 5.0 Hz, 1H), 4.28 (s, 3H), 3.75 – 3.36 (m, 13H), 3.30 – 3.05 (m, 5H), 2.70 (s, 3H), 2.44 (s, 3H), 1.67 (s, 3H). ^{13}C NMR (101 MHz, MeOD) δ 171.6, 168.3, 167.9, 164.8, 155.5, 150.9, 137.0, 136.7, 136.6, 136.4, 132.1, 131.8, 131.7, 130.6, 130.5, 130.0, 129.6, 128.4, 128.4, 127.4, 127.2, 127.1, 126.4, 126.4, 69.1, 68.9, 65.3, 59.6, 54.3, 53.8, 50.4, 44.2, 39.6, 39.0, 37.5, 25.8, 13.0, 11.5, 10.3.

N1-(1-((S)-4-(4-chlorophenyl)-2,3,9-trimethyl-6H-thieno[3,2-f][1,2,4]triazolo[4,3-a][1,4]diazepin-6-yl)-2-oxo-6,9,12-trioxa-3-azatetradecan-14-yl)-N4-((S)-3-(3,4-dihydroisoquinolin-2(1H)-yl)-2-hydroxypropyl)terephthalamide (MrTAC-2): This compound was synthesized as described above for the PEG1 derivative at 30 mg scale, providing 17 mg of pure compound. ^{1}H NMR (400 MHz, MeOD) δ 7.76 – 7.67 (m, 4H), 7.37 – 7.24 (m, 4H), 7.08 – 6.86 (m, 4H), 4.51 (dd, *J* = 8.8, 5.3 Hz, 1H), 4.03 (h, *J* = 5.5 Hz, 1H), 3.71 (s, 2H), 3.61 – 3.16 (m, 20H), 2.82 (d, *J* = 3.0 Hz, 4H), 2.70 – 2.59 (m, 2H), 2.57 (s, 3H), 2.32 (s, 3H), 1.57 (s, 3H). ^{13}C NMR (101 MHz, MeOD) δ 171.5, 168.0, 167.9, 164.7, 155.6, 150.7, 137.0, 136.8, 136.7, 136.5, 133.4, 133.3, 132.1, 131.8, 130.6, 130.6, 130.0, 128.4, 128.3, 127.1, 127.1, 126.3, 126.2, 125.6, 70.2, 69.9, 69.2, 69.1, 66.6, 61.8, 55.8, 53.8, 51.2, 44.8, 39.7, 39.1, 37.4, 27.9, 13.0, 11.6, 10.2.

tert-butyl (S)-4-(2-(4-((3-(3,4-dihydroisoquinolin-2(1H)-yl)-2-hydroxypropyl)carbamoyl)benzamido)ethyl) piperidine-1-carboxylate: To a stirred solution of (S)-4-((3-(3,4-dihydroisoquinolin-2(1H)-yl)-2-hydroxypropyl)carbamoyl)benzoic acid (200 mg, 0.56 mmol) in DMF (2 mL) at r.t, were added HATU (1.5 equiv.) and DIPEA (3 equiv.). Product formation was monitored by LC-MS. Upon reaction completion the resulting mixture was stirred a r.t for 2 h, after which it was diluted with

EtOAc and saturated aqueous $NaHCO_3$. The organic layer was collected and concentrated under reduced pressure. The resulting crude mixture was purified on silica gel chromatography using a gradient of DCM/MeOH (0->50% MeOH) as eluent, providing pure N-boc product (210 mg, 66% yield). ^{1}H NMR (400 MHz, MeOD) δ 7.86 (q, *J* = 8.6 Hz, 4H), 7.23 – 7.04 (m, 4H), 4.24 – 4.13 (m, 1H), 4.08 (dt, *J* = 13.3, 2.9 Hz, 2H), 3.92 (s, 2H), 3.69 – 3.42 (m, 4H), 3.09 – 2.95 (m, 4H), 2.81 (ddd, *J* = 22.5, 13.2, 7.2 Hz, 4H), 1.83 – 1.75 (m, 2H), 1.60 (dd, *J* = 7.4, 4.4 Hz, 3H), 1.47 (s, 9H), 1.21 – 1.04 (m, 2H). ^{13}C NMR (101 MHz, MeOD) δ 168.1, 167.8, 155.1, 137.2, 136.7, 133.1, 132.8, 128.3, 127.1, 127.0, 126.4, 126.2, 125.7, 79.5, 66.4, 61.5, 55.6, 51.1, 44.8, 39.0, 37.1, 35.7, 33.5, 31.8, 27.6, 27.3.

(S)-N1-(3-(3,4-dihydroisoquinolin-2(1H)-yl)-2-hydroxypropyl)-N4-(2-(piperidin-4-yl)ethyl)terephthalamide: To a stirred solution of tert-butyl (S)-4-(2-(4-((3-(3,4-dihydroisoquinolin-2(1H)-yl)-2-hydroxypropyl)carbamoyl)benzamido)ethyl)piperidine-1-carboxylate (200 mg, 0.35 mmol) in DCM (1.5 mL), TFA (0.5 mL) was added. The resulting mixture was stirred at r.t. for 1 h after which volatiles were removed under reduced pressure. The crude mixture was used for the next step without further characterization.

(S)-2-((4-(2-(4-((3-(3,4-dihydroisoquinolin-2(1H)-yl)-2-hydroxypropyl)carbamoyl)benzamido)ethyl)piperidin-1-yl)methyl)acrylic acid (Formate salt): To a stirred solution of (S)-N1-(3-(3,4-dihydroisoquinolin-2(1H)-yl)-2-hydroxypropyl)-N4-(2-(piperidin-4-yl)ethyl)terephthalamide (obtained from the previous step), in DMF (1.5 mL) at r.t were added 2-(bromomethyl)acrylic acid (1 equiv.) and DIPEA (3 equiv.). The resulting mixture was stirred at r.t. for 1 h. Then the crude mixture was diluted with DMSO and purified on reverse

phase prep HPLC using water/MeCN as eluent, providing 139 mg of pure product (72% yield). ^{1}H NMR (400 MHz, MeOD) δ 8.45 (s, 1H), 7.91 (q, *J* = 8.3 Hz, 4H), 7.31 – 7.12 (m, 4H), 6.25 (d, *J* = 1.5 Hz, 1H), 5.72 (s, 1H), 4.38 (d, *J* = 21.2 Hz, 3H), 3.85 (s, 2H), 3.64 – 3.09 (m, 12H), 2.93 (t, *J* = 12.2 Hz, 2H), 2.02 (d, *J* = 14.1 Hz, 2H), 1.71 – 1.57 (m, 3H), 1.48 (q, *J* = 13.6 Hz, 2H). ^{13}C NMR (101 MHz, MeOD) δ 171.1, 168.3, 167.9, 167.8, 137.2, 136.7, 135.5, 131.3, 128.7, 128.5, 127.9, 127.7, 127.3, 127.1, 126.6, 126.5, 65.0, 59.1, 53.7, 51.6, 50.2, 44.0, 36.9, 34.8, 31.3, 29.0, 25.2.

To a stirred solution of (S)-2-((4-(2-(4-((3-(3,4-dihydroisoquinolin-2(1H)-yl)-2-hydroxypropyl)carbamoyl)benzamido)ethyl)piperidin-1-yl)methyl)acrylic acid in DMF (2 ml/mmol) were added HATU (1.5 equiv.), DIPEA (5 equiv.) and the corresponding alkyne amine. The resulting mixture was stirred at r.t. for 1 h after which it was diluted with DMSO and purified on preparative reverse phase HPLC using water/MeCN (+ 0.1% formic acid), providing pure compounds.

(S)-N1-(2-(1-(2-(but-3-yn-1-ylcarbamoyl)allyl)piperidin-4-yl)ethyl)-N4-(3-(3,4-dihydroisoquinolin-2(1H)-yl)-2-hydroxypropyl)terephthalamide (Cmp 1): Synthesized at 0.01 mmol scale (35% yield). ^{1}H NMR (400 MHz, MeOD) δ 7.90 (q, *J* = 8.3 Hz, 4H), 7.23 (qd, *J* = 9.2, 4.3 Hz, 3H), 7.15 (d, *J* = 7.3 Hz, 1H), 6.16 (s, 1H), 5.75 (s, 1H), 4.26 (d, *J* = 21.1 Hz, 3H), 3.74 – 3.02 (m, 16H), 2.46 (tt, *J* = 6.7, 3.8 Hz, 4H), 2.37 (t, *J* = 2.6 Hz, 1H), 1.95 (d, *J* = 13.2 Hz, 2H), 1.72 – 1.35 (m, 5H). ^{13}C NMR (101 MHz, MeOD) δ 168.4, 167.9, 167.8, 137.2, 136.6, 136.2, 131.9, 130.0, 128.4, 127.3, 127.2, 127.1, 126.4, 126.3, 126.2, 81.0, 69.7, 65.4, 59.9, 59.4, 54.5, 52.5, 50.5, 44.3, 39.0, 37.1, 35.2, 32.1, 30.3, 26.1, 18.3.

(S)-4-(6-(2-(but-3-yn-1-ylcarbamoyl)allyl)-2,6-diazaspiro[3.3]heptane-2-carbonyl)-N-(3-(3,4-dihydroisoquinolin-2(1H)-yl)-2-hydroxypropyl)benzamide (Cmp 2): Synthesized at 0.01 mmol scale (27% yield). ^{1}H NMR (400 MHz, MeOD) δ 7.86 – 7.79 (m, 2H), 7.61 (d, *J* = 7.9 Hz, 2H), 7.19 (dt, *J* = 12.7, 7.3 Hz, 3H), 7.10 (d, *J* = 7.6 Hz, 1H), 6.07 (s, 1H), 5.92 (s, 1H), 4.58 – 4.15 (m, 11H), 3.91 (d, *J* = 10.1 Hz, 2H), 3.80 – 3.72 (m, 1H), 3.52 – 3.02 (m, 9H), 2.34 (d, *J* = 7.7 Hz, 2H), 2.20 (s, 1H). ^{13}C NMR (101 MHz, MeOD) δ 169.6, 168.6, 167.0, 136.3, 133.6, 130.7, 128.5, 128.5, 128.1, 127.7, 127.3, 126.9, 80.7, 69.5, 62.6, 56.4, 52.1, 51.5, 43.8, 39.0, 38.3, 32.9, 24.6, 18.2.

(S)-N1-(3-(3,4-dihydroisoquinolin-2(1H)-yl)-2-hydroxypropyl)-N4-(4-(N-(hex-5-ynoyl)-N-(2,2,2-trifluoroethyl)sulfamoyl)butyl)terephthalamide (Cmp 3): Synthesized at 0.01 mmol scale (58% yield).^{1}H NMR (400 MHz, Acetone) δ 8.35 (t, *J* = 6.0 Hz, 1H), 7.98 (s, 4H), 7.39 – 7.18 (m, 4H), 4.88 – 4.70 (m, 2H), 4.67 – 4.53 (m, 2H), 3.92 (t, *J* = 6.5 Hz, 2H), 3.79 – 3.46 (m, 6H), 3.44 – 3.23 (m, 3H), 3.01 (td, *J* = 7.4, 4.0 Hz, 2H), 2.43 (td, *J* = 2.7, 0.7 Hz, 1H), 2.37 – 2.26 (m, 2H), 2.07 (p, *J* = 2.2 Hz, 4H), 2.02 – 1.75 (m, 6H).^{13}C NMR (101 MHz, Acetone) δ 173.6, 172.8, 167.8, 165.9, 165.7, 165.7, 137.7, 136.1, 136.0, 131.2, 128.8, 128.1, 128.1, 127.4, 127.2, 127.2, 127.0, 126.8, 125.4, 124.7, 122.6, 122.0, 83.2, 82.7, 70.0, 65.5, 63.7, 63.0, 62.6, 58.6, 54.3, 54.0, 50.8, 48.9, 45.6, 45.3, 43.8, 43.7, 38.8, 38.7, 38.5, 38.3, 34.3, 32.1, 28.0, 25.0, 24.7, 23.6, 20.9, 20.4, 17.5, 17.0.

To a stirred solution of (S)-2-((4-(2-(4-((3-(3,4-dihydroisoquinolin-2(1H)-yl)-2-hydroxypropyl)carbamoyl)benzamido)ethyl)piperidin-1-yl)methyl)acrylic acid in DMSO (2

ml/mmol) were added HATU (1.5 equiv.), DIPEA (5 equiv.) and (*S*)-JQ1-PEGn-NH2 (HCl salt) (1.1 equiv.). The resulting mixture was stirred at r.t. for 1 h after which it was diluted with DMSO and purified on preparative reverse phase HPLC using water/MeCN (+ 0.1% formic acid), providing pure compounds. *Note: Although we successfully obtained the desired products using (S)-JQ1-PEGn-NH2 (HCl salt) or (S)-JQ1-PEGn-NH2 (formate salt), we were unable to obtain the desired compounds with (S)-JQ1-PEGn-NH2 (TFA salt).*

N1-(2-(1-(2-((2-(2-(2-((S)-4-(4-chlorophenyl)-2,3,9-trimethyl-6H-thieno[3,2-f][1,2,4]triazolo[4,3-a][1,4]diazepin-6-yl)acetamido)ethoxy)ethyl)carbamoyl)allyl)piperidin-4-yl)ethyl)-N4-((S)-3-(3,4-dihydroisoquinolin-2(1H)-yl)-2-hydroxypropyl)terephthalamide (formate salt) (MrTAC-8): Synthesized at 0.01 mmol scale (41% yield). ^{1}H NMR (400 MHz, MeOD) δ 7.90 – 7.78 (m, 4H), 7.51 – 7.36 (m, 4H), 7.23 – 7.12 (m, 3H), 7.07 (dd, *J* = 6.4, 2.6 Hz, 1H), 6.12 (d, *J* = 1.4 Hz, 1H), 5.56 (s, 1H), 4.60 (dd, *J* = 8.8, 5.3 Hz, 1H), 4.20 (dp, *J* = 10.6, 5.3 Hz, 1H), 3.96 (s, 2H), 3.68 – 3.27 (m, 16H), 3.09 (t, *J* = 6.0 Hz, 2H), 3.00 (q, *J* = 7.1 Hz, 4H), 2.87 (qd, *J* = 13.0, 6.2 Hz, 2H), 2.69 (s, 3H), 2.43 (s, 3H), 2.15 (t, *J* = 11.4 Hz, 2H), 1.83 (t, *J* = 9.6 Hz, 2H), 1.67 (s, 3H), 1.58 (q, *J* = 7.0 Hz, 2H), 1.49 – 1.26 (m, 3H). ^{13}C NMR (101 MHz, MeOD) δ 171.5, 168.1, 168.0, 167.6, 164.7, 155.6, 150.8, 137.7, 137.1, 136.7, 136.6, 136.6, 132.9, 132.4, 132.1, 131.8, 130.6, 130.5, 130.0, 128.4, 128.3, 127.1, 127.0, 126.6, 126.3, 125.8, 124.9, 69.2, 69.0, 66.2, 61.2, 60.3, 55.4, 53.8, 52.6, 51.0, 44.7, 39.1, 38.9, 37.4, 37.3, 35.5, 32.9, 31.4, 27.4, 13.1, 11.6, 10.3.

N1-(2-(1-(1-((S)-4-(4-chlorophenyl)-2,3,9-trimethyl-6H-thieno[3,2-f][1,2,4]triazolo[4,3-a][1,4]diazepin-6-yl)-17-methylene-2,16-dioxo-6,9,12-trioxa-3,15-diazaoctadecan-18-

yl)piperidin-4-yl)ethyl)-N4-((S)-3-(3,4-dihydroisoquinolin-2(1H)-yl)-2-hydroxypropyl)terephthalamide (MrTAC-9): Synthesized at 0.01 mmol scale (18% yield). ^{1}H NMR (400 MHz, MeOD) δ 7.87 (q, *J* = 8.3 Hz, 4H), 7.51 – 7.39 (m, 4H), 7.25 – 7.14 (m, 3H), 7.10 (d, *J* = 7.5 Hz, 1H), 6.12 (s, 1H), 5.61 (s, 1H), 4.63 (dd, *J* = 9.0, 5.2 Hz, 1H), 4.22 (s, 1H), 4.05 (s, 2H), 3.79 – 3.38 (m, 20H), 3.23 (t, *J* = 5.5 Hz, 2H), 3.18 (t, *J* = 6.1 Hz, 2H), 3.10 – 3.00 (m, 4H), 2.97 – 2.86 (m, 2H), 2.70 (s, 3H), 2.54 (t, *J* = 6.5 Hz, 2H), 2.46 (s, 3H), 2.24 (t, *J* = 11.7 Hz, 2H), 1.87 (d, *J* = 12.8 Hz, 2H), 1.71 (s, 3H), 1.60 (q, *J* = 6.9 Hz, 2H), 1.39 (t, *J* = 13.7 Hz, 3H). ^{13}C NMR (101 MHz, MeOD) δ 171.5, 168.2, 167.9, 167.7, 164.7, 155.6, 150.8, 137.4, 137.2, 136.7, 132.6, 132.1, 131.8, 130.6, 130.6, 130.0, 128.4, 128.3, 127.1, 127.0, 126.8, 126.3, 126.0, 125.1, 70.3, 70.0, 69.9, 69.2, 69.2, 66.0, 60.8, 55.1, 53.8, 52.6, 50.9, 44.6, 39.1, 38.9, 37.4, 37.2, 35.5, 32.7, 31.1, 26.9, 13.0, 11.5, 10.2.

N1-(2-(1-(1-((S)-4-(4-chlorophenyl)-2,3,9-trimethyl-6H-thieno[3,2-f][1,2,4]triazolo[4,3-a][1,4]diazepin-6-yl)-20-methylene-2,19-dioxo-6,9,12,15-tetraoxa-3,18-diazahenicosan-21-yl)piperidin-4-yl)ethyl)-N4-((S)-3-(3,4-dihydroisoquinolin-2(1H)-yl)-2-hydroxypropyl)terephthalamide (MrTAC-10): Synthesized at 0.01 mmol scale (24% yield). ^{1}H NMR (400 MHz, MeOD) δ 7.92 – 7.80 (m, 4H), 7.51 – 7.38 (m, 4H), 7.22 – 7.12 (m, 3H), 7.10 – 7.06 (m, 1H), 6.11 (d, *J* = 1.5 Hz, 1H), 5.58 (s, 1H), 4.63 (dd, *J* = 9.0, 5.2 Hz, 1H), 4.26 – 4.16 (m, 1H), 3.99 (s, 2H), 3.70 – 3.30 (m, 28H), 3.12 (t, *J* = 6.1 Hz, 2H), 3.02 (q, *J* = 7.5 Hz, 4H), 2.90 (qd, *J* = 13.0, 6.3 Hz, 2H), 2.70 (s, 3H), 2.46 (s, 3H), 2.18 (t, *J* = 11.6 Hz, 2H), 1.85 (d, *J* = 12.6 Hz, 2H), 1.71 (s, 3H), 1.60 (q, *J* = 6.9 Hz, 2H), 1.51 – 1.28 (m, 3H). ^{13}C NMR (101 MHz, MeOD) δ 171.5, 168.1, 167.9, 167.7, 164.7, 155.6, 150.8, 137.7, 137.2, 136.7, 136.7, 136.5, 132.8, 132.1, 131.8, 130.6, 130.0, 128.4, 128.3, 127.1, 127.0, 126.7, 126.3, 125.9, 124.9, 70.1, 70.0, 69.9, 69.2,

69.2, 66.2, 61.1, 60.3, 55.3, 53.8, 52.6, 51.0, 44.6, 39.2, 38.9, 37.4, 37.3, 35.5, 32.8, 31.3, 27.2, 23.9, 13.0, 11.5, 10.2.

Quantification and Statistical analysis

All experiments were repeated with three independent, biological replicates unless otherwise specified. All stated values represent the mean ± S.E.M. Statistical analyses were performed using GraphPad Prism 10 software. Two-sided, Unpaired T-Tests were used to compare two groups and either One-Way or Two-Way Analyses of Variance (ANOVA) Tests were used to compare more than two groups or two categories of groups, respectively (degrees of freedom = n − 1). Dose curves were fitted to sigmoidal regressions using GraphPad Prism 10 software. *$P < 0.05$, **$P < 0.01$, ***$P < 0.001$ and ****$P < 0.0001$ were noted as statistically significant and are denoted in each figure. Image quantification was performed for immunoblots as described above using ImageJ.

2.6 Data Availability

Proteomic data are available via ProteomeXchange (PRIDE) with identifier PXD071805. This paper does not report original code. Any additional information required to reanalyze the data reported in this paper is available from the lead contact upon request. Any new materials can be synthesized as described in the Methods. Characterization of novel material can be found online via doi: 10.1016/j.chempr.2026.102998.

2.7 Acknowledgements

We thank members of the Albrecht Lab for their support in this research. This research was supported in part by Ono Pharmaceuticals (L.V.A.), the Alfred P. Sloan Foundation Research Fellowship (L.V.A.), the National Institute of General Medicine (K99GM159057, E.K.; 1R35GM157370, L.V.A.; 5R01GM137606, A.C.), National Institute of Diabetes and Digestive and Kidney Diseases (5R01DK132900, A.C.), the National Cancer Institute (F31CA295037, L.J.S.), the National Institute of Arthritis and Musculoskeletal and Skin Diseases (T32AR083870, M.C.) the National Science Foundation (J.T.L.), the Defense Advanced Research Projects Agency (HR0011-21-2-0010, A.C.), and the Prince Alwaleed Bin Talal Research Fellowship from the Dubai Harvard Foundation for Medical Research (S.H.S). We thank C. Yu and L. Huang at the UCI High-end Mass Spectrometry Facility for their help and service in MS data acquisition and analysis. S.J.C. is grateful to Michael and Alice Jung for endowing the Jung Chair in Medicinal Chemistry and Drug Discovery at UCLA, which partially supported this work.

2.8 Competing Interest Statement

Broad Institute has filed patent applications for the work described herein. University of California, Irvine has filed a patent for the work described herein. A.C. is a scientific founder and is on the scientific advisory board of Photys Therapeutics.

2.9 Author Contributions

L.J.S. and L.V.A. conceived the project. L.V.A., A.C., S.J.C., M.E.G., and D.S.K. supervised the research. L.J.S., E.K., S.S., G.B., C.R.L., C.N.F., M.C. J.T.L., and F.G. carried out experimental

studies. L.J.S. L.V.A. prepared figures. L.J.S., G.B., E.K., L.V.A., wrote the manuscript. All authors discussed the results and revised the manuscript.

2.10 References

Bachmair, A., Finley, D. & Varshavsky, A. In Vivo Half-Life of a Protein Is a Function of Its Amino-Terminal Residue. Science 234, 179–186 (1986).

Rechsteiner, M. & Rogers, S. W. PEST sequences and regulation by proteolysis. Trends in Biochemical Sciences 21, 267–271 (1996).

Varshavsky, A. N-degron and C-degron pathways of protein degradation. Proceedings of the National Academy of Sciences 116, 358–366 (2019).

Tasaki, T., Mulder, L. C. F., Iwamatsu, A., Lee, M. J., Davydov, I. V., Varshavsky, A., Muesing, M. & Kwon, Y. T. A Family of Mammalian E3 Ubiquitin Ligases That Contain the UBR Box Motif and Recognize N-Degrons. Molecular and Cellular Biology 25, 7120–7136 (2005).

Schreiber, S. L. The Rise of Molecular Glues. Cell 184, 3–9. (2021).

Pettersson, M. & Crews, C. M. PROteolysis TArgeting Chimeras (PROTACs) — Past, present and future. Drug Discovery Today: Technologies 31, 15–27 (2019).

Békés, M., Langley, D. R. & Crews, C. M. PROTAC targeted protein degraders: the past is prologue. Nat Rev Drug Discov 21, 181–200 (2022).

Pergu, R., et al. Development and Applications of Chimera Platforms for Tyrosine Phosphorylation. ACS Cent. Sci. 9, 1558–1566 (2023).

Reddi, R. N., et al. Tunable Methacrylamides for Covalent Ligand Directed Release Chemistry. J. Am. Chem. Soc. 143, 4979–4992 (2021).

Xiao, Z., et al. Identification of Actionable Targeted Protein Degradation Effector Sites through Site-Specific Ligand Incorporation-Induced Proximity (SLIP). J. Am. Chem. Soc. 147, 21549–21559 (2025).

Bondeson, D. P., Smith, B. E., Burslem, G. M., Buhimschi, A. D., Hines, J., Jaime-Figueroa, S., Wang, J., Hamman, B. D., Ishchenko, A. & Crews, C. M. Lessons in PROTAC Design from Selective Degradation with a Promiscuous Warhead. Cell Chemical Biology 25, 78-87.e5 (2018).

Schneider, M., et al. The PROTACtable genome. Nat Rev Drug Discov 20, 789–797 (2021).

Zhang, W., et al. Machine Learning Modeling of Protein-intrinsic Features Predicts Tractability of Targeted Protein Degradation. Genomics, Proteomics & Bioinformatics 20, 882–898 (2022).

Li, F., et al. DeepPROTACs is a deep learning-based targeted degradation predictor for PROTACs. Nat Commun 13, 7133 (2022).

Jevtić, P., Haakonsen, D. L. & Rapé, M. An E3 ligase guide to the galaxy of small-molecule-induced protein degradation. Cell Chemical Biology 28, 1000–1013 (2021).

Seabrook, L. J., Livelo, C. R. & Albrecht, L. V. Designing the Proteome with Chemical Tools: Degrons and Beyond. ChemBioChem 26, e2500345. (2025).

Lee, J. M., Hammarén, H. M., Savitski, M. M. & Baek, S. H. Control of protein stability by post-translational modifications. Nat Commun 14, 201 (2023).

Seabrook, L. J., et al. Methylarginine targeting chimeras for lysosomal degradation of intracellular proteins. Nat Chem Biol 20, 1566–1576 (2024).

Franco, C. N., Seabrook, L. J., Nguyen, S. T., Yang, Y., Campos, M., Fan, Q., Cicchetto, A. C., Kong, M., Christofk, H. R. & Albrecht, L. V. Vitamin B6 is governed by the local compartmentalization of metabolic enzymes during growth. Science Advances 9, eadi2232 (2023).

Albrecht, L. V., Ploper, D., Tejeda-Muñoz, N. & De Robertis, E. M. Arginine methylation is required for canonical Wnt signaling and endolysosomal trafficking. Proc Natl Acad Sci U S A 115, E5317–E5325 (2018).

Larsen, S. C., Sylvestersen, K. B., Mund, A., Lyon, D., Mullari, M., Madsen, M. V., Daniel, J. A., Jensen, L. J. & Nielsen, M. L. Proteome-wide analysis of arginine monomethylation reveals widespread occurrence in human cells. Sci Signal 9, rs9 (2016).

Bedford, M. T. & Clarke, S. G. Protein Arginine Methylation in Mammals: Who, What, and Why. Mol Cell 33, 1–13 (2009).

Maron, M. I., et al. Independent transcriptomic and proteomic regulation by type I and II protein arginine methyltransferases. iScience 24, 102971 (2021).

Akter, F., Bonini, S., Ponnaiyan, S., Kögler-Mohrbacher, B., Bleibaum, F., Damme, M., Renard, B. Y. & Winter, D. Multi–Cell Line Analysis of Lysosomal Proteomes Reveals Unique Features and Novel Lysosomal Proteins. Molecular & Cellular Proteomics 22, 100509. (2023).

Massagué, J. & Sheppard, D. TGF-β signaling in health and disease. Cell 186, 4007–4037 (2023).

Albrecht, L. V., Tejeda-Muñoz, N. & De Robertis, E. M. Cell Biology of Canonical Wnt Signaling. Annu Rev Cell Dev Biol 37, 369–389 (2021).

de Duve, C. & Wattiaux, R. Functions of Lysosomes. Annual Review of Physiology 28, 435–492 (1966).

Fishbain, S., Inobe, T., Israeli, E., Chavali, S., Yu, H., Kago, G., Babu, M. M. & Matouschek, A. Sequence composition of disordered regions fine-tunes protein half-life. Nat Struct Mol Biol 22, 214–221 (2015).

van der Lee, R., Lang, B., Kruse, K., Gsponer, J., Sánchez de Groot, N., Huynen, M. A., Matouschek, A., Fuxreiter, M. & Babu, M. M. Intrinsically Disordered Segments Affect Protein Half-Life in the Cell and during Evolution. Cell Reports 8, 1832–1844 (2014).

Zammit, C. M., Nadel, C. M., Lin, Y., Koirala, S., Ahani, E., Potts, P. R. & Nomura, D. K. Covalent Destabilizing Degrader of AR and AR-V7 in Androgen-Independent Prostate Cancer Cells. J. Am. Chem. Soc. 147, 20512–20524 (2025).

Kaushik, S. & Cuervo, A. M. Chaperone-mediated autophagy: a unique way to enter the lysosome world. Trends in Cell Biology 22, 407–417 (2012).

Wang, Y. & Bedford, M. T. Effectors and effects of arginine methylation. Biochemical Society Transactions 51, 725–734 (2023).

Li, J., Cai, Z., Vaites, L. P., Shen, N., Mitchell, D. C., Huttlin, E. L., Paulo, J. A., Harry, B. L. & Gygi, S. P. Proteome-wide mapping of short-lived proteins in human cells. Molecular Cell 81, 4722-4735.e5 (2021).

Fan, A. T., et al. A Kinetic Scout Approach Accelerates Targeted Protein Degrader Development. Angewandte Chemie International Edition 64, e202417272 (2025).

Dotson H. L. & Ngo J. T. SNAP-tag and HaloTag fused proteins for HaSX8-inducible control over synthetic biological functions in engineered mammalian cells. Preprint at BioRxiv, https://doi.org/10.1101/2022.08.12.503781 (2022).

Erhart D., Zimmermann M., Jacques O., Wittwer M. B., Ernst B., Constable E., Zvelebil M., Beaufils F. & Wymann M. P. Chemical Development of Intracellular Protein Heterodimerizers. Chem. and Biol. 20, 549-557 (2013).

Wang, W., Liu, P., Lavrijsen, M., Li, S., Zhang, R., Li, S., van de Geer, W. S., van de Werken, H. J. G., Peppelenbosch, M. P. & Smits, R. Evaluation of AXIN1 and AXIN2 as targets of tankyrase inhibition in hepatocellular carcinoma cell lines. Sci Rep 11, 7470 (2021).

Peng, Y., Liu, J., Inuzuka, H. & Wei, W. Targeted protein posttranslational modifications by chemically induced proximity for cancer therapy. Journal of Biological Chemistry 299, 104572 (2023).

Sun, Y., Dong, D., Xia, Y., Hao, L., Wang, W. & Zhao, C. YTHDF1 promotes breast cancer cell growth, DNA damage repair and chemoresistance. Cell Death Dis 13, 230 (2022).

Vijay, G. V., et al. GSK3β regulates epithelial-mesenchymal transition and cancer stem cell properties in triple-negative breast cancer. Breast Cancer Research 21, 37 (2019).

Tomaszewski, W. H., et al. Neuronal CaMKK2 promotes immunosuppression and checkpoint blockade resistance in glioblastoma. Nat Commun 13, 6483 (2022).

Yin, L., et al. A mitochondrial outer membrane protein TOMM20 maintains protein stability of androgen receptor and regulates AR transcriptional activity in prostate cancer cells. Oncogene 44, 1567–1577 (2025).

Lin W., Gary J. D., Yang M. C., Clarke S. & Herschman H. R. The Mammalian Immediate-early TIS21 Protein and the Leukemia-associated BTG1 Protein Interact with a Protein-arginine N-Methyltransferase. Journal of Biological Chemistry 271, 15034-15044 (1996).

Guardigni, M., et al. PROTAC-Induced Glycogen Synthase Kinase 3β Degradation as a Potential Therapeutic Strategy for Alzheimer's Disease. ACS Chem. Neurosci. 14, 1963–1970 (2023).

Qu, L., et al. Discovery of PT-65 as a highly potent and selective Proteolysis-targeting chimera degrader of GSK3 for treating Alzheimer's disease. European Journal of Medicinal Chemistry 226, 113889 (2021).

Holmqvist, A., et al. Discovery of a CNS active GSK3 degrader using orthogonally reactive linker screening. Nat. Commun 16, 8857 (2025).

Riching, K. M., Mahan, S., Corona, C. R., McDougall, M., Vasta, J .D., Robers, M. B., Urh, M. & Daniels, D. L. Quantitative Live-Cell Kinetic Degradation and Mechanistic Profiling of PROTAC Mode of Action. ACS Chem. Biol. 13, 2758–2770. (2018).

Clevers, H. & Nusse, R. Wnt/β-Catenin Signaling and Disease. Cell 149, 1192–1205 (2012).

Baek, K., et al. Unveiling the hidden interactome of CRBN molecular glues. Nat Commun 16, 6831 (2025).

Schreiber, S. L. Molecular glues and bifunctional compounds: Therapeutic modalities based on induced proximity. Cell Chemical Biology 31, 1050–1063 (2024).

Chirnomas, D., Hornberger, K. R. & Crews, C. M. Protein degraders enter the clinic - a new approach to cancer therapy. Nat Rev Clin Oncol 20, 265–278 (2023).

Wu, Q., Schapira, M., Arrowsmith, C. H. & Barsyte-Lovejoy, D. Protein arginine methylation: from enigmatic functions to therapeutic targeting. Nat Rev Drug Discov 20, 509–530 (2021).

Wu, Q., et al. PRMT inhibition induces a viral mimicry response in triple-negative breast cancer. Nat Chem Biol 18, 821–830 (2022).

Watts, J., et al. Phase I/II study of the clinical activity and safety of GSK3326595 in patients with myeloid neoplasms. Therapeutic Advances in Hematology 15, 20406207241275376 (2024).

Shen, Y., et al. Discovery of First-in-Class Protein Arginine Methyltransferase 5 (PRMT5) Degraders. J. Med. Chem. 63, 9977–9989 (2020).

Guo, Y., et al. Targeting PRMT5 through PROTAC for the treatment of triple-negative breast cancer. Journal of Experimental & Clinical Cancer Research 43, 314 (2024).

Ju Y., Song H., He Y., Lo Y., Fan Z. & Lu, J. Development of a Selective and Potent PRMT4 PROTAC Degrader with Efficacy against Multiple Myeloma in Vitro and in Vivo. ACS J. Med. Chem. 68(13), 13973-13989 (2025).

Sarott, R. C., et al. Relocalizing transcriptional kinases to activate apoptosis. Science 386, eadl5361 (2024).

Kaniskan, H. Ü., et al. Discovery of Potent and Selective Allosteric Inhibitors of Protein Arginine Methyltransferase 3 (PRMT3). J. Med. Chem. 61, 1204–1217 (2018).

Siarheyeva, A., et al. An Allosteric Inhibitor of Protein Arginine Methyltransferase 3. Structure 20, 1425–1435 (2012).

Matsuo, K., Nishikawa, Y., Masuda, M. & Hamachi, I. Live-cell protein sulfonylation based on proximity-driven N-sulfonyl pyridone chemistry. Angew. Chem., Int. Ed. 57 (3), 659– 662 (2018).

Tsou, H. R., Mamuya, N., Johnson, B. D., Reich, M. F., Gruber, B. C., Ye, F., Nilakantan, R., Shen, R., Discafani, C. & DeBlanc R. 6-Substituted-4-(3-bromophenylamino)quinazolines as Putative Irreversible Inhibitors of the Epidermal Growth Factor Receptor (EGFR) and Human Epidermal Growth Factor Receptor (HER-2) Tyrosine Kinases with Enhanced Antitumor Activity. J. Med. Chem. 44 (17), 2719– 2734 (2001).

Ward, R. A., Anderton, M. J., Ashton, S., Bethel, P. A., Box, M., Butterworth, S., Colclough, N., Chorley, C. G., Chuaqui, C. & Cross, D. A. Structure- and reactivity-based development of covalent inhibitors of the activating and gatekeeper mutant forms of the epidermal growth factor receptor (EGFR). J. Med. Chem. 56 (17), 7025– 7048 (2013).

Zhuang, J., Zhao, B., Meng, X., Schiffman, J. D., Perry, S. L., Vachet, R. W. & Thayumanavan, S. A programmable chemical switch based on triggerable Michael acceptors. Chem. Sci. 11 (8), 2103– 2111 (2020).

Reddi, R. N., Rogel, A., Resnick, E., Gabizon, R., Prasad, P. K., Gurwicz, N., Barr, H., Shulman, Z. & London, N. Site-specific labeling of endogenous proteins Using CoLDR chemistry. J. Am. Chem. Soc. 143 (48), 20095– 20108 (2021).

Choudhary, A. Bifunctional chimeric molecules for labeling of kinases with target binding moieties and methods use thereof. US provisional Patent application US63/173, 351. April 19, 2021.

Li, K. & Crews, C. M. PROTACs: past, present and future. Chem Soc Rev 51, 5214–5236 (2022).

Weng, G., Cai, X., Cao, D., Du, H., Shen, C., Deng, Y., He, Q., Yang, B., Li, D. & Hou, T. PROTAC-DB 2.0: an updated database of PROTACs. Nucleic Acids Research 51, D1367–D1372 (2023).

Donovan, K. A., et al. Mapping the Degradable Kinome Provides a Resource for Expedited Degrader Development. Cell 183, 1714-1731.e10 (2020).

Liu, X. & Ciulli, A. Proximity-Based Modalities for Biology and Medicine. ACS Cent. Sci. 9, 1269–1284 (2023).

Vedagopuram, S., et al. Ultrasmall chemogenetic tags with group-transfer ligands. Preprint at bioRxiv, https://doi.org/10.1101/2025.05.10.653252 (2025).

Taelman V. F., Dobrowolski R., Plouhinec J. L., Fuentealba L. C., Vorwald P. P., Gumper I., Sabatini D. D. & De Robertis E. M. Wnt signaling requires sequestration of glycogen synthase kinase 3 inside multivesicular endosomes. Cell 143, 1136-1148 (2010).

Mathieson, T., et al. Systematic analysis of protein turnover in primary cells. Nat Commun 9, 689 (2018).

Feuermann, M., Mi, H., Gaudet, P., Muruganujan, A., Lewis, S. E., Ebert, D., Mushayahama, T. & Thomas, P. D. A compendium of human gene functions derived from evolutionary modelling. Nature 640, 146–154 (2025).

The UniProt Consortium UniProt: the Universal Protein Knowledgebase in 2025. Nucleic Acids Research 53, D609–D617 (2025).

Hu, G., Katuwawala, A., Wang, K., Wu, Z., Ghadermarzi, S., Gao, J. & Kurgan, L. flDPnn: Accurate intrinsic disorder prediction with putative propensities of disorder functions. Nat Commun 12, 4438 (2021).

Xue, B., Dunbrack, R. L., Williams, R. W., Dunker, A. K. & Uversky, V. N. PONDR-FIT: A Meta-Predictor of Intrinsically Disordered Amino Acids. Biochim Biophys Acta 1804, 996–1010 (2010).

Cerami, E., et al. The cBio cancer genomics portal: an open platform for exploring multidimensional cancer genomics data. Cancer Discov 2, 401–404 (2012).

Fulmer, G. R., Miller, A. J. M., Sherden, N. H., Gottlieb, H. E., Nudelman, A., Stoltz, B. M., Bercaw, J. E. & Goldberg, K. I. NMR Chemical Shifts of Trace Impurities: Common Laboratory Solvents, Organics, and Gases in Deuterated Solvents Relevant to the Organometallic Chemist. Organometallics 29 (9), 2176–2179 (2010).

Zou, W., Li, M., Wan, S., Ma, J., Lian, L., Luo, G., Zhou, Y., Li, J. & Zhou, B. Discovery of PRMT3 Degrader for the Treatment of Acute Leukemia. Adv. Sci. 11 (38), 2405963 (2024).

2.11 Figures

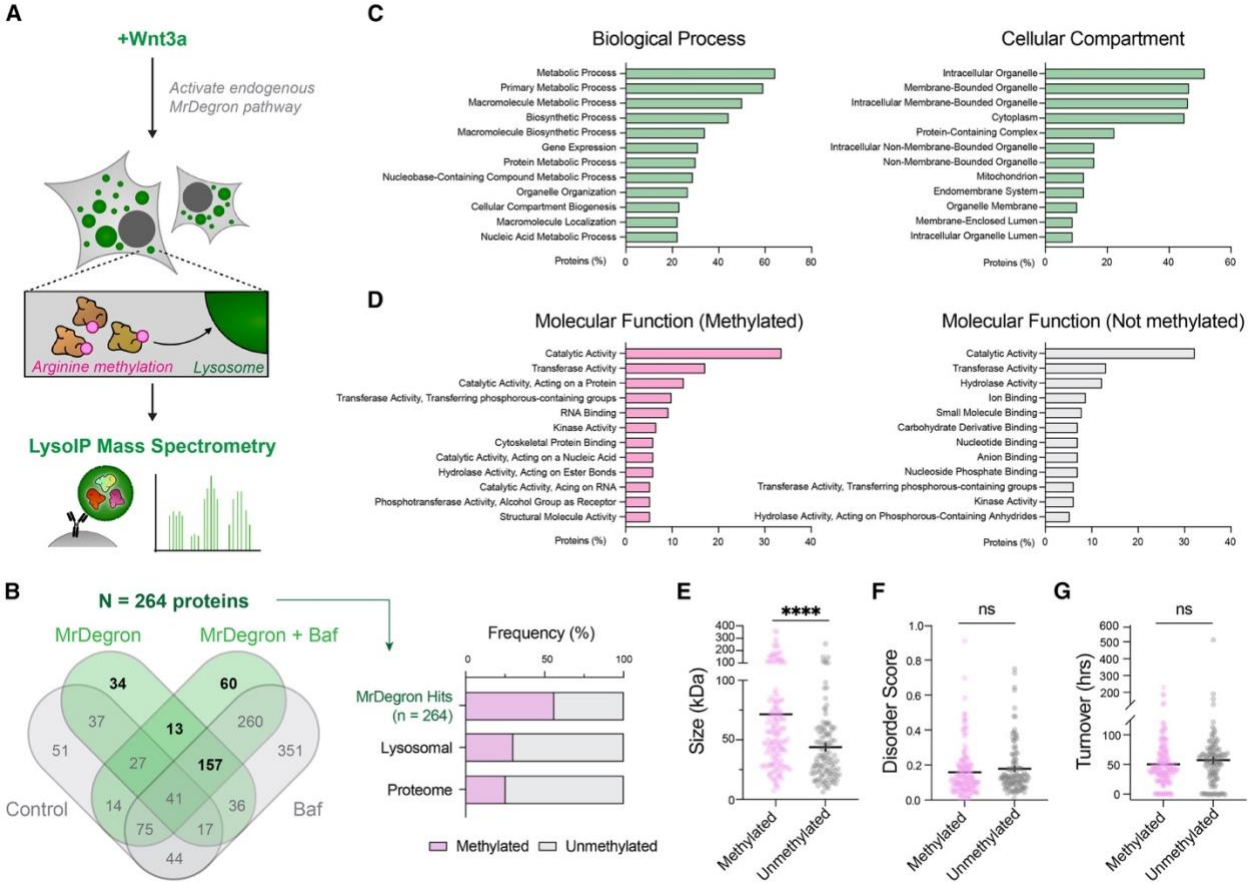

2.1 Defining the lysosomal methyl-degrome of mammalian cells

(A) Schematic depiction of the workflow to identify the methyl-degrome by lysosomal immunoprecipitation mass spectrometry (LysoIP-MS) upon activation of the endogenous methylarginine degron pathway by 20 min treatment with Wnt3a in HEK293T cells stably expressing HA-tagged TMEM192. **(B)** Proteins identified by LysoIP-MS, methylarginine (MrDegron) degron substrates (bold), are exclusively found within Wnt3a-activated samples with or without lysosomal inhibition by bafilomycin (400 nM). Native methylation status of methylarginine degron hits relative to total proteome and lysosomal datasets. Methylation data are from Maron et al. **(C)** Biological process and cellular compartment analysis of methylarginine degron substrates by Pan-GO. **(D)** Molecular function of methylated (left) and the unmethylated (right) proteins identified in LysoIP-MS. **(E)** Average protein size of methylated and unmethylated proteins identified by LysoIP-MS. Data are from UniProt**. (F)** Predicted disorder score (0 is ordered; 1 is disordered) of methylated and unmethylated proteins identified by LysoIP-MS. Data are from DEPICTER2. **(G)** Proportion of long-lived proteins (>8 h half-life) relative to short-lived proteins (<8 h) of methylated and unmethylated proteins identified by LysoIP-MS. Data are from Mathieson et al. Data are presented as means ± SEM (E–G). ****p < 0.0001; ns, not significant; unpaired t test (E–G).

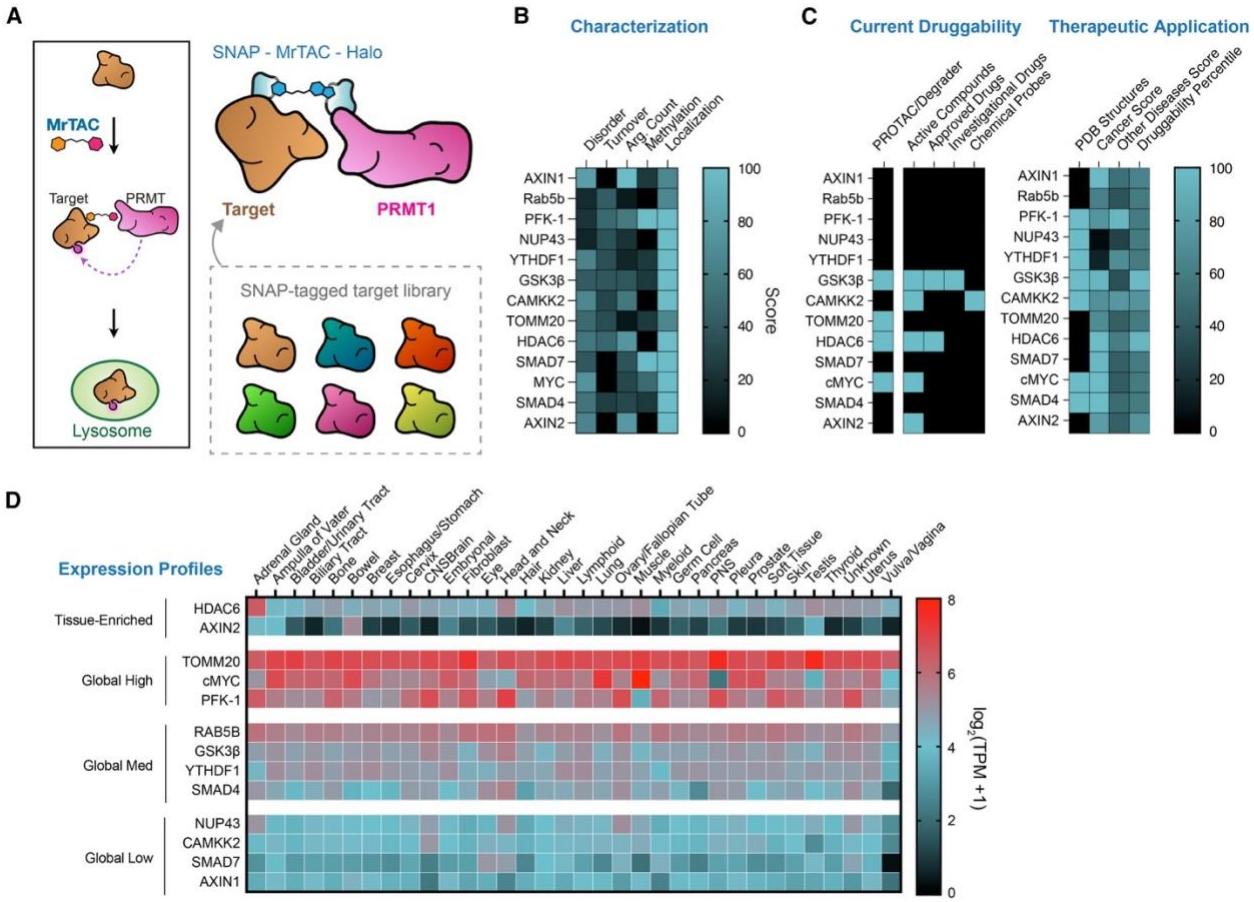

Figure 2.2 Factors and determinants for predicting MrTAC degradability

(A) Schematic of evaluating MrTAC degradation with a modular fusion tagging strategy. MrTAC^{HaXS8} dimerizes HaloTag and SNAP-tag in cells encoding a HaloTagged PRMT1 and a SNAP-tagged protein library. **(B)** Structural characterization of the SNAP-tagged protein library. Disorder prediction is by PondR, and turnover data are from Mathieson et al. Data are not available for AXIN1 in Mathieson et al., and AXIN1 was sourced from Li et al. Surface-exposed arginine counts were calculated via ConSurf modeling, methylation data are from Maron et al., and localization data are from Schneider et al. **(C)** Ligandability characterization of the SNAP-tagged protein library. Data are from canSAR. **(D)** Expression profiles of the SNAP-tagged protein library across cancer lineages. Data are from The Cancer Genome Atlas.

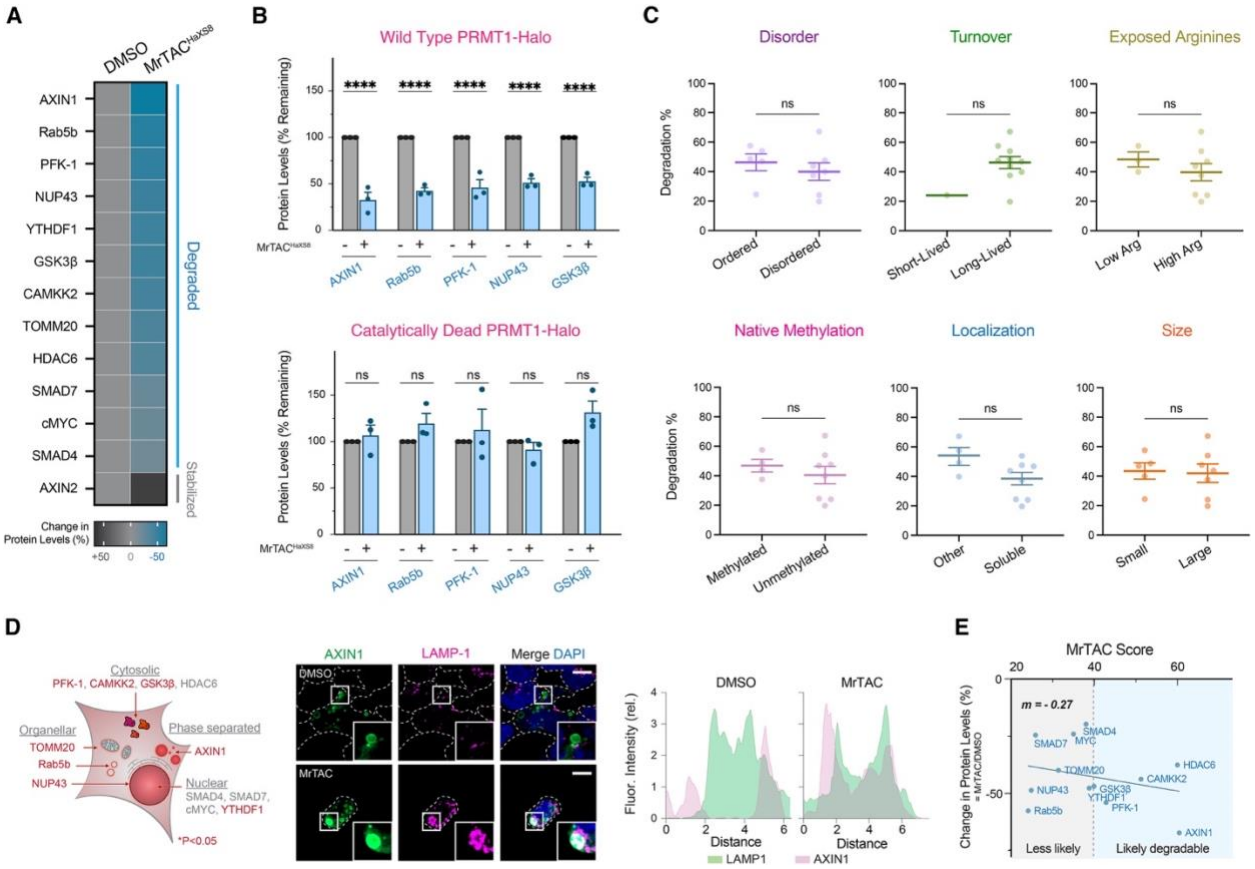

Figure 2.3 Biological variance of protein targets shapes MrTAC degradation

(A) Quantification of SNAP-tagged protein levels after MrTAC^{HaXS8} treatments (24 h at 1 μM) relative to DMSO by immunoblotting (n = 3 biological replicates). **(B)** Quantification of MrTAC degradation for each SNAP-tagged protein target in cells expressing either wild-type (top) or catalytically dead (bottom) PRMT1-Halo by immunoblotting (n = 3 biological replicates). **(C)** Evaluation of protein degradability by MrTAC relative to protein disorder (ordered is >0.6 disorder score), turnover (short lived is <8 h; no turnover data available for SMAD7), surface-exposed arginine count (low Arg is <20), native methylation (binary), localization (other is organelle bound or phase separated), and size (small is <50 kDa). Disorder predictions are from PondR, turnover data are from Mathieson et al., surface-exposed arginines were calculated via ConSurf modeling, methylation data are from Maron et al., and localization and size data are from UniProt. **(D)** Diagram of localization of each SNAP-tagged target; significantly degraded targets are in red. Immunofluorescence shows SNAP-AXIN1-FLAG (green) colocalization with lysosomes marked by LAMP-1 (magenta) with a DAPI co-stain (blue) and representative line traces of signal intensity. Cells were treated for 2 h with 1 μM MrTAC^{HaXS8} in the presence of 500 nM bafilomycin. Scale bar: 10 μm. **(E)** Evaluation of protein degradability by MrTAC based on an aggregated average of predictive traits only (disorder, turnover, arginine count) relative to degradation data. The regression slope (m) is displayed with a dashed line denoting the threshold of degradability at a score of 40. Data are presented as means ± SEM

(A and B). ****$p < 0.001$; ns, not significant; one-way ANOVA with Bonferroni's multiple-comparison test relative to each protein's DMSO control (B and D) or unpaired t test (C).

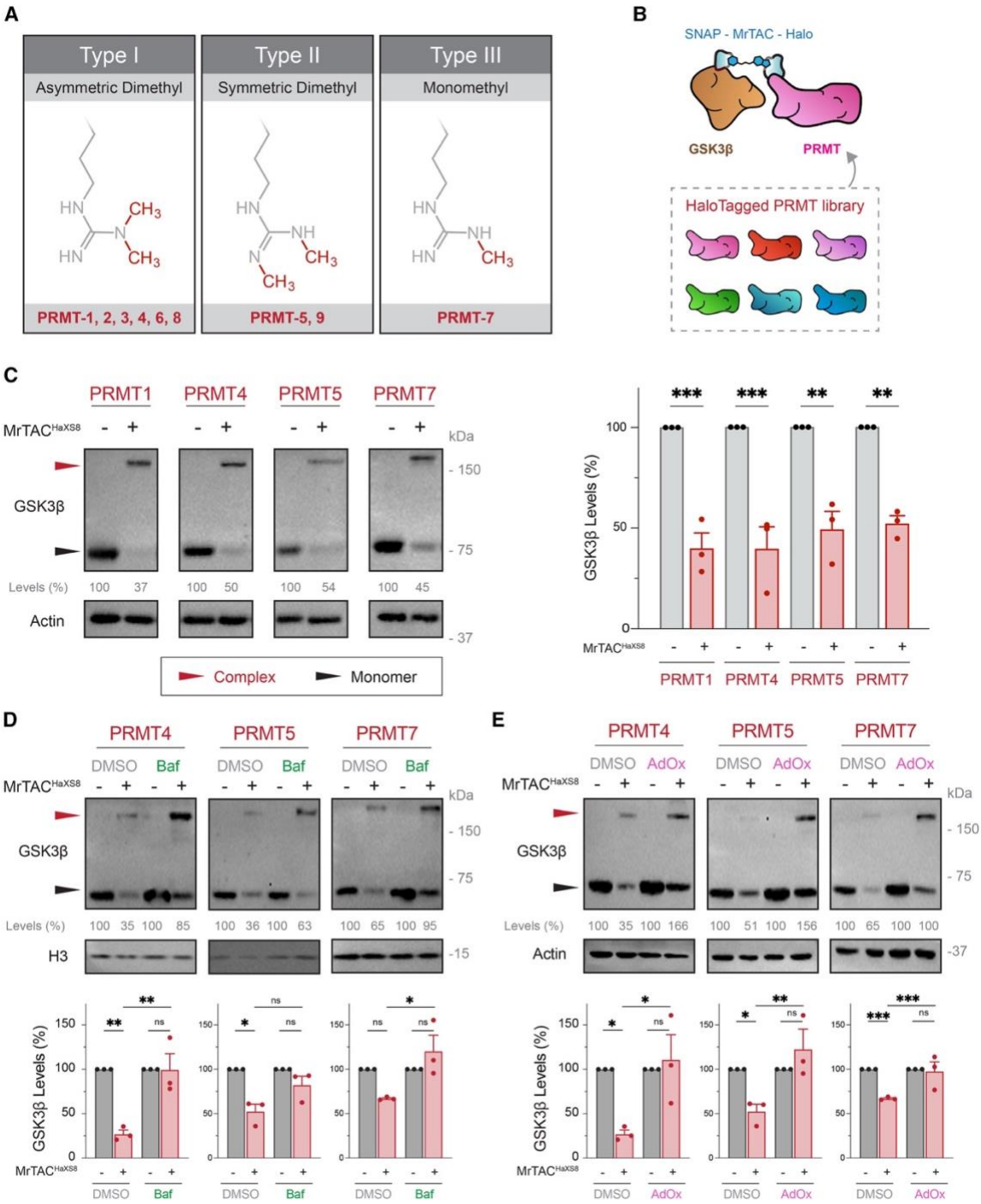

Figure 2.4 MrTAC degradation is sufficient across PRMT classes

(A) Scheme of PRMT classes, the type of arginine methylation that each class catalyzes, and the human PRMTs belonging to each class. **(B)** Schematic depiction of screening MrTAC^{HaXS8} degradation across PRMTs with a modular fusion protein strategy. MrTAC^{HaXS8} dimerizes HaloTag and SNAP-tag in cells encoding a HaloTagged PRMT library and a SNAP-tagged GSK3β. **(C)** MrTAC degradation of SNAP-GSK3β by recruiting different PRMTs for 24 h with 1 μM MrTAC^{HaXS8} (n = 3 biological replicates). **(D)**

MrTAC degradation of SNAP-GSK3β by recruiting different PRMTs for 24 h with 1 μM MrTAC^{HaXS8} in the presence of DMSO or 200 nM bafilomycin (n = 3 biological replicates). **(E)** MrTAC degradation of SNAP-GSK3β by recruiting different PRMTs for 24 h with 1 μM MrTAC^{HaXS8} in the presence of DMSO or 50 μM adenosine dialdehyde (AdOx) (n = 3 biological replicates). Data are presented as means ± SEM. $***p < 0.001$; $**p < 0.01$; $*p < 0.05$; ns, not significant; one-way ANOVA with Dunnett's multiple-comparison test relative to each comparison's DMSO control (C) or two-way ANOVA with Bonferroni's multiple-comparison test (D and E).

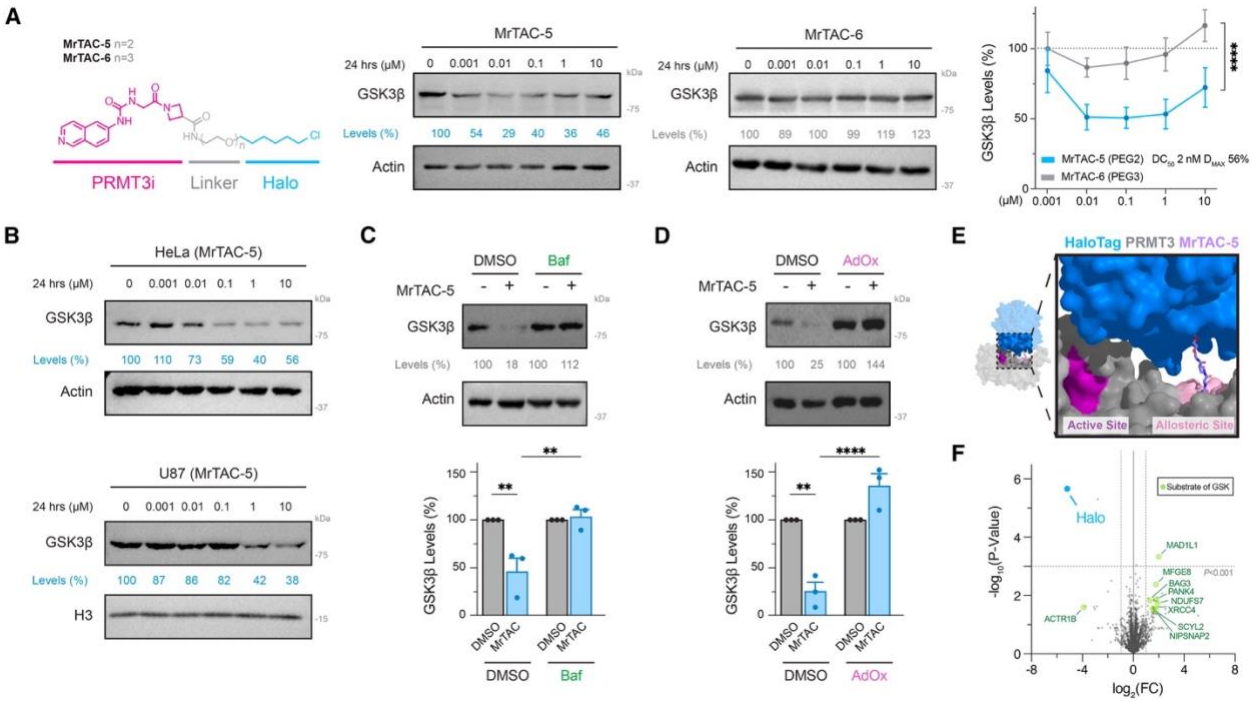

Figure 2.5 PRMT inhibitors recruit endogenous PRMT3 for MrTAC degradation

(A) Structure of classical MrTACs for allosteric PRMT3 recruitment and immunoblot analysis of target (Halo-GSK3β) levels after treatment with MrTAC-5 (n = 4) or MrTAC-6 (n = 3) for 24 h in HEK293 cells. DC_{50} values were obtained by sigmoidal regression analysis, excluding hook effect doses. **(B)** Degradation of Halo-GSK3β in HeLa (n = 3) and U87 (n = 3) cells treated with MrTAC-5 for 24 h. **(C)** Degradation of Halo-GSK3β using MrTAC-5 (24 h, 1 μM) in the presence of DMSO or 100 nM bafilomycin in HeLa cells (n = 3 biological replicates). **(D)** Degradation of Halo-GSK3β using MrTAC-5 (24 h, 1 μM) in the presence of DMSO or 50 μM AdOx in HeLa cells (n = 3 biological replicates). **(E)** Molecular modeling of MrTAC-5 (purple) with PRMT3 (PDB: 4RYL; gray) with HaloTag (PDB: 6U32; blue) based on reference ligand positions. Pink residues show the allosteric site, and purple residues show the methyltransferase active site on PRMT3. **(F)** Global proteomic analysis of HEK293 cells treated with 0.1 μM MrTAC-5 relative to DMSO (n = 4 technical replicates). Halo-GSK3β in blue and GSK3β substrates in green are based on Taelman et al Data are presented as means ± SEM (A, C, and D). ∗∗∗∗p < 0.0001; ∗∗p < 0.01; ∗p < 0.05; ns, not significant; two-way ANOVA (A) with Bonferroni's multiple-comparison test (C and D).

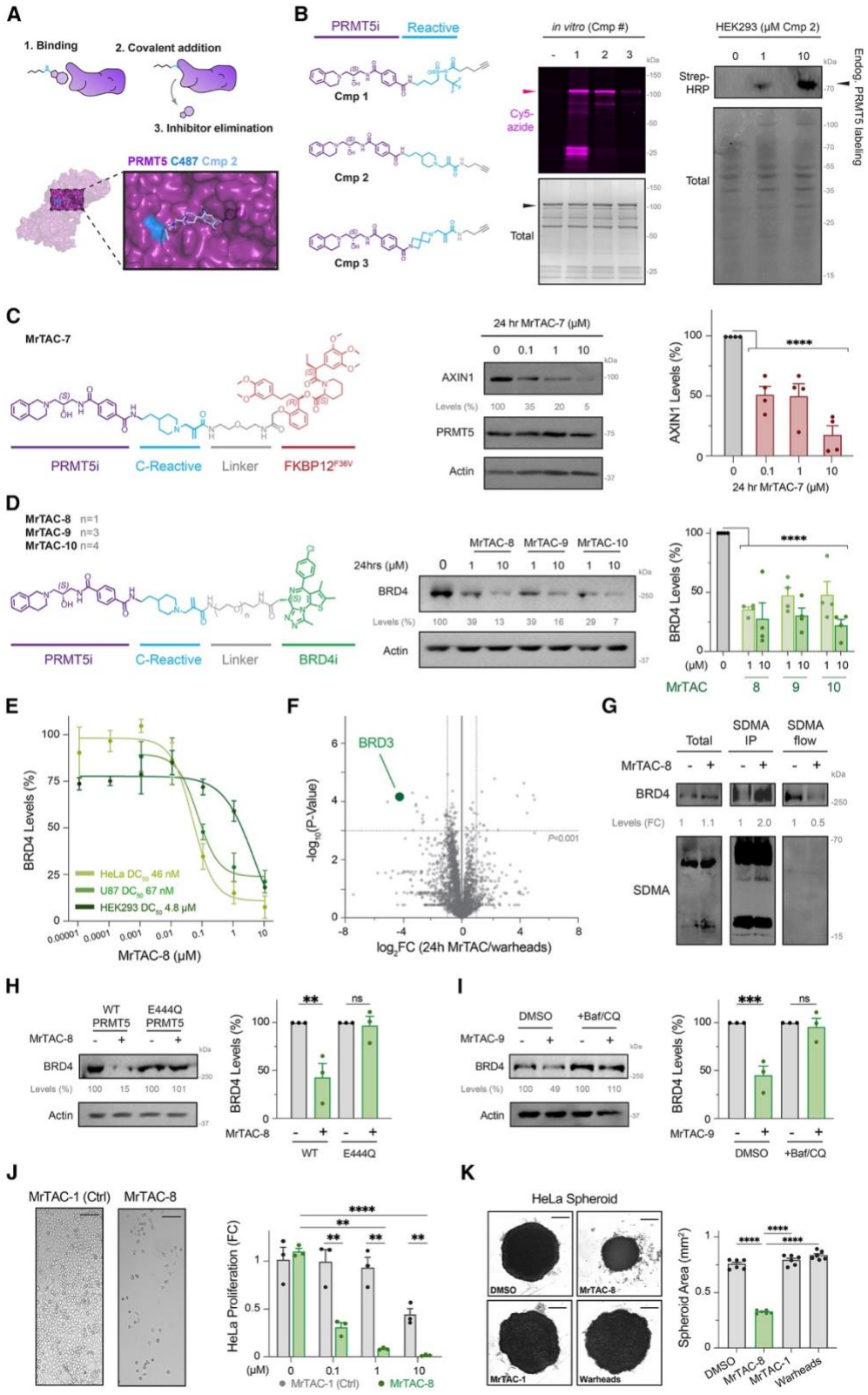

Figure 2.6 Group-transfer chemistry converts PRMT inhibitors into silent recruiters for MrTAC degradation

(A) Schematic of inhibitor-directed group transfer for PRMT5 labeling. Molecular docking is shown for compound 2 with PRMT5 (PDB: 9MGL), and the binding pose affinity is −8.1 kcal/mol. Cysteine 487 is displayed in blue. **(B)** Structures of probes for group-transfer labeling of PRMT5. Labeling efficiency is shown for each probe on purified PRMT5 using a Cy5-azide, and arrowheads mark GST-PRMT5. Click biotin labeling of endogenous PRMT5 used compound 2 in HEK293 cells. Labeling was detected by HRP-conjugated streptavidin. **(C)** Structures of group-transfer MrTACs for recruiting PRMT5 to FKBP12F36V-tagged proteins and immunoblot analysis of AXIN1-FKBP12^{F36V} levels after treatment with MrTAC-7 (PEG1) (n = 4 biological replicates). **(D)** Structures of group-transfer MrTACs for BRD4 and PRMT5 recruitment and immunoblot analysis of BRD4 levels after treatment with MrTAC-8 (PEG1), MrTAC-9 (PEG3), or MrTAC-10 (PEG5) (n = 4 biological replicates). **(E)** Degradation profiles of BRD4 in HEK293, HeLa, and U87 cells treated with MrTAC-8 for 24 h across doses. Dose curves are from sigmoidal regression, and DC_{50} values are shown for each cell line (n = 3 biological replicates). **(F)** Global proteomic analysis of HEK293 cells treated with 1 μM MrTAC-8 relative to cells treated with a combination of either warhead (1 μM Cmp 2 and 1 μM JQ1) (n = 4 technical replicates). BRD3 is highlighted in green. **(G)** Fold change of methylated BRD4 by immunoprecipitation of SDMA-modified proteins in MrTAC-treated cells relative to DMSO-treated cells. Cells were treated for 2 h with 1 μM MrTAC-8 in the presence of degradation inhibitors (500 nM bafilomycin, 10 μM MG132) in HeLa cells. **(H)** Degradation of BRD4 in HEK293 cells expressing wild-type or dominant-negative (E444Q) PRMT5 after 24 h treatment with 1 μM MrTAC-8 (n = 3 biological replicates). **(I)** Degradation of BRD4 in HEK293 cells using MrTAC-9 (10 μM, 6 h) in the presence of cycloheximide (50 μM) and either DMSO or lysosome inhibitors (500 nM bafilomycin and 100 μM chloroquine) (n = 3 biological replicates). **(J)** Proliferation of HeLa cells treated daily for 72 h with either MrTAC-8 or MrTAC-1 (control) (n = 3 biological replicates) with representative bright-field images of the 100 nM doses. Scale bar: 200 μm. **(K)** Growth of HeLa spheroids treated daily for 5 days with 1 μM of either MrTAC-8, MrTAC-1 (control), or Cmp 2 with JQ1 relative to DMSO (n = 6 technical replicates) with representative bright-field images. Scale bar: 500 μm. Data are presented as means ± SEM (C–H), $****p < 0.0001$; $***p < 0.001$; $**p < 0.01$; $*p < 0.05$; one-way ANOVA with Dunnett's multiple comparisons test (C and D) or two-way ANOVA with Bonferroni's multiple comparisons test (H–K).

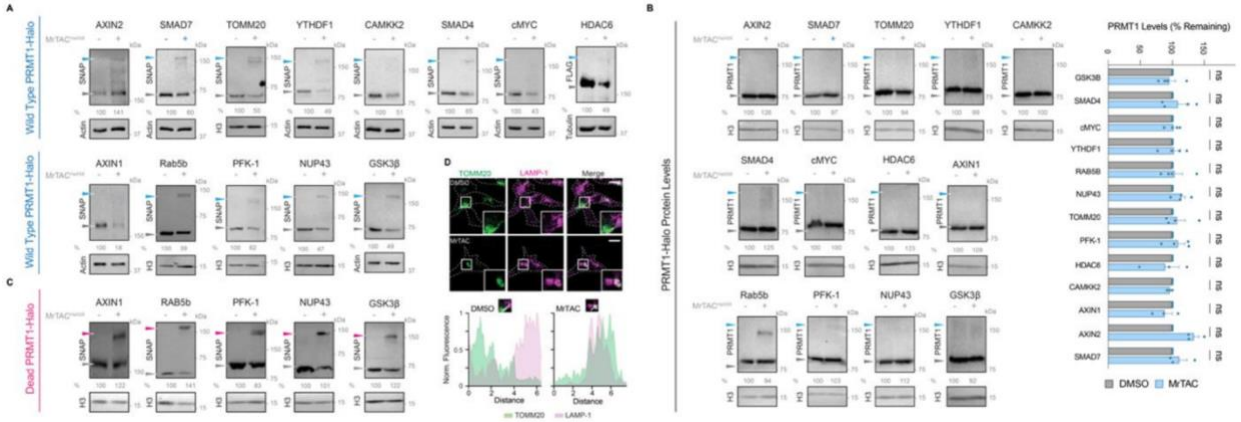

Figure 2.7 MrTAC degradation of the SNAP library

(A) Corresponding blots for Figure 3a denoting SNAP-tagged protein levels following 24 hr DMSO or 1 μM MrTAC^{HaXS8} treatment (n=3 biological replicates). **(B)** Protein levels of PRMT1-Halo in cells treated with DMSO or 1 μM MrTAC^{HaXS8} for 24 hours. **(C)** Corresponding blots for Figure 3b denoting SNAP-tagged protein levels following 24 hr DMSO or 1 μM MrTAC^{HaXS8} treatment in catalytically dead PRMT1-Halo cells (n=3 biological replicates). **(D)** Immunofluorescence of mTurquoise-SNAP-TOMM20 (green) colocalization with lysosomes marked by LAMP-1 (magenta) and representative line traces of signal intensity. Cells were treated for 2 hours with DMSO or 1 μM MrTAC^{HaXS8} in the presence of 500 nM bafilomycin. Scale bar is 10 μm. Data are presented as means ± S.E.M., ns, not significant by One-Way ANOVA with Bonferroni's Multiple Comparisons Test (B).

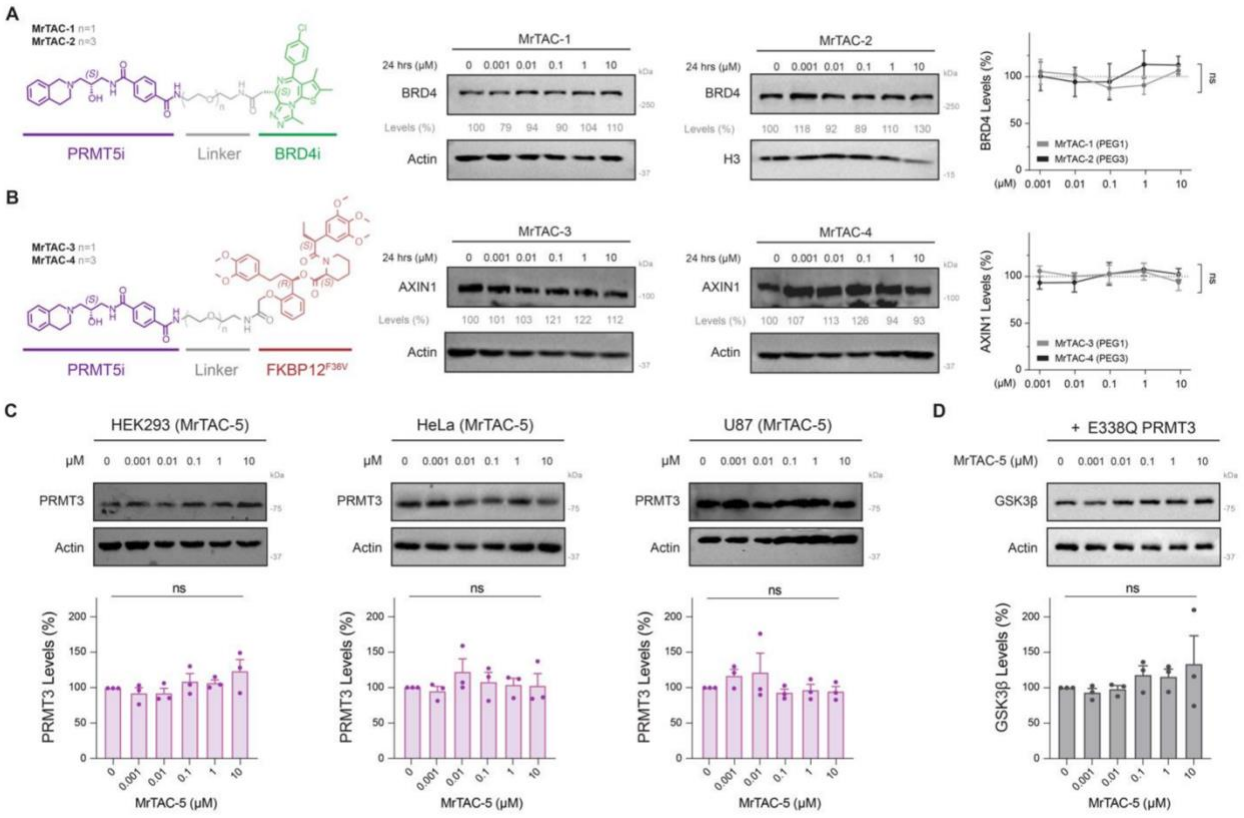

Figure 2.8 Catch-and-release MrTACs for endogenous PRMT recruitment

(A) Structure of classical MrTACs for PRMT5 recruitment and immunoblot analysis of target (BRD4) levels following treatment with MrTAC-1 (PEG1) or MrTAC-2 (PEG3) for 24 hours in HEK293 cells (n=3 biological replicates). **(B)** Structure of classical MrTACs for PRMT5 recruitment and immunoblot analysis of target (AXIN-FKBP12^{F36V}) levels following treatment with MrTAC-3 (PEG1) or MrTAC-4 (PEG3) for 24 hours in HeLa cells (n=3 biological replicates). **(C)** PRMT3 levels in response to MrTAC-5 treatment (24 hours) in HEK293 (left), HeLa (middle), or U87 (right) cells (n=3 biological replicates). **(D)** Levels of Halo-GSK3β across a 24 hr dose curve of MrTAC-5 in HEK293 cells overexpressing a catalytically dead (E338Q) PRMT3. Data are presented as means ± S.E.M., ns, not significant by Two-Way ANOVA (A-B), ns, not significant by One-Way ANOVA (C,D).

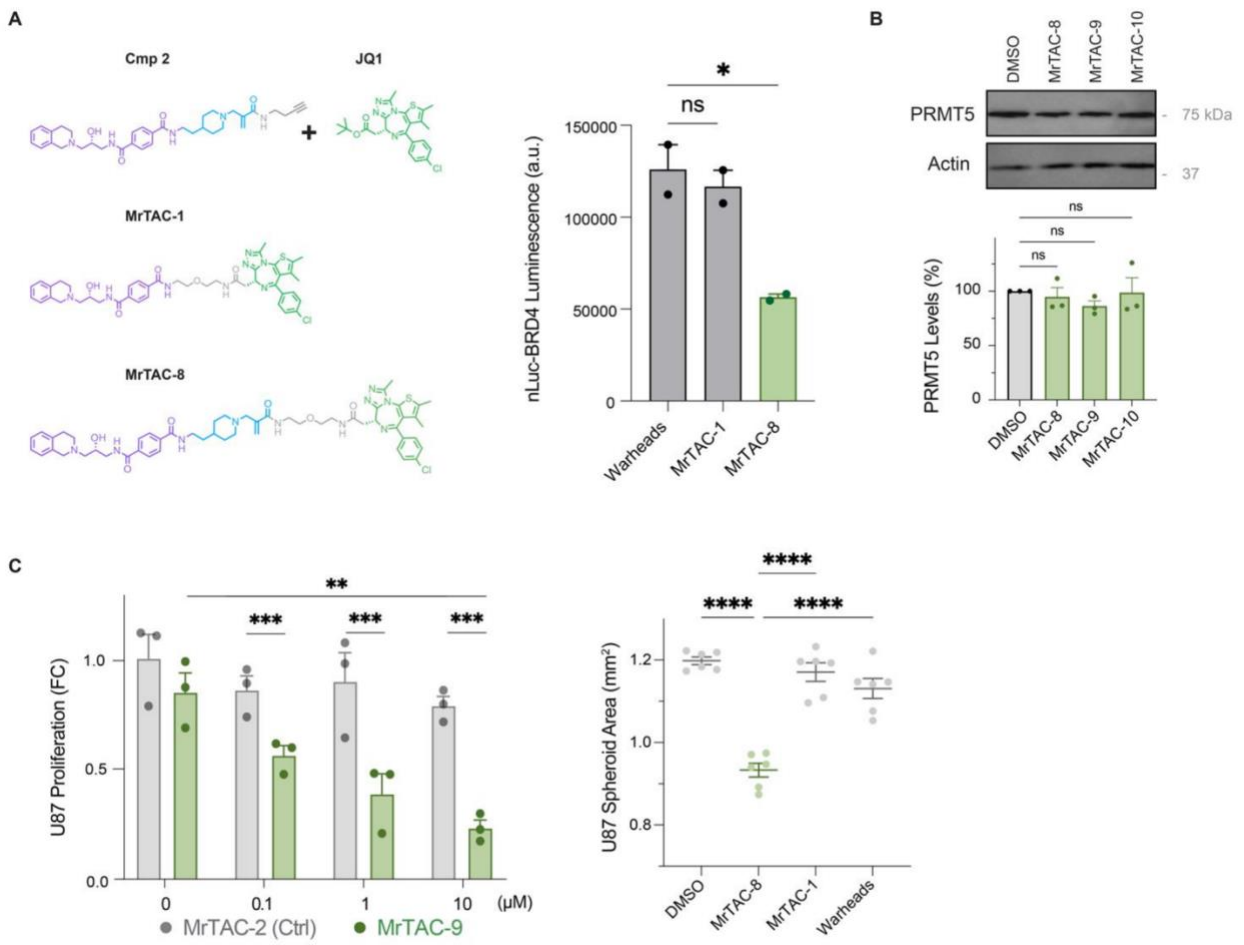

Figure 2.9 Selective degradation of BRD4 by group-transfer MrTACs

(A) Degradation of nLuc-BRD4 using either Cmp 2 + JQ1, MrTAC-1, or MrTAC-8 treated at 10 μM for 24 hours (n=2 technical replicates). **(B)** PRMT5 levels in response to MrTAC-8, -9, or -10 treatment (1 μM, 24 hours) (n=3 biological replicates). **(C)** Proliferation of U87 in 2-D and 3-D spheroid culture following MrTAC treatment. U87s were treated daily for 72 hours in 2-D culture at the indicated doses (n=3) and U87 spheroids were treated daily for 5 days with 1 μM drug after an initial 48 hour seeding period (n=6). Data are presented as means ± S.E.M. (A-C), *P<0.0001 by Two-Way ANOVA with Bonferroni's Multiple Comparisons Test (C).

CHAPTER 3

Summary and Conclusions

3.1 Summary of results

The aim of this work was to evaluate whether arginine methylation could be chemically exploited as a native degradation signal for targeted protein degradation. We first showed that chemical recruitment of PRMT enzymes was sufficient to induce arginine methylation of protein substrates. We then applied this tool to target proteins for degradation through the methylarginine degron pathway, which operated independently of classic degraders. We finally demonstrated MrTAC as a therapeutic tool through the selective degradation of disease-causing proteins that led to suppressed cancer growth. Integrated knowledge from fundamental and chemically induced protein methylation revealed new rules governing protein degradability that resulted in a new class of therapeutics named Methylarginine TArgeting Chimeras (MrTACs).

In Chapter 1 (first published in (Seabrook et al., 2024)), we generate a proof-of-concept platform for proximity-induced methylation. While PRMTs are constitutively active enzymes, whether proximity alone could be used to control substrate methylation had never been tested. Moreover, it remained unknown whether induced methylation could trigger protein degradation given that methylarginine degrons had only been studied in the context of Wnt3a signaling (Albrecht et al., 2018, Franco et al., 2023). We hypothesized that recruiting PRMT1 into proximity with validated methylarginine degron substrates would result in target degradation. To test this hypothesis, we recruited PRMT1 to the model substrate glycogen synthase kinase 3β (GSK3β) using dimerizable fusion proteins. Specifically, the small molecule HaXS8 (denoted MrTAC^{HaXS8}, Erhart et al., 2013)

was used to recruit a HaloTagged PRMT1 to a SNAP-tagged GSK3β. MrTAC^{HaXS8} treatment led to robust and durable degradation of SNAP-GSK3β in a methylation- and lysosome-dependent manner through the microautophagy pathway. Interestingly, MrTAC degradation was not affected by changes in Wnt3a signaling (data not shown), which suggested that the native activity of methylarginine degrons is likely driven by proximity networks instead of external factors that alter PRMT1 behavior. Since PRMT1 methylates a diverse range of peptide motifs within many proteins (Maron et al., 2021, Schapira & Ferreira de Freitas 2014, Boriack-Sjodin & Swinger 2016), we hypothesized that induced proximity could be used to activate novel methylation events on proteins that are not typically degraded by the methylarginine degron (neo-substrates). In line with this, we found that MrTAC could result in degradation of a classic proteasomal substrate, c-Myc, through the Halo/SNAP dimerization system for PRMT1 recruitment. Together, these data demonstrated the versatility of the MrTAC platform for proximity-induced methylation and targeted protein degradation.

We next sought to determine whether MrTAC could be used as a therapeutic tool through proof-of-concept experiments that recruited PRMT1-HaloTag to endogenous, disease-linked protein targets. We designed two series of MrTACs that recruit PRMT1-Halo to oncogenic proteins by derivatizing the HaloTag ligand with either Suberoylanilide Hydroxamic Acid (SAHA) to bind histone deacetylase 6 (HDAC6) or with JQ1 to bind bromodomain containing protein 4 (BRD4) (Haberland, Montgomery & Olsen 2009, Belkina & Denis 2012). MrTAC^{SAHA} and MrTAC^{JQ1} could elicit high levels of target degradation with no effect on the levels of PRMT1-Halo. Degradation required PRMT1 activity and could be rescued by genetic mutation of the PRMT1 active site or through inhibition of methyltransferase activity using the PRMT1 inhibitor

GSK3368715. Loss of either HDAC6 or BRD4, which are both essential genes, suppressed cell survival and proliferation in cell culture models of cancer. We found that the methylarginine degron pathway is a chemically tractable signal for degradation that can be used to reprogram cell biology.

In chapter 2 (first published in (Seabrook et al., 2026)), we dissect the rules governing native and chemically induced methylarginine degrons to generate fully endogenous MrTACs. Prior work in the PROTAC field shows that innate differences in substrate features affects the efficiency of targeted protein degradation based on protein turnover, lysine accessibility, substrate compartmentalization, and disorder (Bondeson et al., 2018, Schneider et al., 2021, Zhang et al., 2022, Li et al., 2022). Although MrTAC could degrade both native PRMT1 substrates and neo-substrates, it was unknown whether innate features of the substrate affected the potency or extent of MrTAC degradation. To better understand the biology behind native methylarginine degrons, we mapped the substrates modified by methylarginine degrons using lysosomal immunoprecipitation-mass spectrometry (LysoIP-MS). We identified 264 proteins that are delivered to lysosomes upon 20 minutes of Wnt3a stimulation. We found that methylarginine degron substrates often report an increase in molecular weight and arginine content, which suggests that the likelihood of a substrate to be recognized by PRMTs may shape its downstream degradation by methylarginine degrons. To assess these trends in a chemically induced setting, we generated a SNAP-tagged protein library bearing different structural and functional features to be tested against MrTAC. We discovered that MrTAC degradability also trended with increased arginine content, verifying that arginine access may improve the chances of a productive methylation event. Interestingly, we also found that MrTAC could also be influenced by other

protein features, including high disorder and long turnover time. These data show that protein clearance by the methylarginine degron is linked to innate substrate variables that can be used to predict substrate compatibility with the MrTAC platform.

In native settings, PRMT1 is responsible for catalyzing over 85% of arginine methylation and is the only PRMT that has been implicated in methylarginine degron addition (Maron et al., 2021). Prior work has established that the PRMT family is structurally diverse and can deposit three types of methylation that, in some cases, can result in opposing effects on the modified substrate (Favia et al., 2019). Given that PRMT1 was sufficient for MrTAC degradation, we hypothesized that only the Type I PRMTs (PRMT1, 2, 3, 4, 6, and 8) could be used for MrTAC degraders since they all deposit asymmetric dimethylarginines. We were surprised to learn that all three classes of PRMTs could be used for MrTAC degraders regardless of the type of arginine methylation that was deposited. Specifically, MrTAC^{HaXS8} recruitment of SNAP-GSK3β to HaloTagged PRMT1, 4, 5 and 7 resulted in a similar extent of target degradation. The mechanism of MrTAC degradation was shared across all four PRMT enzymes and could be rescued by pharmacological inhibition of methylation or lysosomal activity. While these PRMTs are sufficient for methylarginine degron deposition, it remains unclear whether they are necessary for native methylarginine degron activity.

The long-term scope and application of degrader modalities relies on the ability to access endogenous protein machinery. Towards this goal, we sought to recruit endogenous PRMTs to protein targets for MrTAC degradation by derivatizing PRMT-binding ligands with target-binding

moieties. PRMT ligand discovery is a new field that has yet to develop ligands beyond inhibitors, which we hypothesized would block MrTAC degradation because of their inhibitory activity against the PRMT enzyme (Hu et al., 2015). However, recent work showed that in some instances, inhibitors can be used in heterobifunctional molecules to recruit active enzymes through a catch-and-release mechanism. Here, protein association and dissociation from the heterobifunctional can generate regions of high effective molarity, where the effector enzyme can modify the substrate target upon release of the enzyme from its inhibitor (Sarott et al., 2024). We found that derivatizing the allosteric PRMT3 ligand SGC707 (Kaniskan et al., 2018) with a HaloTag could be used for targeted methylation and degradation of a HaloTagged GSK3β through this mechanism. Degradation required methylation and lysosomal activity and was highly selective towards the HaloTagged GSK3β relative to the endogenous proteome, validating the MrTAC mechanism. Interestingly, repurposing PRMT inhibitors for other MrTACs (such as the PRMT5-recruiting GSK3326595) did not always result in effective target degradation, which was presumed to be a result of persistent PRMT inhibition and a failure to catch-and-release. This complements the work by Gray & Crabtree, who found that only a small fraction of inhibitors could be used for enzyme catch-and-release with no clear trend that predicts ligand compatibility (Sarott et al., 2024). These data show that some PRMT inhibitors can be repurposed to generate fully endogenous MrTACs.

Given that only a fraction of existing PRMT ligands could be used for MrTACs, we sought to design a scalable approach to transform PRMT inhibitors into silent recruiters. Prior work in the field of prodrugs shows that modified inhibitors can bind protein targets and subsequently release the inhibitor through a process referred to as covalent ligand directed release (CoLDR) (Reddi et al., 2021, Pergu et al., 2023). We hypothesized that installing a CoLDR reactive group between a

PRMT inhibitor and a small molecule linker could be used to covalently tag PRMTs with MrTACs that result in elimination of the PRMT inhibitor upon labeling. We leveraged prior work showing that cysteine-reactive methacrylamides can be readily applied for CoLDR chemistry by appendage to nitrogen-containing heterocycles that allow for inhibitor elimination. Indeed, we found that introducing a piperidyl-methacrylamide between the PRMT5 inhibitor GSK3326595 and the MrTAC linker allowed for covalent PRMT5 labeling and the elimination of the PRMT5 ligand. To test whether this would preserve PRMT5 activity, we designed group-transfer MrTACs to bind either endogenous BRD4 or FKBP12^{F36V}-tagged fusion proteins. Group-transfer MrTACs sustained high levels of on-target degradation with upwards of 100% protein elimination and demonstrated high selectivity over other proteins. MrTAC degradation of the cancer-associated protein BRD4 across spheroid models of cervical cancer and glioblastoma resulted in strong suppression of cancer growth relative to existing inhibitors, which showed only a minor effect on cancer suppression. In summary, this provides a scalable platform to harness existing PRMT inhibitors into MrTAC degraders, thereby expanding the generalizability of the endogenous MrTAC platform.

The presented work generates an entirely new toolset for studying and understanding the fundamental biology of arginine methylation. We generate the first tool capable of controlling PRMT interactions for proximity-induced methylation. We have applied this tool to generate a series of novel therapeutics capable of eliminating pathogenic proteins and suppressing disease. Overall, these findings demonstrate the transformative potential of applying naturally occurring degrons for the development of small molecule degraders.

3.2 Implications for therapeutics and future perspectives

Targeted protein degradation provides an innovative opportunity to expand druggability towards the entire proteome. While inhibitors rely on an occupancy-based mechanism with a high effective molarity of the drug, degraders operate by an event-based mechanism of induced protein elimination that enables compound recycling to catalyze further degradation reactions. This has been demonstrated using PROTACs, where impressive amounts of target degradation can be accomplished using only a small pool of the effector enzyme. A quantitative assessment of PROTAC labeling showed that <0.5% of cellular E3 ligase is needed for PROTAC degradation, demonstrating the power of an event-based mechanism to elicit incredibly potent phenotypes (Lynch IV et al., 2024). This mechanism contrasts existing lysosomal degraders AUTOTAC and ATTEC, which function by an occupancy-based tethering mechanism to passively recruit proteins into the lysosomal lumen (Zhou, Xiao & Gao 2025, Li et al., 2019, Ji et al., 2022). MrTAC, in contrast, induces a protein modification that targets the protein for degradation and can survive disassembly of the ternary complex, thereby allowing for catalytic PRMT activity that mimics the PROTAC model.

MrTACs provide an orthogonal route for targeted protein degradation beyond the canonical PROTAC pathway of induced ubiquitination by E3 ligase complexes. However, a major limitation in new degrader technologies is the inability to predict which degrader modality is best suited for a new protein target. Looking forward, the efficiency of MrTAC should be compared against PROTACs using disease models with varying methyltransferase/E3 expression profiles, and lysosome/proteasome activity profiles. An improved understanding of the benefits and limitations

of either system will streamline future degrader development and increase the throughput of the degrader pipeline.

A major advantage for targeted degradation therapeutics is their ability for tissue-specific activity through the recruitment of E3 ligases that are exclusively expressed in a target tissue (Li & Crews 2022, Békés, Langley, & Crews et al., 2022). PRMTs are highly abundant enzymes with varying patterns of tissue expression that are subject to change in disease (Boriack-Sjodin & Swinger 2016, Bedford & Clarke 2009). Notably, PRMT1 and PRMT5 are highly upregulated in many cancers (Lee et al., 2025). The PRMT5-recruiting MrTACs showed a nearly 100-fold increase in the potency of BRD4 degradation in cancerous cell lines (HeLa, U87) relative to non-cancerous cell lines (HEK293). Whether this is a direct result of increased PRMT5 expression is unclear and is worthy of investigation in future work. Similarly, the precise threshold for lysosomal activity that is required for MrTAC degradation would provide important insight into the scope of MrTACs as a therapeutic in diseases with decreased lysosomal activity, such as neurodegeneration. Among the PRMT family, PRMT8 shows the highest degree of tissue specificity and is exclusively expressed in cortical neurons (Bedford & Clark 2009). PRMT8-recruiting MrTACs could therefore provide a window to generate tissue-specific MrTAC degraders that are delivered globally but are only active in PRMT8-expressing cells. Similarly, some PRMTs demonstrate subcellular compartmentalization such as the cytosol-restricted PRMT3 and the nuclear-restricted PRMT6 (Bedford & Clarke 2009). Since many pathogenic proteins report defects in localization (Lacoste et al., 2024), subcellular-specific MrTACs may be able to degrade a target protein within one compartment, thereby sparing the healthy counterpart.

Interestingly, the group-transfer MrTACs provide a polypharmacological effect due to the inhibitor-directed addition-elimination. Following binding, the PRMT5 warhead is released and can still act as a functional inhibitor, which drives a reduction in the global levels of symmetric dimethylarginine. Hence, the increase in on-target methylation of BRD4 is countered by a decrease in off-target methylation on the proteome. This suggests that group-transfer MrTACs only require the activity of a small fraction of cellular PRMT5, as observed with PROTACs that used <0.5% of cellular CRBN for targeted degradation (Lynch IV et al., 2024). An ideal MrTAC would have less obstructive effects on peripheral cell biology, which could be accomplished by structure-activity relationship modeling of the PRMT5 ligand to preserve its binding but minimize its inhibitory effects. However, it is also possible that this polypharmacology could provide a therapeutic benefit given that excessive PRMT5 activity is often a cancer vulnerability. Whether a dual acting pro-drug/degrader would provide a more powerful therapeutic strategy over a degrader alone is worthy of consideration as we extend group-transfer MrTACs towards the recruitment of other PRMTs.

Insights into the fundamental biology governing methylarginine degrons have greatly improved our ability to implement and design MrTACs but remains incompletely understood. A fundamental question that remains unanswered is how substrates are trafficked to lysosomes following their methylation. Thermal shift assays show that MrTAC has no noticeable effect on the intrinsic stability of a target protein (data not shown), which suggests that a reader of arginine methylation may be responsible for coordinating substrate delivery to the lysosomal surface. Several proximity-labeling and CRISPR-based screening tools have uncovered the mechanism behind existing proteasomal and lysosomal degraders (Tao et al., 2023, Srestha et al., 2025, Anh et al., 2023) and

could be applied here to understand the cellular connections between PRMT methylation and microautophagy.

In summary, we have developed a chemical strategy to harness arginine methyltransferases for targeted protein degradation. The presented work creates a strong basis for future studies seeking to understand methyltransferase biology, develop precision therapies, and expand the druggable proteome.

3.3 References

Seabrook, L. J., et al. Methylarginine targeting chimeras for lysosomal degradation of intracellular proteins. Nat Chem Biol 20, 1566–1576 (2024).

Albrecht, L. V., Ploper, D., Tejeda-Muñoz, N. & De Robertis, E. M. Arginine methylation is required for canonical Wnt signaling and endolysosomal trafficking. *Proc. Natl Acad. Sci. USA* 115, E5317–E5325 (2018).

Franco, C. N. et al. Vitamin B6 is governed by the local compartmentalization of metabolic enzymes during growth. *Sci. Adv.* 9, eadi2232 (2023).

Maron, M. I. et al. Independent transcriptomic and proteomic regulation by type I and II protein arginine methyltransferases. *iScience* 24, 102971 (2021).

Schapira, M., Ferreira de Freitas, R. Structural biology and chemistry of protein arginine methyltransferases. *Med. Chem. Commun.* 5, 1779-1788 (2014).

Boriack-Sjodin, P. A., Swinger, K. K. Protein methyltransferases: a distinct, diverse and dynamic family of enzymes. *Biochemistry* 55, 1557-1569 (2016).

Erhart, D. et al. Chemical development of intracellular protein heterodimerizers. *Chem & Biol.* 20, 549-557 (2013).

Haberland, M., Montgomery, R. L. & Olson, E. N. The many roles of histone deacetylases in development and physiology: implications for disease and therapy. *Nat. Rev. Genet.* 10, 32–42 (2009).

Belkina, A. C. & Denis, G. V. BET domain co-regulators in obesity, inflammation and cancer. Nat. Rev. Cancer 12, 465–477 (2012).

Seabrook, L. J., et al. Exploration of protein degradability enables fully endogenous MrTAC degraders. Chem 12, 120998 (2026).

Bondeson, D. P. et al. Lessons in PROTAC Design from Selective Degradation with a Promiscuous Warhead. *Cell Chem. Biol.* 25, 78-87.e5. (2018).

Schneider, M.,et al. The PROTACtable genome. *Nat. Rev. Drug Discov.* 20, 789–797 (2021).

Zhang, W. et al. Machine Learning Modeling of Protein-intrinsic Features Predicts Tractability of Targeted Protein Degradation. *Genom., Proteom. & Bioinform.* 20, 882–898 (2022).

Li, F. et al. DeepPROTACs is a deep learning-based targeted degradation predictor for PROTACs. Nat Commun 13, 7133 (2022).

Favia, A. et al. The Protein Arginine Methyltransferases 1 and 5 affect Myc properties in glioblastoma stem cells. *Sci. Rep.* 9, 15925 (2019).

Hu, H. et al. Exploration of cyanine compounds as selective inhibitors of protein arginine methyltransferases: synthesis and biological evaluation. *J. Med. Chem.* 58, 1228-1243 (2015).

Sarott, R.C. et al. Relocalizing transcriptional kinases to activate apoptosis. *Science* 386, eadl5361 (2024).

Kaniskan, H. Ü. et al. Discovery of Potent and Selective Allosteric Inhibitors of Protein Arginine Methyltransferase 3 (PRMT3). J. Med. Chem. 61, 1204–1217 (2018).

Reddi, R. N. et al. Tunable Methacrylamides for Covalent Ligand Directed Release Chemistry. J. Am. Chem. Soc. 143, 4979–4992 (2021).

Pergu, R. et al. Development and Applications of Chimera Platforms for Tyrosine Phosphorylation. ACS Cent. Sci. 9, 1558–1566 (2023).

Lynch IV, T. L. et al. Quantitative Measurement of Rate of Targeted Protein Degradation. *ACS Chem. Biol.* 19, 1604–1615 (2024).

Zhou, X., Xiao, Y. & Gao, Y. Challenges and opportunities for lysosome-targeting chimeras. Cell Rep. Phys. Sci. 6, 102778 (2025).

Li, Z. et al. Allele-selective lowering of mutant HTT protein by HTT–LC3 linker compounds. Nature 575, 203-209 (2019).

Ji, C. H. et al. The AUTOTAC chemical biology platform for targeted protein degradation via the autophagy-lysosome system. Nat. Comm. 13, 904 (2022).

Chang, B., Chen Y., Zhao, Y., Bruick R. K., JMJD6 is a histone arginine demethylase. *Science* 318, 444-447 (2007).

Tao, A. J. et al. A biotin targeting chimera (BioTAC) system to map small molecule interactomes in situ. *Nat. Comm.* 14, 8016 (2023).

Srestha, S. et al. Characterization of PROTAC specificity and endogenous protein interactomes using ProtacID. *Nat. Comm.* 16, 8089 (2025).

Anh, G. et al. Elucidating the cellular determinants of targeted membrane degradation by lysosome-targeting chimeras. Science 382, eadf6249 (2023).

Li, K. & Crews, C. M. PROTACs: past, present and future. Chem. Soc. Rev. 51, 5214–5236 (2022).

Békés, M., Langley, D. R. & Crews, C. M. PROTAC targeted protein degraders: the past is prologue. Nat. Rev. Drug Discov. 21, 181–200 (2022).

Bedford, M. T., Clarke, S. G. Protein Arginine Methylation in Mammals: Who, What, and Why. *Mol. Cell* 33, 1-13 (2009).

Lacoste, J. et al. Pervasive mislocalization of pathogenic coding variants underlying human disorders. *Cell* 187,6725-6741 (2024).